Article

Neuron

The Stabilized Supralinear Network: A Unifying Circuit Motif Underlying Multi-Input Integration in Sensory Cortex

Highlights

- A simple, unified circuit model of contextual modulation and normalization
- Explains transition from facilitation to suppression w/ increasing stimulus strength
- Both excitatory and inhibitory neurons show normalization or suppression
- New experiments in V1 confirm multiple model predictions

Authors

Daniel B. Rubin, Stephen D. Van Hooser, Kenneth D. Miller

Correspondence

ken@neurotheory.columbia.edu

In Brief

Responses to multiple stimuli are typically suppressed relative to summed responses to the individual stimuli, but may facilitate for weak stimuli. Rubin et al. demonstrate a "canonical" circuit mechanism explaining many aspects of multi-input integration and test key model predictions.

Rubin et al., 2015, Neuron *85*, 402–417
January 21, 2015
http://dx.doi.org/10.1016/j.neuron.2014.12.026

CellPress

CellPress

Neuron
Article

The Stabilized Supralinear Network: A Unifying Circuit Motif Underlying Multi-Input Integration in Sensory Cortex

Daniel B. Rubin,[1] Stephen D. Van Hooser,[3] and Kenneth D. Miller[1,2,*]
[1]Center for Theoretical Neuroscience, Doctoral Program in Neurobiology and Behavior, College of Physicians and Surgeons, Columbia University, New York, NY 10032, USA
[2]Department of Neuroscience, Swartz Program in Theoretical Neuroscience, Kavli Institute for Brain Science, College of Physicians and Surgeons, Columbia University, New York, NY 10032, USA
[3]Department of Biology, Swartz Center for Theoretical Biology, Brandeis University, Waltham, MA 02454, USA
*Correspondence: ken@neurotheory.columbia.edu
http://dx.doi.org/10.1016/j.neuron.2014.12.026

SUMMARY

Neurons in sensory cortex integrate multiple influences to parse objects and support perception. Across multiple cortical areas, integration is characterized by two neuronal response properties: (1) surround suppression—modulatory contextual stimuli suppress responses to driving stimuli; and (2) "normalization"—responses to multiple driving stimuli add sublinearly. These depend on input strength: for weak driving stimuli, contextual influences facilitate or more weakly suppress and summation becomes linear or supralinear. Understanding the circuit operations underlying integration is critical to understanding cortical function and disease. We present a simple, general theory. A wealth of integrative properties, including the above, emerge robustly from four cortical circuit properties: (1) supralinear neuronal input/output functions; (2) sufficiently strong recurrent excitation; (3) feedback inhibition; and (4) simple spatial properties of intracortical connections. Integrative properties emerge dynamically as circuit properties, with excitatory and inhibitory neurons showing similar behaviors. In new recordings in visual cortex, we confirm key model predictions.

INTRODUCTION

A key task of sensory cortex is to globally integrate localized sensory inputs and internal signals to parse objects and support perception. While the nature of this computation is not understood, much is known about its manifestation in neuronal firing. Sensory cortical neurons are selective for the structure of a stimulus in their classical receptive field (CRF), a localized region of sensory space. Such selectivity, e.g., orientation selectivity in primary visual cortex (V1), is primarily determined by the ensemble of feedforward inputs the cell receives (Priebe and Ferster, 2008). Modulation of responses by more global influences, including stimuli outside the CRF (Cavanaugh et al., 2002a), additional stimuli within the CRF (Carandini and Heeger, 2012), or spatial attention (Reynolds and Heeger, 2009), primarily alter the gain rather than selectivity of responses, suggesting a key role of cortical circuitry in dynamically modulating response gain.

The modulatory cortical circuit manifests in two properties observed across multiple cortical areas:

(1) Sublinear response summation or "normalization". The response to two stimuli shown simultaneously in the CRF is typically closer to the average than the sum of the responses to the two stimuli shown individually. That is, the responses sum sublinearly. This has been observed in monkeys in areas V1, MT, V4, IT, and MST as well as in cat V1 and many noncortical structures (reviewed in Carandini and Heeger, 2012). However, when stimuli are weak, cortical summation can become linear or supralinear, as observed in MT (Heuer and Britten, 2002) and MST (T. Oshiro et al., Program No. 360.19, 2013, Neuroscience Meeting Planner, Soc. Neurosci., abstract).

(2) Surround suppression. Stimuli outside the CRF (in the "surround") typically suppress responses to CRF stimuli. Surround suppression has been observed in multiple cortical areas, including V1 and V2 in cats (Anderson et al., 2001; Ozeki et al., 2009; Sengpiel et al., 1997; Tanaka and Ohzawa, 2009; Vanni and Casanova, 2013; Wang et al., 2009; Nienborg et al., 2013), mice (Song and Li, 2008; Adesnik et al., 2012; Van den Bergh et al., 2010), and monkeys (Cavanaugh et al., 2002a, 2002b; Sceniak et al., 1999; Schwabe et al., 2010; Shushruth et al., 2009; Van den Bergh et al., 2010), monkey visual areas V4 (Sundberg et al., 2009), MT (Tsui and Pack, 2011), LIP (Falkner et al., 2010) and motor area frontal eye fields (Cavanaugh et al., 2012), and areas serving other sensory modalities (e.g., see Sachdev et al., 2012). However, surround stimuli can facilitate responses to weak center stimuli (e.g., Schwabe et al., 2010; Sengpiel et al., 1997). Furthermore, even while CRF size remains fixed across stimulus strengths (Song and Li,

2008), summation field size—the stimulus size giving maximal response—shrinks monotonically with stimulus strength, as observed in cat (Anderson et al., 2001; Song and Li, 2008), monkey (Cavanaugh et al., 2002a; Sceniak et al., 1999; Shushruth et al., 2009) and mouse (Nienborg et al., 2013) V1 and in monkey V2 (Shushruth et al., 2009) and MT (Tsui and Pack, 2011). Thus, surrounding regions that are facilitating for weak CRF stimuli become increasingly suppressive for stronger CRF stimuli.

These response properties may reflect a canonical computation of cortical circuits (Carandini and Heeger, 2012), often summarized phenomenologically as divisive normalization: each neuron's response is a supralinear "unnormalized response" to driving CRF inputs divided by an increasing function of the unnormalized responses of all neurons in a local network (Carandini and Heeger, 2012). However, normalization cannot easily describe facilitation of response to weak center inputs by surround regions that cannot themselves drive response (though see Cavanaugh et al., 2002a), so here we will use "normalization" only to describe summation of CRF inputs and not surround effects.

Here, we demonstrate a surprisingly simple circuit motif that gives a new and unified circuit-level explanation of this canonical computation. Previous circuit models of these phenomena (e.g., models reviewed in Carandini and Heeger, 2012; Schwabe et al., 2010; Somers et al., 1998) have typically addressed normalization or surround suppression, but not both. They have largely relied on increases in inhibitory input to explain these phenomena. Such increases have not been found in many normalization phenomena (Carandini and Heeger, 2012), and inhibitory input appears decreased in surround suppression (Ozeki et al., 2009) (though see Adesnik et al., 2012; Haider et al., 2010, addressed in Discussion). Consistent with this, inhibitory and excitatory neurons behave similarly in our model, e.g., both show normalization or suppression of responses, which arise as collective network effects. Models of the contrast dependence of surround suppression (Schwabe et al., 2010; Somers et al., 1998) have assumed intrinsic properties of inhibitory cells that rendered them ineffective at low contrasts. While such mechanisms cannot be ruled out (e.g., Kapfer et al., 2007), our unified model instead provides a network explanation of contrast-dependent effects.

We have previously discussed one mechanism underlying our model (Ahmadian et al., 2013). It is based on the fact that a cortical neuron's firing rate is well described by raising its input, as reflected in its depolarization from rest, to a power greater than 1. This power-law input-output (I/O) function arises when the mean input to neurons is subthreshold, so that neurons fire on input fluctuations about the mean (Hansel and van Vreeswijk, 2002; Miller and Troyer, 2002). The cell's I/O function must ultimately saturate, but at least in V1, neurons remain in the unsaturated, power-law region of the I/O function throughout the full range of firing induced by visual stimuli, with powers in the range 2–5 (Priebe and Ferster, 2008).

This power-law presents a puzzle: how does cortex remain stable? The gain of neurons—the change in output rate per change in input, i.e., the I/O function's slope—monotonically increases with response level. Then, if excitatory neurons excite one another, with increasing response level they will more and more strongly amplify their own response fluctuations until, at some "breakpoint" response level, the excitatory subnetwork will become unstable. Activity would then explode until responses saturate, unless the network is stabilized by other factors such as feedback inhibition. A possibility is that excitatory instability is never reached, because the breakpoint level is beyond the dynamic range of cortical networks, or because excitatory instability is prevented by mechanisms such as short-term synaptic depression or hyperpolarizing voltage-activated conductances. However, simple calculations suggest that the breakpoint occurs at relatively low rates (e.g., section 4 of the Supplemental Text of Ozeki et al., 2009), well within cortical dynamic range and for which the effects of these mechanisms should be weak. Direct evidence also suggests excitatory-subnetwork instability in various cortical operating regimes (London et al., 2010; Ozeki et al., 2009).

We showed (Ahmadian et al., 2013) that, in networks of excitatory (E) and inhibitory (I) neurons with power-law I/O functions, stability can be dynamically maintained via feedback inhibition even when response levels move beyond the breakpoint. The network then is an "inhibition-stabilized network" (ISN), i.e., the excitatory subnetwork alone is unstable, but the network is stabilized by feedback inhibition (Ozeki et al., 2009; Tsodyks et al., 1997). Stabilization occurs over a broad parameter regime, i.e., no parameter fine-tuning is required. Furthermore, this stabilization causes a strong change in network operating regime, from supralinear to sublinear response summation, as follows. At low response levels below the breakpoint, i.e., for weak input such as a very low-contrast visual stimulus, neuronal gains are low, so effective synaptic strengths—the change in postsynaptic rate per change in presynaptic rate—are weak. As a result, drive from within the network is weak relative to external drive (mathematically, weak externally driven synapses drive network cells that drive weak network synapses, so network drive is doubly weak relative to external). With only weak interactions between neurons, responses sum supralinearly, following the supralinear I/O function of isolated cells: response to two simultaneously presented stimuli exceeds the sum of the responses to each stimulus presented alone. With increasing input strength, the relative contribution of network drive grows until the breakpoint is reached. Stabilization requires strong damping of the growth of net input (E minus I) such that, in a broad parameter regime, responses then sum sublinearly: the two-stimulus response is less than the sum of the individual stimulus responses. Both E- and I-cell neuronal responses sum sublinearly, an emergent outcome of network dynamics, as opposed to the more intuitive scenario that suppression in E cells results from increased I-cell firing.

Thus, when individual neurons have supralinear input/output functions, inhibitory stabilization drives a transition from weak coupling and supralinear response summation for weak inputs to ISN behavior and sublinear summation for strong inputs. Here, we show how this "stabilized supralinear network" (SSN) mechanism, along with mechanisms involving the spatial structure of connectivity, can give a unified explanation of a wide

range of cortical behavior involving global integration of multiple inputs.

RESULTS

We will focus on modeling V1 behavior, but also refer to other cortical areas. We make several simplifying assumptions. We model interactions in a single layer, e.g., layer 2/3 (L2/3), ignoring interlaminar processing. We assume that the net effect of externally driven input (henceforth, "external input") to this layer is excitatory. We consider only two cell types, E and I, ignoring subtypes. We consider an "E/I pair"—one E unit and one I unit—at each position, where a "unit" can be thought of as a mutually connected set of neurons. We model neuronal firing rates, rather than action potential ("spike") generation, which suffice to understand many aspects of network behavior when spikes are fired irregularly and asynchronously (Ermentrout and Terman, 2010; Murphy and Miller, 2009). These simplifications allow a clear picture to emerge of simple laminar processing motifs that explain a surprising amount of the complexity of cortical responses.

We initially present simple models on a 1D ring or line to highlight mechanisms, but subsequently study a 2D model cortex. The model equations are as follows. Let x represent position of an E/I pair on the model cortex. We let $h(x)$ be the shape and c the magnitude of external input, both taken for simplicity as identical for E and I units. Increasing input strength c represents increasing contrast, but with arbitrary scale; its values should not be equated with contrast. We let $W_{EI}(x_1,x_2)$ be the strength of connection from the I unit at position x_2 to the E unit at x_1, and similarly W_{EE}, W_{IE}, and W_{II} represent $E\rightarrow E$, $E\rightarrow I$, and $I\rightarrow I$ connections, respectively. We let $r_E(x)$ and $r_I(x)$ be the firing rates of, and $I_E(x)$ and $I_I(x)$ the input to, the E and I units at position x. Then the model equations state:

1. The input to a unit is the linear sum of its external input and its input from each cortical unit:

$$I_E(x) = c\,h(x) + \sum_{x'}\left(W_{EE}(x,x')r_E(x') + W_{EI}(x,x')r_I(x')\right). \quad (1)$$

$$I_I(x) = c\,h(x) + \sum_{x'}\left(W_{IE}(x,x')r_E(x') + W_{II}(x,x')r_I(x')\right). \quad (2)$$

The sum over x' ranges over all cortical positions.

2. The steady-state (SS) firing rate of a neuron for a given fixed input is proportional to the input, with negative values set to zero, raised to a power n (e.g., Figure 1B):

$$r_E^{SS}(x) = k\left([I_E(x)]_+\right)^n \quad (3)$$

$$r_I^{SS}(x) = k\left([I_I(x)]_+\right)^n. \quad (4)$$

Here, k is a constant, $n>1$, and $[I]_+$ represents thresholding of I at zero: $[I]_+ = I$ if $I>0$; $=0$, otherwise. k and n are generally taken identical for E and I cells for simplicity, to focus on emergent network properties that arise even without cell-type differences.

3. At any instant of time, each firing rate approaches its current steady-state value with first-order dynamics:

$$\tau_E\frac{dr_E(x)}{dt} = -r_E(x) + r_E^{SS}(x) \quad (5)$$

$$\tau_I\frac{dr_I(x)}{dt} = -r_I(x) + r_I^{SS}(x). \quad (6)$$

Note that steady-state values change in time as firing rates or external inputs change.

Normalization in a 1D Ring Model

We first study an example of normalization: the response to the superposition of two drifting gratings of different orientations. When the gratings are of equal contrast, the response across the V1 population is a sublinear multiple ($\sim$ 0.5 to 0.7) of the sum of the responses to the individual gratings, while as contrasts become unequal, the response approaches "winner-take-all," i.e., the lower-contrast grating has little impact on the response (Busse et al., 2009; MacEvoy et al., 2009). This "cross-orientation suppression" arises at least in part through sublinear summation of subcortical input to cortical cells (e.g., Priebe and Ferster, 2008; but see Sengpiel and Vorobyov, 2005). Nonetheless, given the likelihood that cortex also performs normalization (Carandini and Heeger, 2012), we use this simple experimental paradigm with linearly summing external inputs to study how the model cortex sums multiple inputs.

We consider a set of E/I pairs at a single position in visual space with varying preferred orientations. Preferred orientation, being a circular variable, is represented by the coordinate θ of an E/I pair on a ring (Figure 1A). An oriented stimulus grating induces a Gaussian-shaped pattern of external input strengths peaked at the corresponding preferred orientation. For superposed gratings, the external inputs add linearly. The four connection functions $W_{XY}(\theta_1,\theta_2)$ ($X,Y\in\{E,I\}$) each depend only on the difference $|\theta_1-\theta_2|$ between preferred orientations. The excitation and inhibition received by cells have similar orientation tuning in cats V1 layers 2–4 (e.g., Mariño et al., 2005), so we give these functions identical Gaussian shapes, but different strengths. We have presented a few results from this model previously (Ahmadian et al., 2013), see Figure 1 legend. This simple model directly illustrates the predicted transition from supralinear to sublinear summation and shows that it can account for multiple aspects of normalizing behavior.

With the increasing strength of a single grating stimulus, the network shows the anticipated transition from dominantly externally driven (weakly coupled) to dominantly network-driven (Figures 1C–1E), with network input: (1) increasingly dominated by inhibition (Figures 1C, 1D, and 1F) as observed in mouse S1 under excitatory drive to E cells (Shao et al., 2013) (similar behavior occurs when simulating that protocol, Figure S3), and (2) substantially cancelling external input to leave a slowly growing net input (Figures 1C and 1D). For equal- and high-strength orthogonal gratings, E and I units each add responses sublinearly, with response to two gratings about 0.7 times the sum of the individual responses (Figure 1G). Responses to nonorthogonal gratings also add sublinearly (Figures S4A and S4B), as in experiments (MacEvoy et al., 2009). With increasing

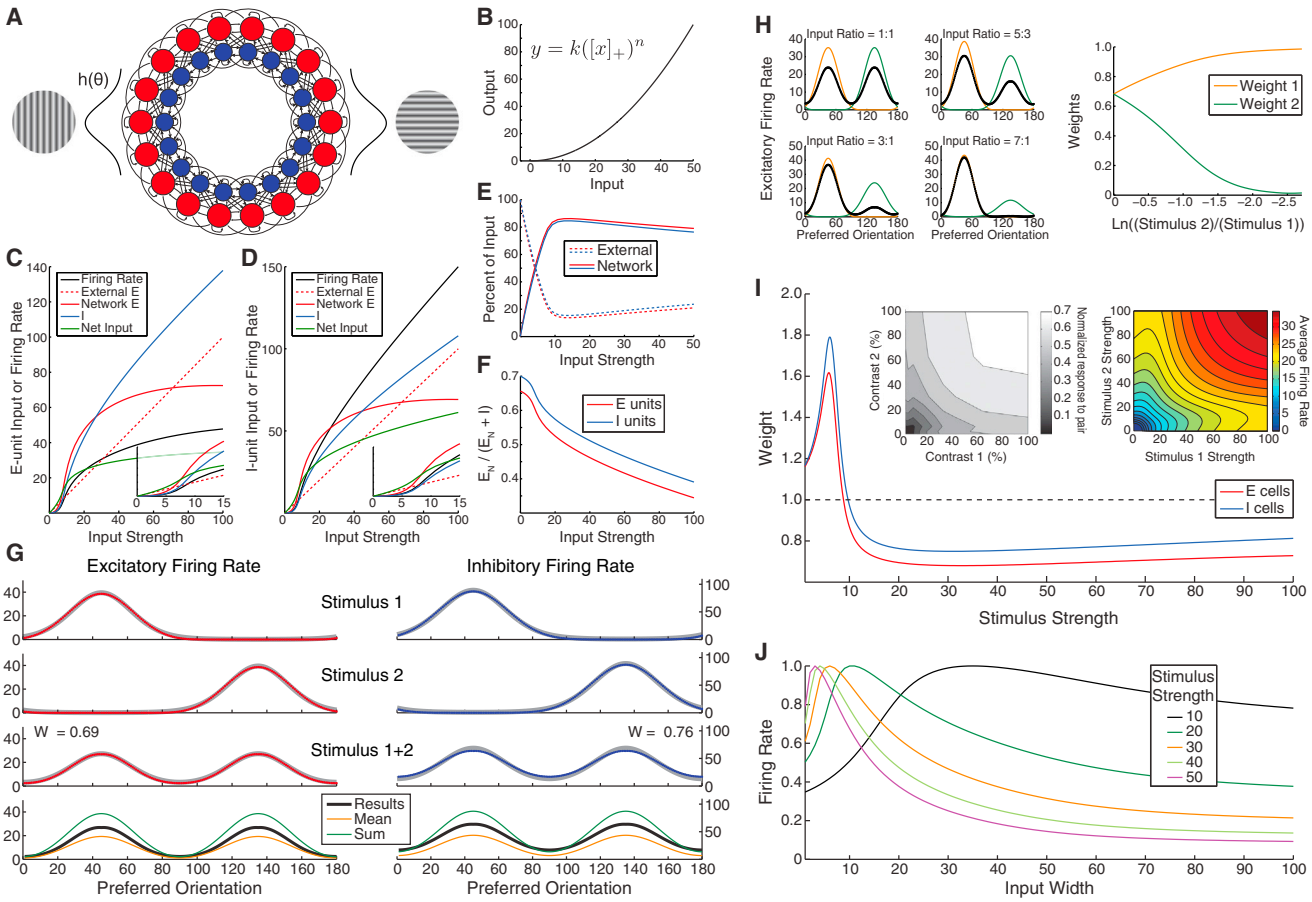

Figure 1. Normalization in a Nonlinear Ring Model

(A) There are 180 E (red) and I (blue) units, with coordinates θ on a ring corresponding to preferred orientations (1° to 180°, 180° = 0°). Lines between units schematize connections between them. A stimulus grating evokes input $ch(\theta)$ equally to E and I units, with $h(\theta)$ a unit-height Gaussian centered at the stimulus orientation with SD $\sigma_{FF} = 30°$, except (J). We consider gratings at 45°, 135°, or both simultaneously.

(B) The power-law input/output function, $k = 0.04$, $n = 2.0$.

(C–F) Use a single-grating stimulus.

(C and D) Input to and firing rates of E (C) and I (D) units at stimulus center. With increasing external input strength c (x axis; dashed lines), network input (E, red and I, blue) transitions from weak to dominating (insets), and substantially cancels external input, so net input (green) grows slowly. Firing rates (black; also shown in Ahmadian et al., 2013) are proportional to net input squared.

(E and F) We consider the summed input received by all E (red) or I (blue) units. With increasing c, input to network (sum of absolute values of E and I input) is increasingly network-driven (E; dashed, external input; solid, network input), and network input is increasingly inhibitory (F; y axis, $E_N/(E_N + I)$, where I and E_N are inhibitory and network excitatory input, respectively).

(G) Sublinear response summation for multiple stimuli. Top two rows, responses of E (left, red) and I (right, blue) units across network to 45° (top) and 135° (2nd row) stimulus, $c = 50$. Third row, responses to both stimuli presented simultaneously. Fourth row, responses from third row (black) versus mean (orange) and linear sum (green) of responses to the two individual stimuli.

(G–I) We fit the response to two superposed stimuli of the E or I population as a weighted sum of the responses to the individual stimuli, with weights w_1 and w_2 determined by least-squared-error fitting. For equal-strength stimuli, $w_1 = w_2 \equiv w$. In (G), best-fit weights w indicated in row 3, with fit shown as gray curve.

(H) Increasingly winner-take-all responses for increasingly divergent contrasts of the two stimuli. Left, E firing rates across network; input strengths (c_1, c_2) are $(40, 40)$, $(50, 30)$, $(60, 20)$, and $(70, 10)$. Orange, response to 45° alone; green, to 135° alone; and black, to both superposed. Right, best-fit weights w_1 (orange) and w_2 (green) for E population versus $\ln(c_2/c_1)$, with $c_1 + c_2 = 80$.

(I) For equal-strength stimuli, best-fit weight w versus stimulus strength $c = c_1 = c_2$ for E (red) and I (blue) responses. Weak inputs add supralinearly. Modified from Ahmadian et al. (2013).

Left inset, averaged responses of neurons in monkey area MT to two superposed CRF stimuli of indicated contrasts (averaged across main diagonal; each cell normalized to its own maximum rate; this is Figure 9 of Heuer and Britten, 2002).

Right inset, model response of E unit at $\theta = 45°$, averaged over stimuli at 45°, 135° or at 135°, 45° having respective strengths c_1 (x axis) and c_2 (y axis).

(J) Width-tuning in orientation space. Response of E unit to stimuli of varying input width σ_{FF} for c from 10 to 50, normalized to maximum rate for given c. Shrinking summation field size versus contrast was shown in Ahmadian et al. (2013).

difference in stimulus strengths, summation becomes increasingly winner-take-all (Figure 1H). Sublinear addition for equal-strength gratings persists across a broad range of stimulus strengths, but at the lowest strengths addition is instead supralinear (Figure 1I). The model results for two-input summation across all pairs of stimulus strengths (Figure 1I, inset right) closely match results in monkey visual cortical area MT (Heuer and Britten, 2002) (Figure 1I, inset left). Model results for both E and I cells across a large set of stimulus-strength pairs are very well fit by phenomenological equations of the normalization model (Busse et al., 2009; Carandini and Heeger, 2012) (E cells, $R^2 = .974$; I cells; $R^2 = .988$; Figure S5). Note that in most previous models only E cells, not I cells, show normalization. These results arise robustly across a reasonable range of parameters, e.g., Figure S6.

A cortical transition from sublinear to supralinear summation for increasingly weak stimuli has thus far not been observed, though a transition to linear summation is seen in MT (Heuer and Britten, 2002) and MST (T. Oshiro et al., Program No. 360.19, 2013, Neuroscience Meeting Planner, Soc. Neurosci., abstract). In MT, average summation was linear when at least one stimulus had contrast below that which drove half-maximal response; behavior at the lowest contrasts was not separately analyzed. The match of model and MT behavior (Figure 1I, inset) suggests, but does not prove, that at the lowest contrasts MT, like the model, sums supralinearly. In V1 cross-orientation suppression, summation remains sublinear down to 6% contrast (Busse et al., 2009). This might be explained by suppression originating in subcortical inputs rather than cortex (Priebe and Ferster, 2008). In all cases, the weakest stimuli studied, or even spontaneous activity, might suffice to drive the network out of the supralinearly summating regime. Note that supralinear effects can be weaker for some parameters, e.g., see Figure 6D.

Normalization in the model is closely related to surround suppression in the space of stimulus features (orientation). When we vary the stimulus orientation width, the width giving the largest response—the orientation "summation field"—shrinks with increasing stimulus strength (Figure 1J), akin to the well-known shrinkage with contrast of the summation field in visual space. (The orientation summation field is distinct from the orientation "CRF" or tuning curve, which, like the visual-space CRF [Song and Li, 2008], experimentally is invariant with contrast [Priebe and Ferster, 2008].) Orientation summation field shrinkage cannot be easily tested in V1, because manipulations of stimulus orientation width either nonlinearly suppress input to cortex (under simultaneous presentation of multiple orientations, Priebe and Ferster, 2008) or alter other stimulus parameters, e.g., spatial frequency or extent across visual space, that independently affect response (under change of grating frequency or aspect ratio). However, it could be tested using optogenetic stimulation to activate broader or narrower sets of orientation columns or, in terms of direction rather than orientation, by testing whether MT directional summation fields shrink with increasing contrast.

In sum, the model for the first time provides a network explanation of normalizing and winner-take-all behavior of both E and I cells. This arises through a transition with increasing stimulus strength from external to internal sources of dominant input, with internally generated input becoming increasingly inhibitory, and a corresponding transition from supralinear to sublinear response summation.

Surround Suppression in a 1D Cortical Model

We now consider interactions between stimuli in different visual positions, i.e., in the CRF and in the surround. We study a 1D line of E/I pairs (Figure 2A), with line position representing CRF position in visual space. We ignore other stimulus features, such as orientation. A drifting luminance grating evokes a static external input, $ch(x)$, that has variable width (representing grating diameter) and peak height c. This input is largely spatially flat, ignoring grating phase, because we are considering the overall input to the set of cells with varying phase preferences at a given spatial position and because many layer 2/3 cells are "complex" cells that are relatively insensitive to grating phase.

Because only E cells make long-range horizontal connections in sensory cortex, we set the spatial range of I projections small relative to E projections, abstracted as making I projections local to each E/I pair. E projection strengths decrease with distance with a Gaussian shape. For reasons discussed below, we take E → I projections to be spatially wider than E → E (more generally, the ratio $E \rightarrow I / E \rightarrow E$ of summed connection strengths should increase with distance; anatomical ranges could be identical).

Spatial considerations now combine with the supralinear to sublinear transition to create a richer set of phenomena. We introduce model behavior in two steps. First, we consider a linear I/O function, which demonstrates spatially periodic behavior that explains a number of experimental results. Then, we return to power-law I/O functions, which yield contrast-dependent modulation of this behavior.

Linear Model

Here, a linear I/O function replaces Equations 3 and 4: $r_E^{SS}(x) = I_E(x)$, $r_I^{SS}(x) = I_I(x)$. A linear model gives a reasonable account of dynamics when firing rates are near their steady-state values for a fixed input. Responses are expressed relative to this steady-state value and so can become negative. We set synaptic weights to make the network an ISN.

Input to cortex of increasing lengths evokes spatially oscillating standing waves of activity (Figure 2B). Intuitively, active neurons suppress their neighbors, which are less active, meaning *their* neighbors are less suppressed (more active). If external input is roughly equal across the activated region, then peaks of the standing waves occur at the edges of the activity pattern, which lacks suppression from one side (Adini et al., 1997). As a result, the activity of the units at the center varies, with increasing stimulus size, from a peak to a trough to a peak of the wave, yielding second peaks in length tuning curves (Figure 2C) as has been observed in firing rates (Sengpiel et al., 1997; Wang et al., 2009, and see new experiments below) and inhibitory conductances (Anderson et al., 2001). The periodic activity occurs at "resonant" spatial frequencies, the frequencies that the network most strongly amplifies (Supplemental Text S2.1; see also Figures 5B and 5C). Sufficiently large and smoothly tapering inputs (e.g., inputs windowed with a Gaussian envelope) lack power at these frequencies, so no periodic activity results (Figures S7 and S8). Given localized inhibitory connectivity, inhibitory resonant frequencies arise only in an ISN (Supplemental Text S2.1.1). In sum, the linear model accounts for surround suppression of

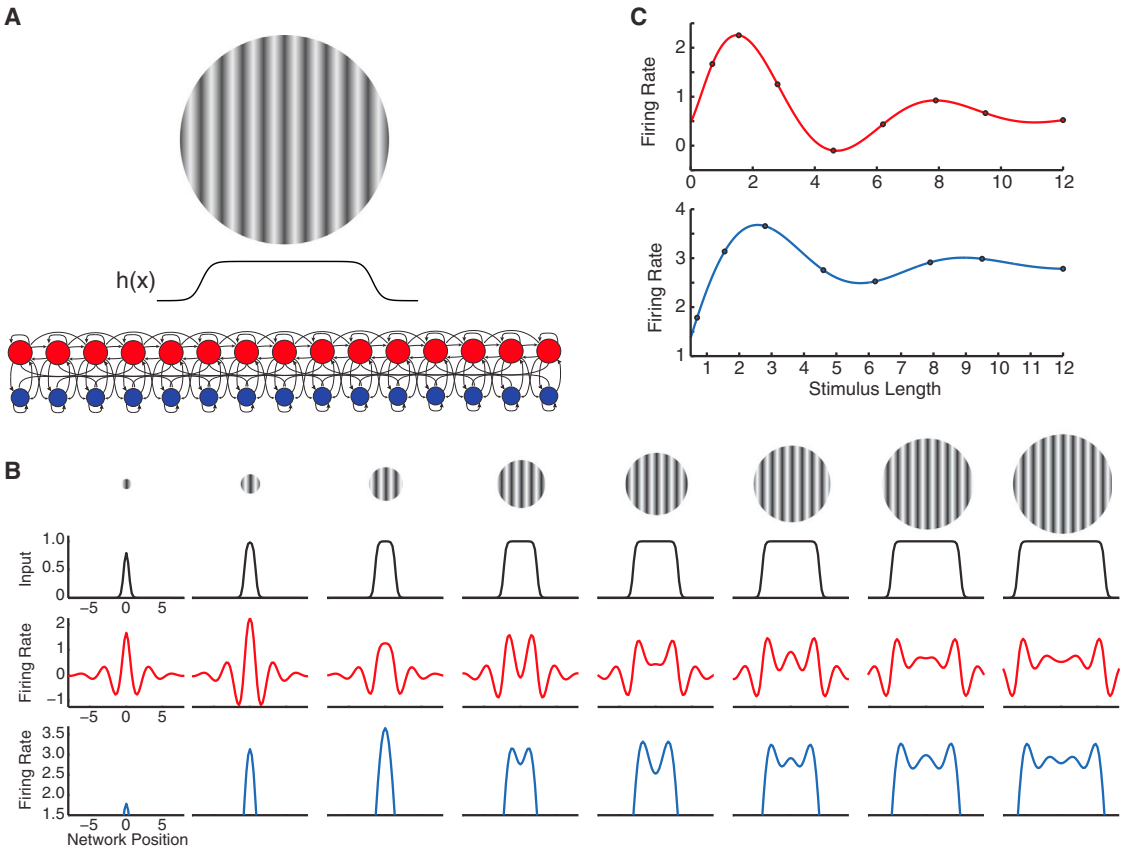

Figure 2. Spatial Contextual Interactions in Linear Model

(A) Cartoon of 1D firing rate model of V1, used for Figures 2 and 3. E (red) and I (blue) units form a 1D grid, with grid position representing CRF visual space position. Grid spacing 0.25° (Figure 2) or 0.33° (Figure 3). Drifting grating stimulus of given size drives input c times input profile $h(x)$ of corresponding width, equally to E and I units.

(B) Input to, and firing rate responses of, model units to stimuli of increasing length versus position of E/I pairs (x axis, degrees; 0, grid center). Top two rows, gratings of increasing size (top) cause 1D input with shape $h(x)$ (plots). Bottom two rows, E (red) and I (blue) firing rates across network, showing spatially periodic activity.

(C) Length-tuning curves of units at stimulus center show surround suppression and second peaks (E, red and I, blue). Circles mark eight stimulus sizes shown in (B). Note here, and in Figure 3, modulations of I units are relatively weak and y axes do not start at zero.

both E and I cells and spatially periodic activity and tuning curves.

Nonlinear Spatial Model

A linear model cannot address qualitative changes in behavior with stimulus contrast, because scaling the input (increasing contrast) only scales responses. We now restore the power law I/O function of Equations 3 and 4. The effects of the linear model are retained, but now are contrast dependent.

As in Figure 1, the network transitions, with increasing input strength, from dominantly externally driven to dominantly network-driven, with network drive increasingly inhibition-dominated (Figures 3A and 3B), corresponding to a transition from non-ISN to ISN behavior (Figure S2D). I-unit as well as E-unit resonant spatial frequencies appear in the ISN regime, with frequencies that increase (wavelengths that decrease) with increasing input strength (Figures S2E and 5D; Supplemental Text S2.3).

Correspondingly, spatially periodic activity and surround suppression are not seen at the lowest contrast (stimulus strength), but emerge with increasing contrast (Figure 3C). As contrast increases, the spatial modulation of activity grows in amplitude and shrinks in wavelength, and second peaks in length tuning appear. These simple effects can explain a wide range of experimental results: (1) the second peaks in the length tuning of I conductance, discussed previously, arise for high-contrast, but not for low-contrast stimuli (Anderson et al., 2001); (2) summation field size (location of first peak in the length tuning curve) shrinks with contrast (Anderson et al., 2001; Song and Li, 2008; Cavanaugh et al., 2002a; Nienborg et al., 2013; Sceniak et al., 1999; Shushruth et al., 2009; Tsui and Pack, 2011) (Figure 3D), following the shrinking resonance wavelength; (3) a high-contrast surround stimulus can facilitate the response to a low-contrast center, but suppress the response to a high-contrast center (Cavanaugh et al., 2002a; Schwabe et al., 2010; Sengpiel et al., 1997) (Figure 3E), but (4) this effect depends on surround size (Figure 3E) and shape (Figure S8B), which may explain varying results in previous studies (Cavanaugh et al., 2002a; Schwabe et al., 2010); and note also that (5) I units develop wider summation fields than E units (Figures 2C and 3D), as observed in rodent V1

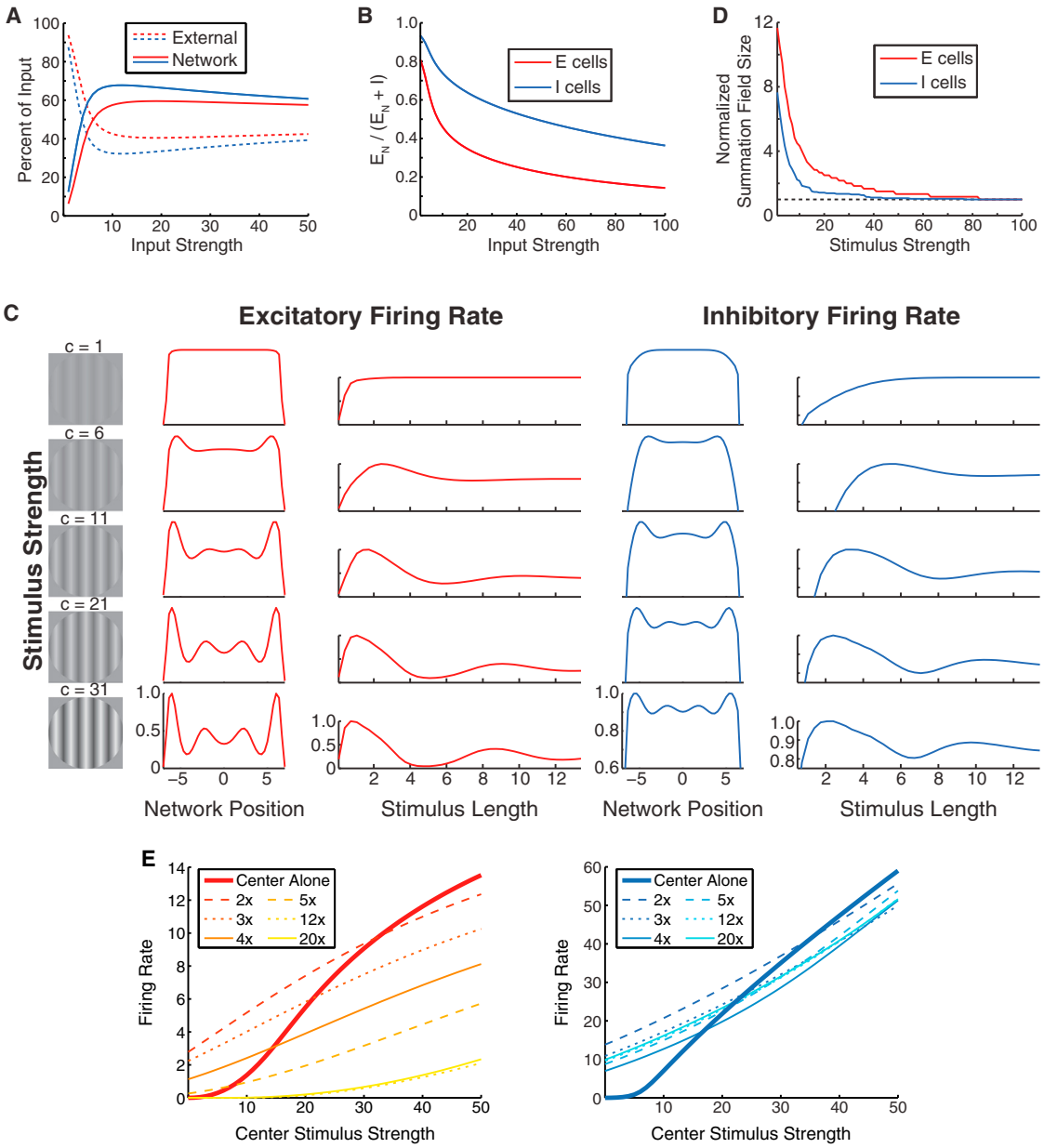

Figure 3. Spatial Contextual Interactions with Supralinear, Power-Law Input/Output Functions

(A and B) Responses to full-field stimuli. Network transitions, with increasing input strength, from dominantly externally driven to network-driven (A), with network drive increasingly inhibition-dominated (B). Conventions are as in Figures 1E and 1F.

(C) Length-tuning at multiple levels of input strength ($c = 1, 6, 11, 21, 31$, schematized by gratings of increasing contrast, left). The two columns of plots for each of E (left) and I (right) show firing rates across network for largest stimulus (left columns) and length-tuning curves for units at stimulus center (right columns). All curves normalized to their maxima.

(D) Summation field size (first peak of length-tuning curve) shrinks with increasing stimulus strength. Values normalized to that at stimulus strength $c = 100$ (dashed line; 0.4°, E units; 1.7°, I units).

(E) Strong surround stimulus ($c = 50$) can switch from facilitative to suppressive with increasing center stimulus strength, depending on stimulus size. Center stimulus fills $c = 50$ summation field, diameter 0.55° (E, left), 1.9° (I, right). Responses to center-only stimulus (thick lines) or with added surround for total stimulus size ranging from 2× to 20× center size (legends).

(Adesnik et al., 2012). Again, these results arise robustly across a reasonable range of parameters, e.g., Figure S6.

Several of these results seem to depend on E → I projections being spatially wider than E → E, although our exploration of parameter space is limited, so we are not certain of this. When these two projections have the same width, we have not seen spatially periodic behavior, and for many parameters, summation field size does not shrink continuously with contrast, but

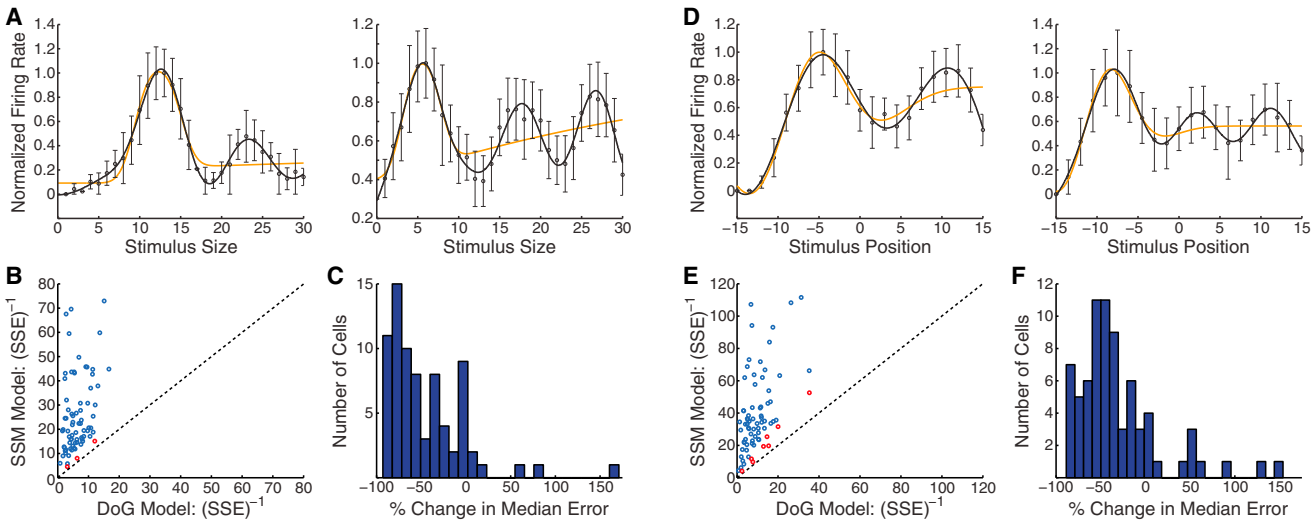

Figure 4. Experimental Tests of Model Predictions

(A–C) Periodicity in size-tuning curves (76 cells studied).

(A) Two examples of tuning curves, normalized to peak = 1. Data indicate mean ± SE as determined from maximum likelihood estimation (Supplemental Methods S1.4.2). Curves, best fit DoG (orange) and SSM (black) models. Tuning curves for all cells, Figure S10.

(B) Reciprocal of summed squared error (SSE) for DoG and SSM models for all neurons studied. Blue points (73 cells), SSM fit significantly better ($p<0.01$) than DoG fit by nested F-test. Red points (three cells), $p>0.01$.

(C) Cross-validation (c-v) analysis. Histogram of number of cells showing given % change in median SSE (in predicting withheld data, across 100 c-v trials) for SSM model relative to DoG model.

(D–F) Periodicity in position-tuning curves (74 cells). Conventions and statistical tests as in (A–C).

(D) Two examples of tuning curves. Tuning curves for all cells, Figure S11.

(E) Reciprocal of SSE for DoG and SSM models. Of 74 cells studied, 66 were significantly better fit by SSM model (blue points).

(F) C-v analysis. Details of statistical tests for all cells, Tables S1, S3, and S4 and Supplemental Methods S1.5.2.

instead jumps from no suppression to the size that saturates external input (note, here I projections are far narrower than E projections; when both have equal width, shrinkage occurs, Figure 1J).

In sum, given connectivity that falls off with spatial distance with I projections short-range compared to E, the transition with increasing stimulus strength to inhibitory stabilization and sublinear summation explains a great deal of contextual modulation behavior of both E and I cells. The model predicts periodicity in activity and tuning curves with wavelengths that shrink and amplitudes that grow with contrast. This explains shrinkage of summation fields and transitions from surround facilitation to surround suppression with increasing contrast.

Experimental Tests I

We tested the predictions of periodic activity in single-unit extracellular studies of neurons in anesthetized ferret V1.

We tested whether size tuning curves show periodicity for high-contrast stimuli (Figures 4A–4C). Few previous studies have carefully studied length tuning for lengths between summation field size and some large size (reviewed in Wang et al., 2009), though curves with periodicity have been reported (e.g., Sengpiel et al., 1997; Wang et al., 2009). We presented drifting gratings ranging in size from 1° to 30° diameter in 1° increments, randomly interleaved. Tuning curves showed clear periodicity (Figure 4A). We fit two models to tuning curves, a difference-of-Gaussians (DoG) model for the center/surround receptive field, which exhibits no spatial periodicity (Figure 4A, orange curves), and a model adding a sinusoidal surround modulation (SSM) to the DoG model (Figure 4A, black curves). To assay whether the curves showed significant periodicity, we considered two tests. In 73 of 76 cells, the SSM fit was significantly better ($p<0.01$) than the DoG fit (Figure 4B) according to a nested F-test, which takes into account the SSM's extra parameters. Using cross-validation (fit each model to a randomly chosen 80% of the data, test model on remaining 20%, repeat 100 times), the SSM's median sum-squared error (SSE) on the withheld data was less than the DoG's for 70/76 cells (Figure 4C; $p = 6.2\times10^{-15}$, 2-sided binomial test of null hypothesis that each model is equally likely to have smaller median SSE for a given cell; median of illustrated distribution significantly different from zero, 2-sided Wilcoxon signed rank test, $p = 1.04\times10^{-10}$).

We next tested spatial periodicity of the activity profile across the cortical surface for high-contrast stimuli, an issue not previously studied to our knowledge (Figures 4D–4F). Ideally, one would show a large drifting grating and sample responses of cells at multiple spatial positions. Instead, we studied the response of each single cell as we moved the drifting grating to multiple randomly interleaved spatial positions. These positional tuning curves showed clear periodicity (Figure 4D), with 66 of 74 better fit by the SSM than the DoG model ($p<0.01$, nested F-test; Figure 4E). In the cross-validation test (Figure 4F), SSM errors were less than DoG errors for 61 of 74 cells ($p = 1.4\times10^{-8}$, binomial test as above; median significantly different from zero,

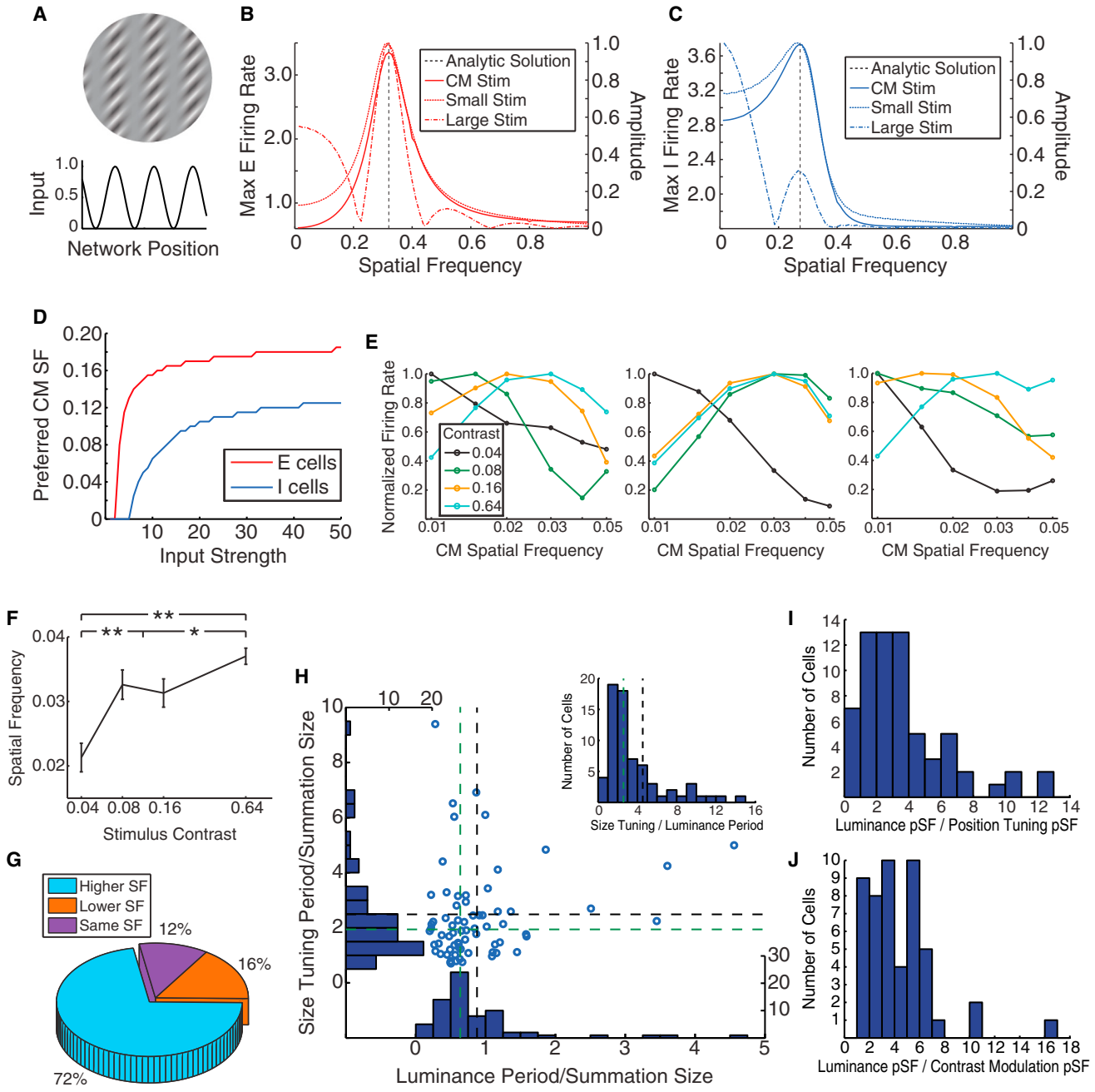

Figure 5. Contrast Modulation (CM) Gratings: Model and Experiments

(A) CM stimuli. Snapshot of 2D CM gratings used in experiments and corresponding spatially periodic 1D model input $h(x)$.

(B and C) Linear model of Figure 2. For E (B) and I (C) units, curves show response versus CM SF (solid lines) and power versus SF (omitting point at SF 0) of firing rates across space for large (dashed-dot lines) and small (dotted lines) luminance stimuli (without CM). All peak at network resonant frequencies, derived analytically (black dashed lines; Supplemental Text S2.1). Y axes, left, responses to CM stimulus; right, normalized power. X axes, SF in cycles/degree. Stimulus diameters, small, 0.5°; large, 4.5° (E) or 5.25° (I).

(D) Nonlinear model of Figure 3. E (red) and I (blue) network resonant frequencies increase with input strength, as measured by preferred CM SF.

(E–G) Experimental measurements of contrast dependence of CM tuning (50 cells studied). Luminance grating had cell's preferred orientation and SF. CM SF tuning was studied at optimal CM orientation, at four luminance contrasts: 4%, 8%, 16%, and 64%.

(E) Normalized CM SF tuning curves for three example cells at the four contrast levels. Tuning curves for all cells, Figure S12.

(F) Mean preferred CM SF increases with stimulus contrast. Error bars, SEM. Data for two middle contrasts were not significantly different (two-sided Wilcoxon rank-sum [WRS] test, $p = 0.68$) and so were grouped together for other tests. All other differences were significant (one-sided WRS test, $n = 50$ [low, high contrasts] or $n = 100$ [medium contrast]): low versus medium, $p < 0.5 \times 10^{-4}$; low versus high, $p < 10^{-7}$; and middle versus high, $p = 0.046$. * $p < 0.05$ and ** $p < 10^{-4}$.

(legend continued on next page)

$p = 2.4 \times 10^{-7}$, Wilcoxon test as above). This result is particularly surprising given an expectation that receptive field strengths monotonically decrease with distance from their center.

Modeling and Experimental Test II: Contrast Dependence of Network Frequency

The model predicts that the network resonant spatial frequencies should increase with contrast (Figure 3). Such a frequency increase would provide strong evidence that the periodic behaviors are emergent properties of the network dynamics, rather than fixed properties of the connections. Because we expected difficulty in accurately measuring oscillations in tuning curves from responses to very low contrast stimuli, we employed a different stimulus used by Tanaka and Ohzawa (2009) to probe center-surround receptive field structure in cat V1: a contrast-modulated sinusoidal grating.

For a given neuron, Tanaka and Ohzawa (2009) presented a large drifting luminance grating covering center and surround, with orientation and spatial frequency (SF) optimal for the CRF, and superimposed a drifting sinusoidal contrast modulation (CM) (Figure 5A, top). They studied the selectivity of the neuron's response to the CM orientation and SF. The neurons were quite selective. The preferred CM spatial period was generally larger than the period of the CRF's preferred luminance SF (mean ± SD, 2.1 ± 0.9 times larger), and there was a wide distribution of relative angles between the preferred CM orientation and the CRF's preferred luminance orientation.

We model the CM as spatial periodicity in the input to cortex, i.e., high- or low-contrast regions receive strong or weak input, respectively (Figure 5A, bottom). The linear model shows CM tuning with preferred spatial period equal to the period of the resonant network activity, i.e., the optimal CM stimulus drives the peaks, but not troughs of resonant activity (Figures 5B, 5C, S2A, and S2B; Supplemental Text S2.1). This remains true in the nonlinear model, in which the preferred CM SF, like the other measures of network frequency, increases with stimulus contrast (Figures 5D and S2E; Supplemental Text S2.3). Thus, the preferred CM SF provides an excellent and direct assay of the network's resonant frequency.

We tested the prediction that network resonant frequencies increase with contrast, by studying the contrast dependence of preferred CM SFs, previously measured only at high contrasts (Tanaka and Ohzawa, 2009). We studied 50 cells at four luminance contrasts. Tuning curves for three example cells (Figure 5E) showed low-pass behavior at low contrast, but preference for higher frequencies at higher contrasts. Like these cells, 50% of studied cells preferred the lowest frequency tested at the lowest contrast tested, while none preferred the lowest frequency at the highest contrast tested. The mean preferred CM SF across cells increased significantly with increasing contrast (Figure 5F). The CM SF preferred at the lowest contrast tested was lower than at the highest contrast for 72% of cells, the same for 12%, and higher for 16% (Figure 5G; $p = 2.5 \times 10^{-5}$ [ties discarded] or $p = 9.0 \times 10^{-5}$ [ties divided equally], two-sided binomial test assuming "lower" or "higher" equally likely for each cell). We were also able to study length tuning across multiple contrasts in a small number of cells ($N = 16$), with results consistent with model predictions (Figures S9A–S9C).

All three experimental measures of network periodicity—length tuning period, position tuning period, and preferred CM SF—have periods, for high contrasts, dominantly in the range 1–8 times larger than the period of the CRF's preferred luminance SF (Figures 5H–5J, and Tanaka and Ohzawa, 2009). This is predicted by the model under a simple heuristic argument: a neuron's summation field should fill no more than 1/2 cycle of the resonant spatial period, as a larger size would drive suppressive troughs; while empirically, the high-contrast summation field typically contains 0.5–4 CRF preferred luminance spatial periods (Teichert et al., 2007). This argument is supported by our data, as illustrated for size-tuning period (Figure 5H): mean and median summation field sizes are $\approx 1/2$ of the size-tuning period; and summation fields contain 0.5–4 luminance spatial periods. The three different periods are not correlated across cells, neither in experiments nor in a model with stochastic connectivity presented below in Figure 6 (Figures S9D and S9E). This presumably reflects different local subnetworks of cells being recruited by each experimental paradigm.

Full Model

Thus far we have studied feature (orientation) effects and spatial effects in separate 1D models. Here, we show that these results can all arise in a single model of a large 2D patch of V1 and also consider effects of more realistic stochasticity. Visual position changes smoothly across the 2D patch and units have preferred orientations given by a superposed orientation map (Figure 6A). Connections and each unit's parameters are chosen stochastically (which indicates that results are robust to parameter variations), with probability of a connection between two units of given types 0.1 (E projections) or 0.5 (I projections) times the product of unit-height Gaussian functions of positional distance (qualitatively as in Figures 2 and 3) and of preferred orientation difference (as in Figure 1). Dependence of connectivity on preferred orientations is supported by evidence discussed for Figure 1 and the fact that long-range horizontal excitatory connections preferentially connect neurons of similar preferred orientation (Gilbert and Wiesel, 1989). We have not tried to tune the model other than to find a regime with reasonable surround suppression (and in retrospect the chosen regime may be suboptimal, Supplemental Methods S1.3.2). Our intent is simply to address qualitative results.

(G) Pie chart summarizing population data, described in main text.

(H–J) For all three measures of network frequency—size tuning preferred SF (pSF) (H, inset), position tuning pSF (I), and high-contrast CM pSF (J)—the network frequency tends to be 1–8 times larger than the cell's luminance pSF, as the model predicts. Histograms include all cells for which SSM model gave better fit by nested F-test than DoG model for length and position tuning (excluding five cells with luminance period larger than the full screen for length tuning) and all 50 cells for CM tuning.

(H) Scatterplot of size tuning pSF (y axis) versus luminance pSF (x axis), each in units of summation field size. Histograms, distributions of data along each axis. Green and black dashed lines, medians and means, respectively, of these distributions. Inset histogram, distribution along diagonals parallel to the main diagonal.

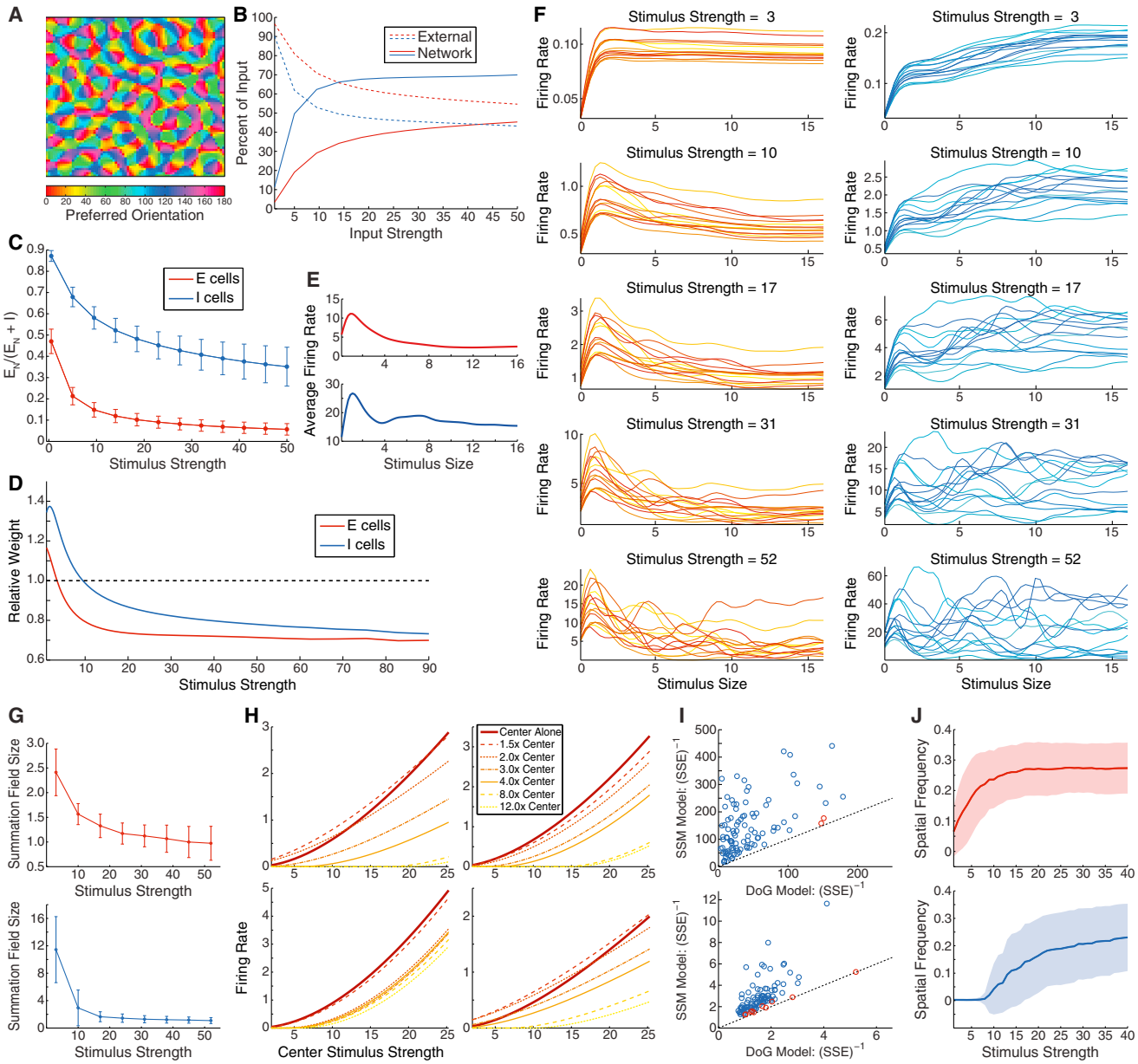

Figure 6. A Large-Scale, Probabilistically Connected, 2D Model of V1

(A) We model a grid of 75×75 E/I units. Retinotopic position progresses uniformly across the grid, spanning 16°×16°. Preferred orientations are assigned according to a superposed orientation map, illustrated.

(B) Strength of external versus network input and (C) $E_N/(E_N+I)$ in response to preferred-orientation full-field gratings both behave similarly to 1D model (all conventions and definitions as in Figure 3A for (B) and Figure 3B for (C). (B) and (C) show means, ± SD in (C), over E or I units at 25 randomly selected locations.

(D) Transition from supralinear to sublinear summation in response to superposed full-field gratings with equal stimulus strength (x axis) and 90° difference in orientations. Plot shows best-fit summation weight (w), averaged over 25 different pairs of orthogonal orientations (first grating equally spaced from 0° to 86.4°), versus stimulus strengths for E (red) and I (blue) units. w computed from curves of average firing rates across units in each of 18 equal-sized bins of preferred orientation. Conventions and definition of w as in Figure 1I.

(E) Mean length-tuning curves for $c = 40$ from all units that demonstrated significant surround suppression among 500 randomly sampled E/I units (surround suppression index, [SSI], >0.25; 498 E and 304 I units). SSI = $(r_{max} - r_{full})/r_{max}$, where r_{max} = maximum firing rate to stimuli shorter than $(2/3)\times16°$; r_{full} = response to largest (16°) stimulus.

(F) Length-tuning for different levels of stimulus strength for 14 E and 14 I units, randomly selected. Each neuron is assigned a different color, yellow to red (E units) or cyan to blue (I units).

(G) Summation field size shrinks with stimulus strength; E (top) and I (bottom) units, mean ± SD over 100 randomly selected grid locations.

(legend continued on next page)

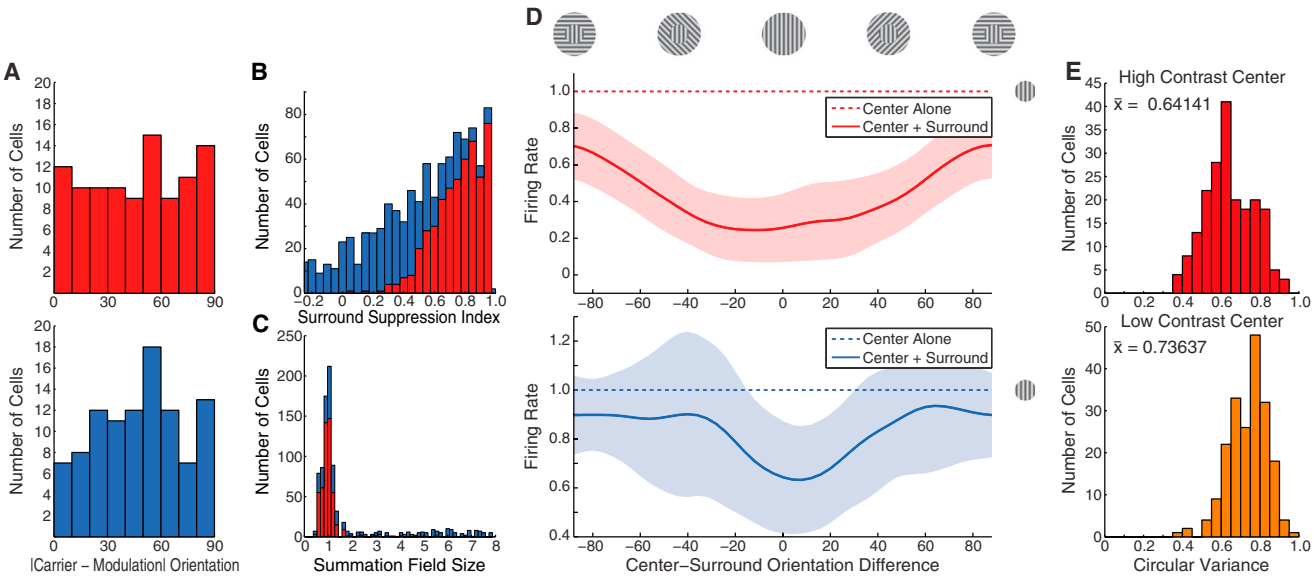

Figure 7. 2D Probabilistic Model: Further Results

(A) Histograms of differences between preferred luminance and CM orientations for E (red) and I (blue) units of Figure 6J for $c = 40$. The two preferred orientations were completely uncorrelated (E units, $r = 0.098$, $p = 0.33$ and I units, $r = 0.093$, $p = 0.36$).

(B) Distribution of SSI (see legend of Figure 6E) for E (red) and I (blue, shown above E units) units at 500 randomly selected sites of Figure 6E. SSI = 0, no suppression; SSI = 1, complete response suppression; and SSI <0, response facilitation. Mean ± SD, E units 0.75 ± 0.18 and I units 0.30 ± 0.35.

(C) Distribution of summation field sizes, same 500 E and 500 I units and colors as (B). Mean ± SD, E, 1.08° ± 0.18° and I, 4.97° ± 3.74°.

(D) Dependence of surround suppression on surround orientation for stimulus strength $c = 40$. Center stimulus at unit's preferred orientation fills summation field; surround at varying orientations relative to center stimulus (x axis) extends stimulus to total diameter 15.1° (70 grid spacings). Mean (solid lines) ± 1 SD (shaded region) of responses of 50 randomly selected E (top) or I (bottom) units, each normalized to response to center stimulus alone.

(E) Orientation tuning of surround suppression decreases for low-strength center. Histograms show circular variances (C.V.'s) of 1 minus the normalized orientation tuning curves of surround suppression (as in D) for the 50 E and 50 I units of (D), for center $c = 40$ (top) or $c = 10$ (bottom); surround $c = 40$ in both conditions. Mean C.V. ($\bar{x}$ in figure) increases significantly at low center strength, indicating broader orientation tuning. Mean ± SD of C.V.'s for high ($c = 40$) and low ($c = 10$) contrast and p values for difference between two distributions using 2-sided WRS test: all units, high 0.64 ± 0.11, low 0.74 ± 0.11, $p = 2.6 \times 10^{-9}$; E units, high 0.62 ± 0.10, low 0.77 ± 0.09, $p = 6.3 \times 10^{-10}$; and I units, high 0.67 ± 0.12, low 0.72 ± 0.12, $p = 0.034$.

The model qualitatively reproduces all of the results of the previous 1D models, but with more realistic variability. With increasing stimulus strength, (1) input shifts from externally-driven to network-driven (Figure 6B) with network input increasingly inhibition-dominated (Figure 6C), as in Figures 1E, 1F, 3A, and 3B; (2) response summation switches from supralinear to sublinear (Figure 6D), as in Figure 1I; and (3) surround suppression and periodicity in length-tuning curves develop (Figure 6E, average high-strength tuning curves; Figure 6F, sampling of diverse tuning curves of individual units across input strengths) and summation fields shrink (Figure 6G), as in Figures 3C and 3D. For weak center input strength, surround suppression weakens, and for smaller surrounds, can switch to surround facilitation (Figure 6H), as in Figure 3E. The periodicity in both length- and position-tuning curves is statistically significant (Figure 6I), as in the experimental data (Figures 4B and 4E). Preferred CM SF increases with stimulus strength (Figure 6J), as in model and experiment (Figures 5D–5G). Note that preferred CM SF for I units is uniformly 0 for smaller stimulus strengths, consistent with the linear model prediction that a nonzero I-unit resonant SF requires an ISN (Supplemental Text S2.1.1).

The model also reveals new results. There is no correlation between luminance and CM preferred orientations (Figure 7A), similar to experiments (Tanaka and Ohzawa, 2009). This is because CM preferred orientation arises as a network effect (the best orientation across 2D cortical space of the spatially periodic activity, determined in the model by random variations in intracortical connections), whereas CRF preferred orientation is

(H) Dependence of surround suppression on center stimulus strength and surround size for four example E units chosen to represent the diversity seen across units. For each unit, the center stimulus exactly filled its summation field. Surround stimulus strength $c = 40$.

(I) Applying the same procedures to model data (100 randomly selected E units) as to experimental data produces similar results: 98/100 units (length tuning, left) and 90/100 units (position tuning, right) are better fit by SSM model than DoG model ($p<0.01$, nested F-test). All conventions and analyses as in Figures 4B and 4E. Statistics for all units in Tables S4 and S5.

(J) Preferred CM SF versus stimulus strength for E (top) and I (bottom) units. Luminance grating is full-field at preferred orientation of center grid location. E/I units studied at 100 locations, the center and the 99 locations with preferred orientation closest to the center location's (all within 2°; spatially dispersed across the map). Mean (curves) ± SD (color). Due to limits of computing time, we studied CM SF tuning at fixed CM orientation (vertical across model cortex) and CM orientation tuning (Figure 7A) at fixed CM SF (0.3 cycles/degree).

the luminance orientation that best drives a cell's external input. The model shows a relatively broad distribution of surround suppression indices, akin to the variability observed experimentally (e.g., Walker et al., 2000) (Figure 7B), and of I-unit summation field sizes (Figure 7C), with I units having larger mean summation fields and weaker mean surround suppression than E units, as in Figures 2B, 2C, and 3C. Surround suppression is tuned for surround orientation (Figure 7D), with tuning that is weaker for a low-contrast versus high-contrast center (Figure 7E), both as observed in V1 (Cavanaugh et al., 2002b; Sengpiel et al., 1997; Ozeki et al., 2009).

DISCUSSION

The SSN provides a remarkably simple account, and the first unifying circuit account, of a wide variety of behaviors across multiple cortical areas. These include surround suppression, normalization, and their dependencies on contrast and other stimulus parameters (see multiple references in Introduction), as well as spatial periodicity in activity and length tuning (Anderson et al., 2001; Tanaka and Ohzawa, 2009; Wang et al., 2009). The model requires no fine tuning, producing qualitatively similar behavior over broad parameter regimes. Our first experimental tests provide strong support, for the first time demonstrating systematic periodicity in high-contrast length-tuning and position-tuning curves (the latter indirectly indicating spatial periodicity in activity), as well as an increase in the underlying SF of periodic activity with increasing contrast as measured by preferred CM SF.

The model depends on very few assumptions, most importantly a supralinear I/O function for single neurons and sufficiently strong recurrent excitation and feedback inhibition. It differs from previous circuit models (e.g., Schwabe et al., 2010; Somers et al., 1998, and models reviewed in Carandini and Heeger, 2012) in providing a unified network explanation of multiple aspects of both contextual modulation and normalization, exhibiting similar behaviors for both E and I cells, showing suppression and normalization without increases in inhibition, and explaining contrast-dependent behaviors without assuming a class of I neurons that are ineffective at lower contrasts.

Connection to the Balanced Network

As discussed in more detail in Ahmadian et al. (2013), in both the SSN and the balanced network model (van Vreeswijk and Sompolinsky, 1998), the dynamics robustly lead inhibition to stabilize excitation. However, the two models operate in very different regimes. In the balanced network, both external and network-driven inputs are very large, but are tightly balanced, leaving only a far smaller residual input. This predicts external input alone is much larger than net input, counter to results of isolating external input by silencing cortex (Priebe and Ferster, 2008). Due to tight balancing, the balanced network can only respond linearly to the input. In the SSN, inputs are not large, the balance is loose, and nonlinear behavior like that seen in cortex can result. In preliminary results with spiking models, SSN behavior is reproduced while, like the balanced network, producing asynchronous, irregular firing (D. Obeid and K.D.M., unpublished data).

Experimental Predictions

The model makes many experimental predictions beyond those we tested: (1) for linearly adding external inputs, cortical areas should show supralinear (weak input) or sublinear (strong input) response summation; optogenetically stimulating two distinct sets of neurons could ensure linear input addition; (2) periodicity in length- and positional-tuning should decrease in wavelength with increasing contrast, as shown here for CM tuning; (3) periodicity in length- and positional-tuning should attenuate or disappear as stimuli are changed from sharp-edged to slowly tapering, while CM tuning persists; (4 & 5) across a variety of normalization or suppression phenomena, (4) E and I cells should show similar behavior (both normalized or both suppressed); however, this may be confounded by multiple I-cell subtypes with differing responses, so a more robust prediction (Supplemental Text S2.2.3) is (5) response suppression in E cells should be accompanied by a decrease in the I conductance they receive; and (6) the summation field for directional tuning in MT should shrink with contrast.

A seventh prediction is that ISN behavior should occur only for lower spatial frequencies of input to I cells, along with sufficient network activation to drive the network into the ISN regime (Supplemental Text S2.2). A key ISN behavior is the "paradoxical" response of I cells: addition of excitatory drive to I cells causes them to *lower* their firing rates in the new steady state (Ozeki et al., 2009; Tsodyks et al., 1997). Thus, if channelrhodopsin-2 (ChRh2) were expressed in I neurons, and a light pattern of a given SF were modulated or drifted at low temporal frequency while a visual stimulus was presented, the network should show paradoxical response only for sufficient visual contrast and then only for spatial frequencies of light below a critical frequency k_{cr} (Figure 8). This predicts a sharp jump, with increasing SF, of about 180° in the relative phase of E and I cell activities as k_{cr} is crossed, or more robustly (Supplemental Text S2.2.3), in the relative phases of the E and I conductances received by E cells.

We also note several caveats. In some species or areas, spontaneous activity may suffice to drive the network out of the supralinearly summating regime. Periodicity in length- and position-tuning curves depends on sharp-edged input, but this might not correspond directly to stimulus shape: connection fan-in and fan-out at previous stages could spatially smooth input from sharp-edged stimuli, while processing (e.g., surround suppression) at previous stages could sharpen input edges for smoothly tapering stimuli. Because I cells have wider summation fields than E cells, intermediate stimulus sizes can suppress E cells, but facilitate I cells (see Discussion of results of Haider et al., 2010, below). In parameter regimes in which I projections are not too narrow, both E and I cells can be surround suppressed with *increases* in the inhibition they receive: inhibition from new I cells recruited by a larger stimulus can outweigh loss of inhibition from suppressed I cells. Other factors that can dynamically change effective synaptic strengths–short-term synaptic depression or facilitation, adaptation currents–may add complexity to model behavior, but will not alter the basic SSN distinction between weak- and strong-effective-synapse regimes.

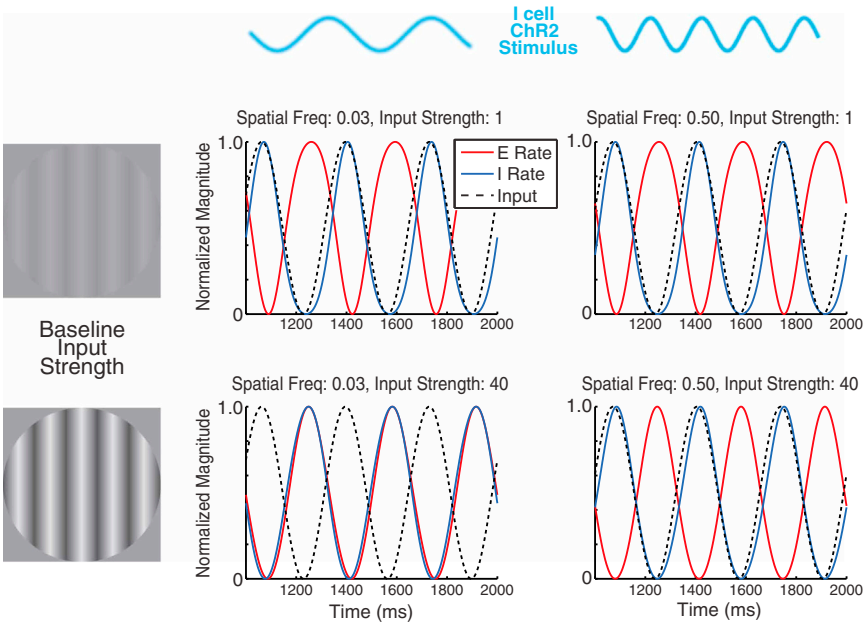

Figure 8. Spatial-Frequency- and Contrast-Dependent Paradoxical Response in the 2D Nonlinear Model

Slowly drifting, spatially sinusoidal modulatory input is given to I units (e.g., by photostimulation with ChRh2 expressed in I cells), in the presence of varying levels of spatially uniform tonic visual input driving both E and I units. "Paradoxical" ISN behavior–I firing rates decreasing for increased input to I units–manifests as E and I units modulating in phase with one another. For weak tonic input, the network is a non-ISN and units respond nonparadoxically (modulatory input and I in phase, E at opposite phase) for all modulatory spatial frequencies. For high tonic input, network is an ISN. Then low-spatial-frequency, but not high-spatial-frequency modulation drives units paradoxically (Supplemental Text S2.2 and Figure S2C). A more robust prediction is that these changes in relative phase will occur in the excitation and inhibition received by cells (Supplemental Text S2.2.3). Modulatory input and E and I firing rates are all shown normalized to both their minimum and maximum values.

Does the SSN Model Apply to Rodent Cortex?

We have primarily modeled data from species with columnar organization and maps of features such as preferred orientation. Does our model apply to species, such as rodents, that lack such organization?

Recurrent excitation in rodents may be weaker than in species with columnar organization, so that excitatory instability and the transition to sublinear behavior may not occur. This is suggested by results of Atallah et al. (2012) in mouse V1 L2/3: optogenetic suppression of parvalbumin (PV)-expressing I cells increased E-cell visual responses without any increase in the excitatory conductance they received and with a nonparadoxical increase in inhibitory conductance, suggesting a dearth of E → E coupling and non-ISN behavior. This could explain why maps fail to develop in rodents, as such failure can occur if local interactions between neurons are suppressive (Kaschube, 2014). However, engagement of L2/3 excitatory connectivity may vary with experimental conditions or area. In rodent auditory cortex, locomotion added drive to L1 I neurons, suppressing L2/3 E-cell firing with a paradoxical suppression of inhibitory conductance they received, suggesting an ISN (Zhou et al., 2014). Other results suggest strong recurrent excitation and ISN-like behavior in L5 of rodent cortex (London et al., 2010; Stroh et al., 2013); rodent response properties might be synthesized in deep layers by SSN mechanisms and propagate to upper layers.

Adesnik et al. (2012) found in mouse V1 L2/3 that somatostatin-expressing I cells (SOM cells) were surround facilitated, while E and PV cells were suppressed, suggesting a non-ISN in which increased SOM inhibition mediates suppression (Nienborg et al., 2013). However, suppression might decrease the net inhibition (SOM + PV) cells receive, as in an ISN; optogenetic suppression of SOM-cell spiking only moderately reduced E-cell surround suppression; and another study found both SOM and PV neurons were surround suppressed (Pecka et al., 2014). The relative sparsity of SOM cells and increased proportion of PV cells in macaque versus mouse V1 (reviewed in Nienborg et al., 2013) is another potentially significant species difference.

A Conflicting Experiment?

The model suggests a resolution to the apparent conflict between two findings: inhibition decreased during surround suppression (Ozeki et al., 2009); yet increased stimulus size in windowed natural movies suppressed E cell firing, while *increasing* the inhibition they receive and PV cell firing (Haider et al., 2010). Haider et al. (2010) used small stimuli: for a given cell, center stimulus size was that giving half-maximal response, which for a Gaussian-shaped CRF is about 0.5-0.6 × CRF size (Supplemental Methods S1.3.4); large stimuli were three times larger, or 1.5-1.8 × CRF size (versus surrounds typically 10 × CRF size in Ozeki et al., 2009). PV cells have larger summation fields than E cells in mice (Adesnik et al., 2012) and our model (Figure 7C). Thus, Haider et al. (2010)'s larger stimuli, (1) to E cells might have size close to optimal for I cells; and (2) to I cells might evoke more response than center stimuli, even if optimal size were in between. Figure S14 shows how the model could simultaneously produce the results of both studies. The broad spatiotemporal power spectrum of natural stimuli may also contribute: paradoxical effects arise only at lower spatial frequencies (Figure 8) and similar dependence might occur for temporal frequency.

Extension to Other Cortical Properties

The network's winner-take-all property for unequal-strength inputs may explain suppression of correlated neural variability induced by a sensory stimulus or motor plan (Churchland et al., 2010) or attention (Cohen and Maunsell, 2009; Mitchell et al., 2009): increasing strength of other inputs (stimulus, plan, or attention) suppresses the contribution of correlated neural noise to neuronal output. Multiple attentional effects on neural

responses arise if attention modulates inputs to a normalizing circuit (e.g., Reynolds and Heeger, 2009); the SSN model is likely to reproduce these effects. Future studies will address these issues.

Attentional enhancement and modulatory suppression can be understood as opposite turns of a "knob" that adjusts the gain of "balanced amplification" (Murphy and Miller, 2009), which arises in the ISN regime: a small network shift toward inhibition (e.g., addition of modulatory E input to I cells) causes a large decrease in both E- and I-cell responses, while a small shift toward excitation causes large increases in both (these changes can be multiplicative, i.e., gain changes, in the SSN; Figure S13). Thus, a function of strong cortical recurrence may be to provide modulatable amplification.

Conclusions

The SSN provides a powerful framework for understanding how sensory cortex globally integrates multiple sources of input, bottom-up and top-down, to produce neuronal responses and ultimately perception. The computational function of these integrative behaviors may now be more deeply probed by studying how the underlying circuit processes more complex and natural stimuli. Circuit changes that cause failures of this basic circuit operation might manifest at multiple cortical levels from primary sensation to higher cognition. Understanding such failures may provide insight into disorders such as autism and schizophrenia, which show deficits in contextual (Silverstein and Keane, 2011) or global (Qian and Lipkin, 2011) processing and involve disruptions in E/I balance (Yizhar et al., 2011; Yoon et al., 2010) that could disrupt the balanced amplification underlying SSN modulations. Indeed, schizophrenics show reduced visual surround suppression that correlates with reduced gamma-amino-butyric acid (GABA) concentration in visual cortex (Yoon et al., 2010), while autistic subjects show increased variability in sensory responses (Dinstein et al., 2012), which might reflect failure of normalization-induced variability suppression.

EXPERIMENTAL PROCEDURES

Animal care protocols conformed to NIH guidelines and were approved by the Brandeis University Institutional Animal Care and Use Committee. Methods are found in Supplemental Methods, section S1.

SUPPLEMENTAL INFORMATION

Supplemental Information includes Supplemental Methods, Supplemental Text, fourteen figures, and five tables and can be found with this article online at http://dx.doi.org/10.1016/j.neuron.2014.12.026.

AUTHOR CONTRIBUTIONS

D.B.R. and K.D.M. developed the model and worked together on analysis and simulations. D.B.R. wrote and executed all code and made all figures. Experiments were designed by all authors, performed by D.B.R. and S.V.H., and analyzed by D.B.R. in interaction with K.D.M. and S.V.H. K.D.M. and D.B.R. wrote the manuscript, with comments and contributions from S.V.H.

ACKNOWLEDGMENTS

We thank Larry Abbott, Yashar Ahmadian, Anne Churchland, David Ferster, Mark Goldman, Giancarlo LaCamera, Ashok Litwin-Kumar, Arianna Maffei, and Steve Siegelbaum for helpful comments; Liam Paninski for help with analysis of experimental data; and Jared Clemens for help with physiological recordings. Work supported by R01-EY11001 to K.D.M.; the Gatsby Charitable Foundation (K.D.M.); Medical Scientist Training Program grant 5 T32 GM007367-36 (D.B.R.); and a faculty startup grant from NIH P30NS069339 and grants from the Massachusetts Life Sciences Center and the John Merck Foundation (S.V.H.).

Accepted: December 9, 2014
Published: January 21, 2015

REFERENCES

Adesnik, H., Bruns, W., Taniguchi, H., Huang, Z.J., and Scanziani, M. (2012). A neural circuit for spatial summation in visual cortex. Nature *490*, 226–231.

Adini, Y., Sagi, D., and Tsodyks, M. (1997). Excitatory-inhibitory network in the visual cortex: psychophysical evidence. Proc. Natl. Acad. Sci. USA *94*, 10426–10431.

Ahmadian, Y., Rubin, D.B., and Miller, K.D. (2013). Analysis of the stabilized supralinear network. Neural Comput. *25*, 1994–2037.

Anderson, J.S., Lampl, I., Gillespie, D.C., and Ferster, D. (2001). Membrane potential and conductance changes underlying length tuning of cells in cat primary visual cortex. J. Neurosci. *21*, 2104–2112.

Atallah, B.V., Bruns, W., Carandini, M., and Scanziani, M. (2012). Parvalbumin-expressing interneurons linearly transform cortical responses to visual stimuli. Neuron *73*, 159–170.

Busse, L., Wade, A.R., and Carandini, M. (2009). Representation of concurrent stimuli by population activity in visual cortex. Neuron *64*, 931–942.

Carandini, M., and Heeger, D.J. (2012). Normalization as a canonical neural computation. Nat. Rev. Neurosci. *13*, 51–62.

Cavanaugh, J.R., Bair, W., and Movshon, J.A. (2002a). Nature and interaction of signals from the receptive field center and surround in macaque V1 neurons. J. Neurophysiol. *88*, 2530–2546.

Cavanaugh, J.R., Bair, W., and Movshon, J.A. (2002b). Selectivity and spatial distribution of signals from the receptive field surround in macaque V1 neurons. J. Neurophysiol. *88*, 2547–2556.

Cavanaugh, J., Joiner, W.M., and Wurtz, R.H. (2012). Suppressive surrounds of receptive fields in monkey frontal eye field. J. Neurosci. *32*, 12284–12293.

Churchland, M.M., Yu, B.M., Cunningham, J.P., Sugrue, L.P., Cohen, M.R., Corrado, G.S., Newsome, W.T., Clark, A.M., Hosseini, P., Scott, B.B., et al. (2010). Stimulus onset quenches neural variability: a widespread cortical phenomenon. Nat. Neurosci. *13*, 369–378.

Cohen, M.R., and Maunsell, J.H. (2009). Attention improves performance primarily by reducing interneuronal correlations. Nat. Neurosci. *12*, 1594–1600.

Dinstein, I., Heeger, D.J., Lorenzi, L., Minshew, N.J., Malach, R., and Behrmann, M. (2012). Unreliable evoked responses in autism. Neuron *75*, 981–991.

Ermentrout, G.B., and Terman, D.H. (2010). Mathematical Foundations of Neuroscience. (New York: Springer).

Falkner, A.L., Krishna, B.S., and Goldberg, M.E. (2010). Surround suppression sharpens the priority map in the lateral intraparietal area. J. Neurosci. *30*, 12787–12797.

Gilbert, C.D., and Wiesel, T.N. (1989). Columnar specificity of intrinsic horizontal and corticocortical connections in cat visual cortex. J. Neurosci. *9*, 2432–2442.

Haider, B., Krause, M.R., Duque, A., Yu, Y., Touryan, J., Mazer, J.A., and McCormick, D.A. (2010). Synaptic and network mechanisms of sparse and reliable visual cortical activity during nonclassical receptive field stimulation. Neuron *65*, 107–121.

Hansel, D., and van Vreeswijk, C. (2002). How noise contributes to contrast invariance of orientation tuning in cat visual cortex. J. Neurosci. *22*, 5118–5128.

Heuer, H.W., and Britten, K.H. (2002). Contrast dependence of response normalization in area MT of the rhesus macaque. J. Neurophysiol. *88*, 3398–3408.

Kapfer, C., Glickfeld, L.L., Atallah, B.V., and Scanziani, M. (2007). Supralinear increase of recurrent inhibition during sparse activity in the somatosensory cortex. Nat. Neurosci. *10*, 743–753.

Kaschube, M. (2014). Neural maps versus salt-and-pepper organization in visual cortex. Curr. Opin. Neurobiol. *24*, 95–102.

London, M., Roth, A., Beeren, L., Häusser, M., and Latham, P.E. (2010). Sensitivity to perturbations in vivo implies high noise and suggests rate coding in cortex. Nature *466*, 123–127.

MacEvoy, S.P., Tucker, T.R., and Fitzpatrick, D. (2009). A precise form of divisive suppression supports population coding in the primary visual cortex. Nat. Neurosci. *12*, 637–645.

Mariño, J., Schummers, J., Lyon, D.C., Schwabe, L., Beck, O., Wiesing, P., Obermayer, K., and Sur, M. (2005). Invariant computations in local cortical networks with balanced excitation and inhibition. Nat. Neurosci. *8*, 194–201.

Miller, K.D., and Troyer, T.W. (2002). Neural noise can explain expansive, power-law nonlinearities in neural response functions. J. Neurophysiol. *87*, 653–659.

Mitchell, J.F., Sundberg, K.A., and Reynolds, J.H. (2009). Spatial attention decorrelates intrinsic activity fluctuations in macaque area V4. Neuron *63*, 879–888.

Murphy, B.K., and Miller, K.D. (2009). Balanced amplification: a new mechanism of selective amplification of neural activity patterns. Neuron *61*, 635–648.

Nienborg, H., Hasenstaub, A., Nauhaus, I., Taniguchi, H., Huang, Z.J., and Callaway, E.M. (2013). Contrast dependence and differential contributions from somatostatin- and parvalbumin-expressing neurons to spatial integration in mouse V1. J. Neurosci. *33*, 11145–11154.

Ozeki, H., Finn, I.M., Schaffer, E.S., Miller, K.D., and Ferster, D. (2009). Inhibitory stabilization of the cortical network underlies visual surround suppression. Neuron *62*, 578–592.

Pecka, M., Han, Y., Sader, E., and Mrsic-Flogel, T.D. (2014). Experience-dependent specialization of receptive field surround for selective coding of natural scenes. Neuron *84*, 457–469.

Priebe, N.J., and Ferster, D. (2008). Inhibition, spike threshold, and stimulus selectivity in primary visual cortex. Neuron *57*, 482–497.

Qian, N., and Lipkin, R.M. (2011). A learning-style theory for understanding autistic behaviors. Front. Hum. Neurosci. *5*, 77.

Reynolds, J.H., and Heeger, D.J. (2009). The normalization model of attention. Neuron *61*, 168–185.

Sachdev, R.N., Krause, M.R., and Mazer, J.A. (2012). Surround suppression and sparse coding in visual and barrel cortices. Front Neural Circuits *6*, 43.

Sceniak, M.P., Ringach, D.L., Hawken, M.J., and Shapley, R. (1999). Contrast's effect on spatial summation by macaque V1 neurons. Nat. Neurosci. *2*, 733–739.

Schwabe, L., Ichida, J.M., Shushruth, S., Mangapathy, P., and Angelucci, A. (2010). Contrast-dependence of surround suppression in Macaque V1: experimental testing of a recurrent network model. Neuroimage *52*, 777–792.

Sengpiel, F., and Vorobyov, V. (2005). Intracortical origins of interocular suppression in the visual cortex. J. Neurosci. *25*, 6394–6400.

Sengpiel, F., Sen, A., and Blakemore, C. (1997). Characteristics of surround inhibition in cat area 17. Exp. Brain Res. *116*, 216–228.

Shao, Y.R., Isett, B.R., Miyashita, T., Chung, J., Pourzia, O., Gasperini, R.J., and Feldman, D.E. (2013). Plasticity of recurrent l2/3 inhibition and gamma oscillations by whisker experience. Neuron *80*, 210–222.

Shushruth, S., Ichida, J.M., Levitt, J.B., and Angelucci, A. (2009). Comparison of spatial summation properties of neurons in macaque V1 and V2. J. Neurophysiol. *102*, 2069–2083.

Silverstein, S.M., and Keane, B.P. (2011). Perceptual organization impairment in schizophrenia and associated brain mechanisms: review of research from 2005 to 2010. Schizophr. Bull. *37*, 690–699.

Somers, D.C., Todorov, E.V., Siapas, A.G., Toth, L.J., Kim, D.S., and Sur, M. (1998). A local circuit approach to understanding integration of long-range inputs in primary visual cortex. Cereb. Cortex *8*, 204–217.

Song, X.M., and Li, C.Y. (2008). Contrast-dependent and contrast-independent spatial summation of primary visual cortical neurons of the cat. Cereb. Cortex *18*, 331–336.

Stroh, A., Adelsberger, H., Groh, A., Rühlmann, C., Fischer, S., Schierloh, A., Deisseroth, K., and Konnerth, A. (2013). Making waves: initiation and propagation of corticothalamic Ca2+ waves in vivo. Neuron *77*, 1136–1150.

Sundberg, K.A., Mitchell, J.F., and Reynolds, J.H. (2009). Spatial attention modulates center-surround interactions in macaque visual area v4. Neuron *61*, 952–963.

Tanaka, H., and Ohzawa, I. (2009). Surround suppression of V1 neurons mediates orientation-based representation of high-order visual features. J. Neurophysiol. *101*, 1444–1462.

Teichert, T., Wachtler, T., Michler, F., Gail, A., and Eckhorn, R. (2007). Scale-invariance of receptive field properties in primary visual cortex. BMC Neurosci. *8*, 38.

Tsodyks, M.V., Skaggs, W.E., Sejnowski, T.J., and McNaughton, B.L. (1997). Paradoxical effects of external modulation of inhibitory interneurons. J. Neurosci. *17*, 4382–4388.

Tsui, J.M., and Pack, C.C. (2011). Contrast sensitivity of MT receptive field centers and surrounds. J. Neurophysiol. *106*, 1888–1900.

Van den Bergh, G., Zhang, B., Arckens, L., and Chino, Y.M. (2010). Receptive-field properties of V1 and V2 neurons in mice and macaque monkeys. J. Comp. Neurol. *518*, 2051–2070.

van Vreeswijk, C., and Sompolinsky, H. (1998). Chaotic balanced state in a model of cortical circuits. Neural Comput. *10*, 1321–1371.

Vanni, M.P., and Casanova, C. (2013). Surround suppression maps in the cat primary visual cortex. Front Neural Circuits *7*, 78.

Walker, G.A., Ohzawa, I., and Freeman, R.D. (2000). Suppression outside the classical cortical receptive field. Vis. Neurosci. *17*, 369–379.

Wang, C., Bardy, C., Huang, J.Y., FitzGibbon, T., and Dreher, B. (2009). Contrast dependence of center and surround integration in primary visual cortex of the cat. J. Vis. *9*, 1–15.

Yizhar, O., Fenno, L.E., Prigge, M., Schneider, F., Davidson, T.J., O'Shea, D.J., Sohal, V.S., Goshen, I., Finkelstein, J., Paz, J.T., et al. (2011). Neocortical excitation/inhibition balance in information processing and social dysfunction. Nature *477*, 171–178.

Yoon, J.H., Maddock, R.J., Rokem, A., Silver, M.A., Minzenberg, M.J., Ragland, J.D., and Carter, C.S. (2010). GABA concentration is reduced in visual cortex in schizophrenia and correlates with orientation-specific surround suppression. J. Neurosci. *30*, 3777–3781.

Zhou, M., Liang, F., Xiong, X.R., Li, L., Li, H., Xiao, Z., Tao, H.W., and Zhang, L.I. (2014). Scaling down of balanced excitation and inhibition by active behavioral states in auditory cortex. Nat. Neurosci. *17*, 841–850.

Neuron

Supplemental Information

The Stabilized Supralinear Network: A Unifying Circuit Motif Underlying Multi-Input Integration in Sensory Cortex

Daniel B. Rubin, Stephen D. Van Hooser, and Kenneth D. Miller

Supplementary materials for:

The stabilized supralinear network: A unifying circuit motif underlying multi-input integration in sensory cortex

Daniel B. Rubin, Stephen D. Van Hooser, and Kenneth D. Miller

Contents

List of Figures

List of Tables

S1 Methods

We first present in brief the information needed to replicate our results, excepting the details of the maximum likelihood estimation (MLE) procedure (Sections S1.1-S1.2). We then present supplemental modeling information (Sections S1.3-S1.4), including the MLE details in Section S1.4.2.

S1.1 Modeling Methods in Brief

We define the Gaussian $G_\sigma(x,y) = e^{-\frac{d(x,y)^2}{2\sigma^2}}$, where for positions $d(x,y) = |x-y|$, for orientations $d(x,y) =$ shortest distance around circle of circumference 180^o between x and y. We define $\sim \mathcal{N}(m,\sigma^2)$ to mean distributed as a normal distribution with mean m, variance σ^2.

S1.1.1 Determination of external input shape $h(x)$

Input of length l had shape $s_l(x) = \left(\frac{1}{1+e^{-\frac{x+l/2}{\sigma_\text{RF}}}}\right)\left(1-\frac{1}{1+e^{-\frac{x-l/2}{\sigma_\text{RF}}}}\right)$. Fig. 1: stimulus of orientation ϕ had $h(\theta) = G_{\sigma_\text{FF}}(\phi,\theta)$. Figs. 2-3: $h(x) = s_l(x)$. Figs. 6-8: stimulus centered at 2D position $\mathbf{x}'$, orientation ϕ has $h(\mathbf{x}) = s_l(|\mathbf{x}-\mathbf{x}'|)G_{\sigma_\text{FF}}(\phi,\theta(\mathbf{x}))$ ($\theta(\mathbf{x})$ is preferred orientation of units at 2D position $\mathbf{x}$). For full-field gratings, $s_l(\cdot)$ is replaced by 1.

S1.1.2 Parameters

All figs: $\tau_E = 20$ms, $\tau_I = 10$ms.
Figs. 1,2,3: there are N E/I units with grid spacing $\Delta\theta$ (Fig. 1) or Δx (Figs. 2,3).
Fig. 1: Connections are $W_{ab}(\theta-\theta') = J_{ab}G_{\sigma_\text{ori}}(\theta,\theta')$. $N = 180$, $\Delta\theta = 1^\text{o}$, $J_{EE} = 0.044$, $J_{IE} = 0.042$, $J_{EI} = 0.023$, $J_{II} = 0.018$, $\sigma_\text{ori} = 32^\text{o}$, $\sigma_{FF} = 30^\text{o}$, $k = 0.04$, $n = 2.0$.
Figs. 2,3: Excitatory projections are $W_{aE}(x,x') = J_{aE}G_{\sigma_{aE}}(x,x')$ for $a \in \{E,I\}$. Inhibitory projections W_{aI} are only to same grid position as projecting neuron. **Figure 2**: $N = 401$, $\Delta x = 0.25^\text{o}$, $\sigma_\text{RF} = 0.33\Delta x$, $J_{EE} = 0.385$, $J_{IE} = 1.0$, $W_{EI} = 0.55$, $W_{II} = 1.5$, $\sigma_{EE} = 0.5^\text{o}$, $\sigma_{IE} = 1^\text{o}$, $c = 1$. **Figure 3:** $N = 101$, $\Delta x = \frac{1}{3}^\text{o}$, $\sigma_\text{RF} = 0.125\Delta x$, $J_{EE} = 1.0$, $J_{IE} = 1.25$, $W_{EI} = 1.0$, $W_{II} = 0.75$, $\sigma_{EE} = \frac{2}{3}^\text{o}$, $\sigma_{IE} = \frac{4}{3}^\text{o}$, $k = 0.01$, $n = 2.2$.
Figs. 6,7: Grid is 75×75 E/I pairs, grid interval $\Delta x = \frac{16}{75}^\text{o}$, periodic boundary conditions. The map of preferred orientations $\theta(\mathbf{x})$ ($\mathbf{x}$ is 2D position) is randomly generated using the method of Kaschube et al. (2010) (their supp. materials, Eq. 20) with $n = 30$, $k_c = \frac{8 \text{ cycles}}{75 \text{ grid intervals}}$. Let $W_{ab}(\mathbf{x},\mathbf{x}')$ be synaptic weight from unit of type b (E or I), position $\mathbf{x}'$ to type a, position $\mathbf{x}$. Nonzero connections are sparse, chosen with probability $p\left(W_{ab}(\mathbf{x},\mathbf{x}') \neq 0\right) = \kappa_b G_{\sigma_{aE}}(x,x')G_{\sigma_\text{ori}}(\theta(\mathbf{x}),\theta(\mathbf{x}'))$. For nonzero connections, $W_{ab}(\mathbf{x},\mathbf{x}')$ is $\sim \mathcal{N}(J_{ab},(0.25J_{ab})^2)$; negative weights are set to zero. Weights of a given type b onto each unit are then scaled so that all units of a given type a receive the same total type b synaptic weight, equal to J_{ab} times the mean number of connections received under $p\left(W_{ab}(x,x') \neq 0\right)$. τ_E, τ_I, n_E, n_I, and k are $\sim \mathcal{N}(m,(0.05m)^2)$ where m is the corresponding mean value. n_E

and n_I are exponents of power law for E or I cells respectively. Parameters (mean values if stochastic): $\kappa_E = 0.1$, $\kappa_I = 0.5$, $J_{EE} = 0.10$, $J_{IE} = 0.38$, $J_{EI} = 0.089$, $J_{II} = 0.096$, $k = 0.012$, $n_E = 2.0$, $n_I = 2.2$, $\sigma_{EE} = 8\Delta x$, $\sigma_{IE} = 12\Delta x$, $\sigma_{EI} = \sigma_{II} = 4\Delta x$, $\sigma_{ori} = 45^{\rm o}$, $\sigma_{FF} = 32^{\rm o}$, $\sigma_{\rm RF} = \Delta x$.

Figs. 2,3,6: CM tuning is studied using a full-field grating multiplied by the contrast modulation $\frac{1}{2}\left(1 + \sin\left(2\pi\left(k \cdot x + \omega t\right)\right)\right)$ where x and k are 1D in Figs. 2 and 3 and 2D in Fig. 6 and $\omega = 4Hz$. Stimulus was run for 1 sec (1ms time steps). Preferred CM spatial frequency (SF), and preferred CM orientation in Fig. 6, were those producing maximum peak response over that time.

In Fig. 6, there were problems with units having response peaks of similar heights for multiple harmonics of a fundamental preferred SF. For this figure, we defined CM preferred SF as follows. We Fourier transformed the CM SF tuning curve and found its peak X, a number representing cycles/(tuning curve). Let f be the highest frequency in the CM SF tuning curve. We then successively looked at intervals of the tuning curve 0 to Nf/X, $N = 1, 2, \ldots,$ floor(X) followed by the full interval, looking for a response peak that was at least 95% of the height of the global peak of the tuning curve. The first such peak that was found was deemed the preferred SF. Visual inspection of many tuning curves confirmed that this procedure correctly isolated the fundamental of a harmonic stack of similar responses and otherwise simply found the peak of the tuning curve.

Figure 8: Parameters as in Fig. 6. All stimuli are full field. Photostimulus drifted at 3 Hz. Low input: tonic input 1, modulatory amplitude 1. High input: tonic input 40, modulatory amplitude 10. Spatial frequencies: 0.03 c/deg (low), 0.5 c/deg (high). Illustrated E/I pair chosen at random; grating at preferred orientation. Photostimulus oriented vertically across model cortex as shown in Fig. 6A.

S1.1.3 Simulation methods

For the linear model, the steady state can be explicitly determined. Using matrix/vector notation, letting $\mathbf{r}$ be the vector of firing rates of all units across the network (both E and I), $\mathbf{h}$ the vector of their external inputs, $\mathbf{W}$ the matrix of connection weights between these neurons and $\mathbf{1}$ the identity matrix of the same dimension, the steady state activities $\mathbf{r}_{\rm SS}$ are given by $\mathbf{r} = (\mathbf{1} - \mathbf{W})^{-1}\mathbf{h}$, which was numerically calculated. For the nonlinear models, steady states (and dynamics in CM-tuning simulations, Fig. 8, and Supplemental Fig. S2C) were determined by simulations using simple forward Euler method with 1 ms time step. All simulations were run from multiple initial conditions to confirm independence of final state from initial condition and tested with shorter time steps to ensure no changes in results.

S1.1.4 Tuning curve plots

All model tuning curves linearly connect points sampled at high resolution, without smoothing.

S1.2 Experimental Methods in Brief

S1.2.1 Animal care, surgery, and recording

Animal care protocols conformed to NIH guidelines and were approved by the Brandeis University Institutional Animal Care and Use Committee. Eight adult ferrets (90-110 days of age; 7 females, 1 male) were studied. They were singly or doubly housed and kept on a 12 hour light/12 hour dark cycle. Anesthesia was induced with a mix of ketamine (30 mg/kg) and xylazine (3.0 mg/kg) (IM) and maintained with 0.5–1.5% isoflurane. Atropine (0.2 ml, 0.5 mg/ml) was administered. All wound margins were infused with the long-lasting analgesic bupivicane (0.25%). A nylon tracheal tube was inserted by tracheotomy, and animals respirated on a 2:3 mixture of oxygen:nitrous oxide, switched to 1:1 after surgeries. Silicon oil was placed on the eyes to prevent corneal damage. The animal was secured in a stereotaxic frame, a small craniotomy (4×8 mm wide) was made and the dura removed. Ferrets were then paralyzed with continuous IP infusion of gallamine triethiodide (0.2mg/hr) to suppress spontaneous eye movements and respirated with a 1:1 mixture of oxygen:nitrous oxide. Heart rate, end-tidal CO_2 (maintained between 3.2% - 5.0%), and temperature were monitored continuously throughout surgeries and recordings.

Extracellular signals were recorded from upper layers of ferret V1 using carbon fiber microelectrodes (Kation Scientific).

S1.2.2 Visual stimulus protocols

Receptive field mapping: After initial coarse mapping of the CRF and preferred orientation, we determined CRF center (by switching between circular and complementary annular stimulus, progressively shrinking radius while searching for position that gave response to circular but not annular stimulus), then preferred direction (drifting gratings of 16 directions, 22.5° steps, spatial frequency 0.1 cycles/deg, temporal frequency 4 Hz), and then preferred spatial frequency (SF) (preferred-direction gratings of 7 SF's). Then studies of length, position, and CM tuning were carried out.

Tuning studies: Luminance gratings always had cell's preferred orientation, direction, and spatial frequency. For length tuning (30 stimuli, radius 1° to 30° by 1°) and position tuning (21 30°-diameter stimuli, position $-15°$ to 15° by 1.5°, moved parallel to grating orientation), stimuli were presented for 2 sec, drift rate 4 Hz, interstimulus interval (ISI) 4 sec. Response measure was mean firing rate during grating presentation. CM grating varied contrast sinusoidally from 0% contrast to luminance-grating contrast. We first found CM preferred orientation (among 8 orientations, 22.5° spacing) with 70% luminance contrast and CM SF 0.05 cycles/deg. This CM orientation was used to study CM SF tuning across luminance contrasts (24 stimuli: SFs 01, .015, .02, .03, .04, .05 c/deg; contrasts 4%, 8%, 16%, 64%). CM stimuli were presented for 4 seconds, drift rates 4 Hz (luminance), 1 Hz (CM), ISI 4 sec. Response measure was 1 Hz component of firing rate during CM grating presentation. For each tuning type, stimuli were presented in pseudorandom order; each stimulus appeared 4–5 times.

S1.2.3 Maximum likelihood estimation (MLE) and DOG and SSM models

We used MLE to improve our estimates of tuning curves by removing the effects of slow, stimulus-independent variations in excitability. Details are in Section S1.4.2.

For Fig. 4 and Fig. 6I, SSM and DOG curves were defined as follows. The error function is defined by $\mathrm{erf}(x) = \frac{2}{\sqrt{\pi}} \int_0^x dz\, e^{-z^2}$, and ranges from -1 to 1. We define the non-negative function $z(x) = (\mathrm{erf}(x) + 1)/2$. For size-tuning curves $r(x)$, the DoG model is $r(x) = a_1 z((x - a_2)\, a_3) - a_4 z((x - a_5)\, a_6)\, e^{a_7 x} + a_8$. The SSM model eliminates the a_8 term and replaces e^{a_7} with $(e^{a_7 x} \cos(a_9 x + a_{10}) + a_8)$. (Note that setting $a_9 = a_{10} = 0$ reduces the SSM model to same form as the DOG model, as becomes clear if the equations are reexpressed in terms of $\mathrm{erf}(x)$ rather than $z(x)$; that is, the models are nested.) For position-tuning curves $p(x)$, the DoG model is $p(x) = a_1 e^{\frac{-(x-a_2)^2}{2a_3^2}} - a_4 e^{\frac{-(x-a_5)^2}{2a_6^2}} + a_7$. The SSM model replaces a_4 with $a_4(\cos(a_8 x + a_9) + a_{10})$. SSM and DOG models were fit by minimizing sum-squared error using the Matlab function lsqcurvefit.

S1.3 Supplemental Methods Information: Modeling

S1.3.1 External input shape: General considerations and supplementary figures

We adopted the function $s_l(x)$ that defines "sharp-edged" stimuli (Section S1.1.1) early in our work, but it is very similar to the form that would be obtained by assuming that the spatial envelope of the CRF is given by a Gaussian function of retinotopic space and that the external input to a given cell is the integral of the product of its Gaussian CRF with the stimulus. If we let the Gaussian CRF have standard deviation σ_{G} and assume a sharp-edged stimulus constant over $x = -l$ to $x = l$, this integral is proportional to $f_l(x) = \frac{1}{2}\left(\mathrm{erf}\left(\frac{x+l/2}{\sigma_{\mathrm{G}}\sqrt{2}}\right) + \mathrm{erf}\left(\frac{l/2-x}{\sigma_{\mathrm{G}}\sqrt{2}}\right)\right)$. Identifying $\sigma_{\mathrm{RF}} = 0.6\sigma_{\mathrm{G}}$, $s_l(x)$ and $f_l(x)$ are essentially identical for $\sigma_{\mathrm{RF}} < 0.25l$, a condition that holds for almost all of our stimuli. As σ_{RF} increases from $0.25l$ to l, $s_l(x)$ becomes about 10% wider than $f_l(x)$ (half width at half height) and its amplitude relative to $f_l(x)$ decreases to about $0.6 f_l(x)$.

In Supplemental Figs. S7 and S8, we also considered more smoothly-tapering stimuli. For Gaussian-shaped stimuli of length l, $h(x) = g_l(x)$ where $g_l(x) = e^{-\frac{x^2}{2\sigma_l^2}}$ with $\sigma_l = \frac{l/2}{\sqrt{2*\ln(2)}}$ (l is full-width at half-height of the input). We considered varying degrees of tapering by linearly interpolating between $s_l(x)$ and $g_l(x)$ to produce input profiles $h(x) = a s_l(x) + (1 - a) g_l(x)$ with $a = 0, 0.2, 0.4, 0.6, 0.8, 1.0$.

Throughout the paper, external input was taken for simplicity as identical for E and I units. In Ahmadian et al. (2013) we consider aspects of the more general case in which external drives to E and I are not equal.

S1.3.2 Parameters: General considerations

We did not attempt to tune parameters to quantitatively match data, but instead aimed at explicating simple, robust mechanisms underlying qualitative behaviors. For similar reasons

we ignored many biological details that should be explored in future work, notably the different types of I cells and their (and E cells') different cellular and synaptic properties, cortical layers, biological properties such as spike-rate adaptation or synaptic depression that would reduce the supralinearity of input/output functions, and the dynamic increase in the power-law exponent n and associated change in the parameter k that would be induced by the reduction in voltage noise levels with contrast (Sadagopan and Ferster 2012) (because the effective power is roughly determined by the distance from rest to threshold in units of the voltage noise standard deviation (Hansel and van Vreeswijk 2002, Miller and Troyer 2002)). We used equal numbers of E and I units, but we expect no significant changes if reduced numbers of I units are used with correspondingly stronger connections, based on similar behavior of spiking models with realistic proportions of I neurons and rate models with equal numbers of E and I units (Murphy and Miller 2009, and D. Obeid and K.D. Miller, unpublished observations of SSN models).

Since this work was largely completed we realized (Ahmadian et al. 2013) that the most strongly nonlinear behavior would likely arise for $\Omega_E < 0$, $\Omega_E < \Omega_I$ where, for equal external input to E and I units as used here, $\Omega_E \equiv \bar{W}_{II} - \bar{W}_{EI}$, $\Omega_I \equiv \bar{W}_{IE} - \bar{W}_{EE}$, and $\bar{W}_{XY}$ is the total synaptic strength from units of type Y received by a unit of type X. This condition was not met in Fig. 6, which had $0 < \Omega_E < \Omega_I$. These simulations nonetheless worked well enough for our purposes of displaying qualitative behavior.

We used $\tau_I = \frac{1}{2}\tau_E$. Using faster inhibition than excitation helps ensure network stability but does not otherwise affect steady state responses.

In the 2D simulations (Figs. 6-8), degrees can be converted to distance across cortex by assuming a cortical magnification factor of 0.6 mm/deg, a typical figure for $5-10^o$ eccentricity in the cat (Albus 1975), giving $\sigma_{EE} = 1.02$mm, $\sigma_{IE} = 1.54$mm, $\sigma_{EI} = \sigma_{II} = 0.51$mm, orientation map period 1.2mm. We used slightly different exponents, $n_I > n_E$, to increase stability despite variability (experiments suggest much larger differences: Supplemental Fig. S3 of Haider et al. 2010). Variability of τ's, n's, k was limited because larger variability tended to yield instability. Biologically, large variability can probably be tolerated without instability because of various forms of homeostatic compensation (Turrigiano 2011, Vogels et al. 2011) as well as mechanisms such as adaptation/depression in excitatory cells and synapses or facilitation in inhibitory synapses, not modeled here.

S1.3.3 DoG and SSM fits to model data: General considerations

Model length-tuning curves have 61 data points (evenly spaced from 0.5 to 75 grid units). In Fig. 6I, mean/median SSE's per data point for position tuning are 1.4/1.8 (DOG) or 3.5/4.6 (SSM) times those of experiments; for length tuning, 0.09/0.08 (DOG) or 0.10/0.08 (SSM). These differences, of unknown cause, are similar for DOG and SSM and so do not indicate differences in periodicity of model vs. real cells.

S1.3.4 Determining size of stimuli used by Haider et al. (2010), relative to CRF size

In the Discussion we discuss the size of the stimuli used by Haider et al. (2010), based on the following calculation. We assume a Gaussian CRF profile (Jones and Palmer 1987), which we take for simplicity to be circularly symmetric. We define the standard deviation of the Gaussian to be length 1. Thus the CRF is proportional to $G(r) \equiv \frac{1}{2\pi} e^{-r^2/2}$ where r is the radial coordinate in 2D polar coordinates. In response to a stimulus of strength 1 uniformly stimulating the CRF out to radius x (measured in units of the standard deviation), the output of the CRF filter applied to the stimulus is $\int_0^x r dr \int_0^{2\pi} d\theta\, G(r) = 1 - e^{-x}$. We assume the CRF size is 2 standard deviations of the Gaussian, so maximal filter output is $1 - e^{-2}$ (*e.g.* beyond that radius surround suppression would set in). Finally we assume the neuron's response is the filter output raised to a power n. Thus, the condition that the stimulus radius x gives half-maximal response is $\left(\frac{1-e^{-x}}{1-e^{-2}}\right)^n = \frac{1}{2}$, or $x = -\ln\left(1 - 2^{-1/n}\left(1 - e^{-2}\right)\right)$. For n ranging from 2 to 3, this gives x ranging from 0.94 to 1.16 (in standard deviations), or from .47 to .58 of CRF size.

S1.4 Supplemental Methods Information: Experiments

S1.4.1 Recording

Spikes were amplified with a preamplifier/amplifier system by Multichannel Systems (Germany) and acquired and clustered using a Micro1401 acquisition board and Spike2 software (Cambridge Electronic Design, LLC). Visual stimuli were created in Matlab using the Psychophysics Toolbox (Kleiner et al. 2007) on a Macintosh Pro (OS10) and displayed on a Sony monitor (GDM-520) (100 Hz refresh and frame rates). Spike tuning curves were analyzed with custom software in Matlab.

S1.4.2 Maximum likelihood estimation (MLE) for denoising of tuning curves

To improve our estimates of tuning curves, which represent the stimulus-specific component of responses, we used MLE to remove the effects of slow, stimulus-independent variations in excitability (Supplemental Figs. S1A,B). This was particularly important for our data because we presented each stimulus only four or five times. Because we wished to explore a large region of stimulus parameter space with each cell, we were constrained in the number of times we could present each stimulus by the amount of time we could reasonably expect to record from a single neuron. Removing the slow stimulus-independent variations in rate improves our statistical power to estimate tuning curves. We also incorporated our prior knowledge that tuning curves are smooth by using constraints on tuning curve smoothness, which also improves our statistical power by effectively combining data across nearby stimuli.

To remove stimulus-nonspecific slow variations in response magnitude, we modeled a neuron's firing rate to stimulus type i (*i.e.*, a given stimulus size, stimulus position, or CM contrast and SF) presented at time t as $r_i(t) = g(t)s_i$ where $g(t)$ represents slow changes in

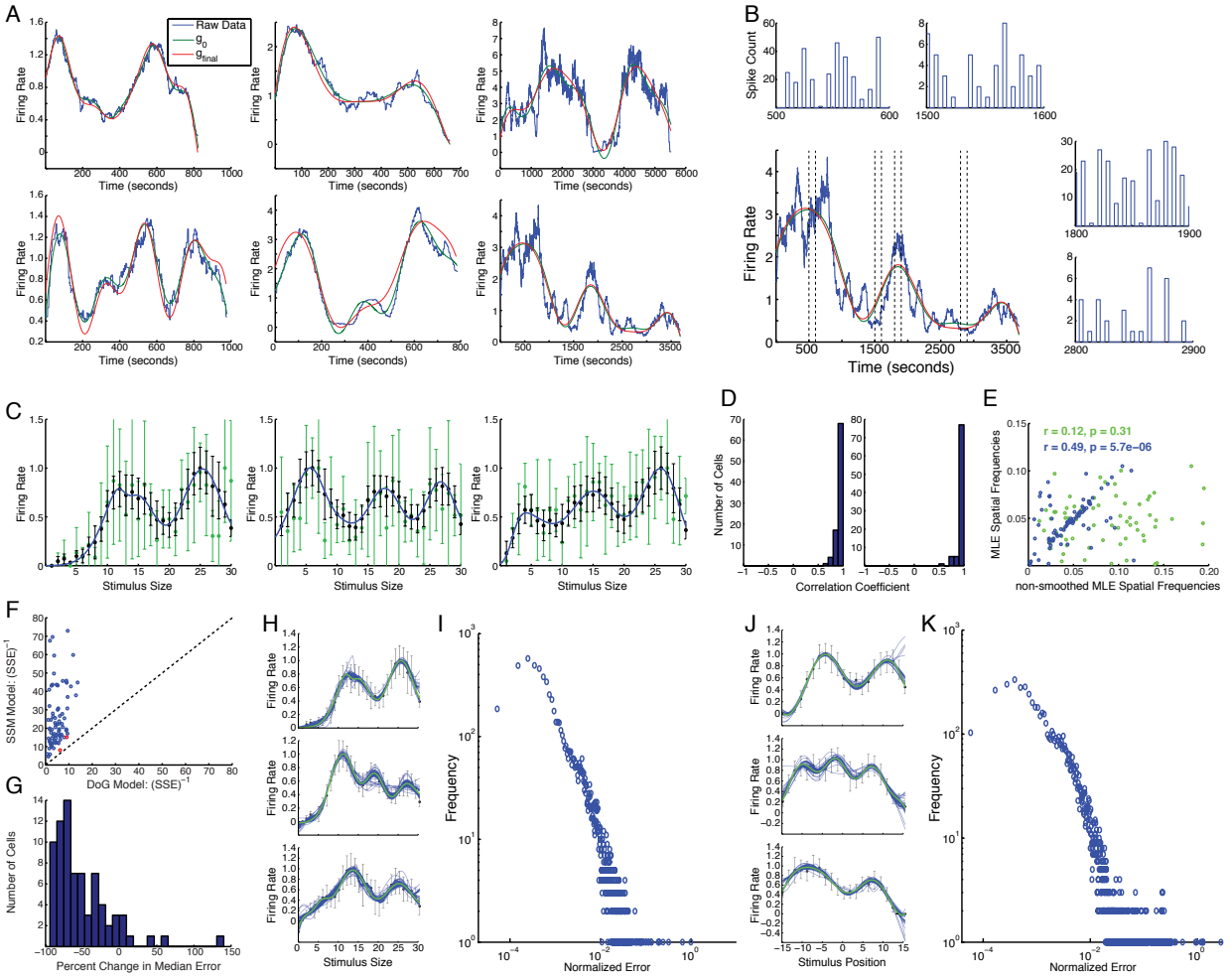

Figure S1:

MLE for denoising of tuning curves, and fits of DOG and SSM models to tuning curves (related to Supplement S1.4.2-S1.4.3). (A). Examples of slow changes in cortical excitability. The firing rate versus time for six example cells is shown in blue (calculated with a 100ms sliding window). The initial estimate of the nonspecific scaling function, $g_0(t)$, is in green. The adjusted $g(t)$ that maximizes the likelihood of both $g(t)$ and the stimulus specific response vector $s_i(t)$ is shown in red. **(B)**. Slow fluctuations in cortical excitability do not obscure stimulus selectivity. We examine one firing rate curve from **(A)** while highlighting four 100-second time epochs, marked by adjacent pairs of dashed vertical lines. Each subplot shows firing rates during one of these epochs, in bins across the 100 seconds, with each bin indicating response to a single stimulus or a single ISI (ISI responses are small or zero, so ISI bins mostly appear to be spaces between the bins showing stimulus responses). The stimuli were shown in pseudorandom order so the particular stimuli shown are different in each epoch. During periods of both high and low cortical excitability, the cell responds differentially to different stimuli. Note the changing scale on the y-axes of the subplots. **C.** Example outcomes of MLE denoising: three example size-tuning curves. The green data are the raw size-tuning curves, and the black data indicate the size-tuning responses after the MLE de-noising process. The best-fit SSM model curve for the post-processed data is in blue.
(Continued on next page.)

Figure S1:

(Continued). **D.** MLE denoising preserves response properties. Left: Histogram of the correlation coefficients between orientation tuning curves before and after the MLE denoising process. The overwhelming majority of cells show a near perfect correlation between the raw tuning curve and the post-processed tuning curve. Right: Histogram of the correlation coefficients of luminance spatial frequency tuning curves before and after the MLE denoising process. **E.** MLE smoothing eliminates high frequencies from SSM fits. We consider frequencies of the oscillation in fits of the SSM model to size-tuning curves (76 cells). The green dots show fits to the data from MLE denoising without smoothing (x-axis) and from MLE denoising with smoothing (y-axis). The two show no significant correlation ($r = 0.12$, $p = 0.31$; $DF = 74$, $t = 1.014$). We found the Gaussian spatial filter that, applied to the unsmoothed MLE size-tuning curves, gave the least mean-squared error from the smoothed MLE curves, which had standard deviation $\sigma = 0.99^{\circ}$. The blue dots compare frequencies from SSM fits to this Gaussian smoothing of the unsmoothed MLE curves (x-axis) to those from the smoothed MLE curves (y-axis); these are now highly correlated ($r = 0.49$, $p = 5.7 \times 10^{-6}$; $DF = 74$, $t = 4.891$). Thus the smoothing in the MLE algorithm has very similar effect to smoothing with a Gaussian filter with $\sigma = 0.99^{\circ}$. **F,G.** Statistics of size-tuning fits compared to the classic Difference of Gaussians (DoG) model. Same analysis as Fig. 4B-C, but here comparison is to a more classic version of the DoG model, setting parameter $a_7 = 0$ in the equation for the size-tuning DoG (Section S1.2.3). **F.** The reciprocal of the sum squared error for the DoG and SSM models, conventions and statistical tests as in Fig. 4B. 74/76 cells had significantly better fits by SSM than classic DoG by nested F-test. **G.** Results of cross-validation analysis, conventions as in Fig. 4C. For 69/76 cells the SSM model fit gave less median sum-squared error than the classic DoG model ($p = 6.4 \times 10^{-14}$, binomial test; median of distribution significantly different from zero, $p = 1.1 \times 10^{-11}$, Wilcoxon signed-rank test, SignedRank= 2775; statistical tests as in Fig. 4C). Statistics for all cells given in Supplemental Table S2. **H-I.** Cross-validation analysis of size-tuning model fits. **H.** Three examples of the cross-validation process. In each case, the original SSM curve, fit with all 30 data points, is in green. The 100 cross-validation fits, each fit with 24 randomly selected points (80% of the original data), are shown in blue. **I.** A log-log histogram of the normalized error of the cross-validation fits relative to the full-data fit shows a roughly power-law distribution, indicating that most cross-validation fits differ very little from their respective full-data fit. Letting r_i^a and r_i be the firing rate at position i for cross-validation estimate a and for the full-data fit respectively, the normalized error for estimate a is $\frac{\sum_i (r_i^a - r_i)^2}{\sum_j r_j^2}$. **J-K.** Cross-validation analysis of position-tuning model fits. **J.** Three examples of the cross-validation process. Conventions as in **H**. **K.** A log-log histogram of the normalized error between the cross-validation fits and the full-data fit. Conventions as in **I**.

overall cortical excitatability and s_i is stimulus-specific response (the tuning curve). Time was binned, one bin for each stimulus onset/offset interval and one for each ISI (ISI's are an additional stimulus type). The initial $g(t)$ was found by least-squares fitting of the spike train, smoothed with a 100ms sliding window, to the 12-parameter function, $g(t) = \sum_{i=1}^{4} A_i \sin(2\pi f_i t + \phi_i)$ where the f_i were constrained to be < 10 cycles/experiment duration (exp't duration typically 8-16 minutes) to ensure that $g(t)$ captures only slow variations corresponding to changes in cortical state rather than changes in stimuli. We then maximized the log likelihood, alternating maximizing over the s_i with $g(t)$ fixed and over the 4 A_i parameters of $g(t)$ with other parameters of $g(t)$ and the s_i fixed. To incorporate prior knowledge of the smoothness of tuning curves, for length- and position-tuning curves, the s_i maximization was constrained so that, after setting maximum s_i to 1, the second derivative of the tuning curve was always $< 0.10/\text{deg}^2$ (length-tuning) or $< 0.15/\text{deg}^2$ (position tuning). Smoothing was not used for CM-tuning because those curves had only six points, sufficiently spaced that we had no a priori reason to expect smooth curves. For length and position tuning, the likelihood of an observed k spikes in a given time bin of size Δt at time t with stimulus i was given by a Poisson distribution with mean $r_i(t)\Delta t$. For CM tuning, the log likelihood of an observed envelope F1 amplitude k in a given bin was $-(k - r_i(t)\Delta t)^2$.

To find error bounds for our estimates, we derive the Hessian matrix of the log likelihood – the matrix of second derivatives of the log likelihood (L.L.) with respect to the s_i's. The Hessian is diagonal – derivatives $\frac{\partial^2 \text{L.L.}}{\partial s_i \partial s_j}$ are zero for $i \neq j$ – and the diagonal entries are just $\frac{\partial^2 \text{L.L.}}{\partial s_i^2}$. In this case, in the neighborhood of the maximum likelihood estimate, the probability of s_i can be approximated by a Gaussian, centered at the maximum likelihood value, with variance given by the negative of the inverse of the i^{th} diagonal entry of the Hessian. We take the error bar to be the standard deviation of this distribution, *i.e.* the square root of the variance, which we refer to as the standard error (because it gives the standard deviation of the probability distribution for the mean).

The responses and error bars presented throughout the experimental results section are derived from this MLE process. Note that tuning curve amplitudes are arbitrary (replacing $g(t)$ and the s_i with $bg(t)$ and $(1/b)s_i$ would not change performance for any b), so presented tuning curves are all normalized to have peak value 1.

As controls on the MLE process, we show that (1) responses remain stimulus-selective across widely varying overall levels of cortical responsiveness (Supplemental Fig. S1B); (2) orientation tuning curves and spatial frequency tuning curves are largely unchanged by the MLE, (Supplemental Fig. S1D; the MLE process was applied to the stimulus epochs in which preferred direction and preferred spatial frequency were assessed).

We also examined the effects of the MLE fitting on the frequencies of tuning curve oscillations found by the SSM model fits to size tuning curves. The MLE procedure suppresses higher frequencies of oscillation (above about 0.1 cycle/deg) and shrinks error estimates (Supplemental Fig. S1C,E); position-tuning curves behave similarly). We believe this is due to suppression of high-frequency noise in the tuning curves. This noise arises because the random presentation times of a given stimulus may happen to occur at times of lesser excitability or of greater excitability. Since stimuli of different sizes are presented in pseu-

dorandom order, these effects are uncorrelated between different stimulus sizes, including adjacent sizes, and so induce high-frequency noise in the size tuning curve. This noise is suppressed by the use of MLE to factor out the excitability changes. High-frequency noise also arises due to trial-to-trial biological variation in responses at a fixed level of excitability. This noise, and also residual noise from excitability changes, is suppressed by the assumption of smoothness of the tuning curves we used as part of the MLE procedure.

One might worry that the MLE smoothing procedure reduced signal rather than noise. To address this, we show that the smoothing is roughly equivalent to a very limited conventional smoothing. We ran the MLE process without any smoothing constraints ("MLE-unsmoothed"). We then found the Gaussian smoothing filter that, when applied to the size-tuning curves from MLE-unsmoothed, gave the least mean-squared difference across the 76 cells with the size-tuning curves resulting from MLE with smoothing ("MLE-smoothed"). The optimal Gaussian filter had standard deviation 0.99°. The smoothness assumption in MLE gives results very much like smoothing the MLE-unsmoothed tuning curves with this optimal filter. For each cell, we calculated the sum-squared difference between the size tuning curves determined by MLE-smoothed and by this Gaussian-filtering of MLE-unsmoothed, as a percentage of the sum of the squares of the MLE-smoothed tuning curve. This percentage had median 0.0130 (5th and 95th percentiles, 0.0028 and 0.040) and mean±stdev 0.0160±0.0139. Furthermore, the frequencies of SSM fits to MLE-unsmoothed data after (but not before) the Gaussian smoothing are highly correlated to the frequencies found from MLE-smoothed results (Supplemental Fig. S1E). All of these results indicate that adding the smoothness constraint to the MLE yields tuning curves very much like those obtained simply by smoothing MLE-unsmoothed with the Gaussian filter (a conclusion also supported by visual inspection of the curves). The Gaussian filter has a width about 1° and hence represents a very limited degree of smoothing. In addition, if the suppression of frequencies above 0.1 cycle/deg were due to the smoothness constraint eliminating true signal at higher spatial frequencies, we would expect – unless cells had two distinct oscillation frequencies, one above and one below 0.1 cycle/deg – that cells with oscillation frequencies above 0.1 cycle/deg in SSM fits to the MLE-unsmoothed size-tuning data would be brought down only to 0.1 cycle/deg in MLE-smoothed data (*i.e.*, to the highest limiting frequency imposed by smoothing, as judged by the highest frequency seen in the smoothed fits), but this is not the case (Supplemental Fig. S1E).

S1.4.3 Fits of DoG and SSM models to tuning curves

For size tuning, the exponential decay $e^{a_7 x}$ was important for a good fit. We included this term in both DoG and SSM models, so that the only difference between the two models is the periodicity. Results are very similar if the SSM model is compared to a more standard DoG model without the decay term ($a_7 = 0$ in equation for DoG model; Supplemental Fig. S1F).

Fits of SSM and DOG models using Matlab function lsqcurvefit were done subject to constraints established empirically as necessary to avoid poorly-fitting local minima. In units in which the first and last points on the curves had coordinates 10 and 300, respectively, these constraints were: for size-tuning curves, $a_1 \geq 0$, $0 \leq a_3 \leq 1$, $a_4 \geq 0$, $0 \leq a_6 \leq 1$ (SSM)

or $0 \leq a_6 \leq a_3$ (DOG), $-0.1 \leq a_7 \leq 0.1$, $0 \leq a_9 \leq \pi/10$, $-\pi \leq a_{10} \leq \pi$; for position-tuning curves, $a_1 \geq 0$, $-150 \leq a_2 \leq 150$, $a_3 \geq 0$ (DOG) or $a_3 \geq 25$ (SSM), $-150 \leq a_5 \leq 150$ (DOG only), $a_6 \geq 0$ (DOG) or $a_6 \geq 50$ (SSM), $0 \leq a_8 \leq 2\pi/45$, $-\pi \leq a_9 \leq \pi$, $a_{10} \geq 0$. In size-tuning DOG model of Supplemental Fig. S1F-G ($a_7 = 0$), constraints on other parameters are unchanged except $0 \leq a_3 \leq 0.2$. The use of different constraints for the two models may cast doubt on the use of the F-test, which depends on the models being nested, *i.e.* identical after extra parameters in the SSM model are set to zero. Because fits generally became worse (greater summed-squared error) when constraints were relaxed, we think of these constraints as guidance to the error-minimizing algorithm to get it into the best parameter regime, rather than as constraints on the models. The cross-validation analyses provide an independent check on the significance of our results that does not rely on the assumption of nested models.

In Figs. 4C, 4F and Supplemental Fig. S1G, we showed results of a cross-validation analysis comparing the performance of the DoG vs. SSM models. In Supplemental Figs. S1H-I (size-tuning data) and S1J-K (positional-tuning data), we show that there is in general very little difference between the cross-validation fits of the SSM model, using 80% of the data, and the SSM fits using the full data set, indicating that the variance in our SSM estimates is very small.

S1.5 Statistical Methods

S1.5.1 Assumptions of Normality

Most of the statistical tests we used make no assumption that data is normally distributed. There are two exceptions:

- We used a nested F-test to compare SSM and DOG model fits to data. These models are nested: the SSM model contains all the parameters of the DOG model plus additional parameters; setting these additional parameters to zero gives the DOG model. On the assumption that the residuals from the fits are approximately normally distributed, and under the null hypothesis that the simpler hypothesis is correct (*i.e.*, that the extra parameters in the more complex model are all equal to zero), the F-statistic, which is derived from the ratio of the summed-squared errors of the two fits (or more generally of the Ξ^2 of the two fits) should follow an F distribution with degrees of freedom as specified in legend of Supplemental Table S1. We use this test on the plausible assumption of approximately normally distributed residuals, but we also assay the same question with a cross-validation test that requires no such assumption.

- We used the Pearson correlation coefficient to determine whether two sets of data are correlated in Fig. 6K and Supplemental Figs. S9C,D,E and S1e. We use the standard test as to whether r is significantly different from zero, which is to conduct a Student's t-test with degrees of freedom $DF = n - 2$ on the statistic $t = r\sqrt{\frac{n-2}{1-r^2}}$. For an uncorrelated normal distribution, t follows the Student's t distribution with DF degrees of freedom. However, t also approximately follows this distribution for non-normal

distributions if sample size is not very small (Edgell and Noon 1984), *i.e.* ≥ 6, so no assumption of normality is required. Furthermore all but one of our tests show lack of significant correlation by a wide margin, with the two smallest non-significant p-values being 0.17 and 0.31, and the remaining test shows very strong significance ($p = 5.7 \times 10^{-6}$, one of the tests in Supplemental Fig. S1E). These margins combined with the results of Edgell and Noon (1984) alleviate any worries about non-normality.

S1.5.2 Test statistics for statistical tests of Figs. 4C,F, 5F and 7A,E

Here we give test statistics (and repeat p and r values from main text) for statistical tests other than those documented in Supplemental Tables.

- Tests of Fig. 4C,F: tests whether median of difference between sum-squared error of SSM and DOG models on withheld data in cross-validation tests is less than 0, using Wilcoxon signed rank test. Fig. 4C: $p = 1.04 \times 10^{-10}$, SignedRank= 2711; Fig. 4F: $p = 2.4 \times 10^{-7}$, SignedRank= 2347.

- Tests of Fig. 5F for differences between contrast levels in experimentally measured CM preferred SF, using Wilcoxon rank sum (WRS) test. Two middle contrasts not significantly different: $p = 0.68$, ranksum= 2584; low vs. medium: $p < 0.5 \times 10^{-4}$, ranksum= 2818; low vs. high: $p < 10^{-7}$, ranksum= 1789.5; middle vs. high: $p = 0.046$, ranksum= 7137.5.

- Tests of Fig. 7A, Student's t-test for significance of Pearson correlation coefficient (as described in previous subsection) between luminance and CM preferred orientations in model data: E units: $r = 0.098$, $p = 0.33$, $DF = 98$, $t = 0.979$; I units: $r = 0.093$, $p = 0.36$, $DF = 98$, $t = 0.923$.

- Tests of Fig. 7E for differences between high and low contrasts in model circular variance of orientation tuning of surround suppression, using WRS test. All units: $p = 2.6 \times 10^{-9}$, ranksum= 7032; E units: $p = 6.3 \times 10^{-10}$, ranksum= 1555; I units: $p = 0.034$, ranksum= 1990.

S2 Supplemental Text: Mathematical Analysis and Related Theoretical Issues

S2.1 Network Resonant Frequencies

We write the linear model equation in matrix/vector form as

$$\tau_E \mathbf{T} \frac{d}{dt}\mathbf{r}(x) = -\mathbf{r}(x) + \mathbf{W} * \mathbf{r}(x) + c\mathbf{h}(x) \tag{S1}$$

Here, $\mathbf{r}(x) = \begin{pmatrix} r_{\mathrm{E}}(x) \\ r_{\mathrm{I}}(x) \end{pmatrix}$, $\mathbf{h}(x) = \begin{pmatrix} h(x) \\ h(x) \end{pmatrix}$, $\mathbf{W}(x) = \begin{pmatrix} W_{\mathrm{EE}}(x) & -W_{\mathrm{EI}}(x) \\ W_{\mathrm{IE}}(x) & -W_{\mathrm{II}}(x) \end{pmatrix}$, $\mathbf{T} = \begin{pmatrix} 1 & 0 \\ 0 & \frac{\tau_I}{\tau_E} \end{pmatrix}$, and the $*$ means convolution: $\mathbf{W} * \mathbf{r}(x) \equiv \sum_{x'} \mathbf{W}(x - x')\mathbf{r}(x')$. We will also refer to the full set of connections as the matrix $\mathbf{W} = \begin{pmatrix} \mathbf{W}_{\mathrm{EE}} & -\mathbf{W}_{\mathrm{EI}} \\ \mathbf{W}_{\mathrm{IE}} & -\mathbf{W}_{\mathrm{II}} \end{pmatrix}$ where the submatrix $\mathbf{W}_{\mathrm{XY}}$ has elements $(\mathbf{W}_{\mathrm{XY}})_{\mathrm{ij}} = W_{\mathrm{XY}}(x_i - x_j)$ and x_i and x_j are the i^{th} and j^{th} grid positions respectively.

Here we analyze linear network behavior, and in particular derive expressions for the excitatory and inhibitory resonant frequencies. We simplify by assuming either periodic boundary conditions for the network or that the network stretches to $\pm\infty$. For generality we will let the inputs to E and I have different magnitudes: $h_{\mathrm{E}}(x) = \alpha h(x)$, $h_{\mathrm{I}}(x) = h(x)$.

Because the connections between two units at locations x and x' depend only on the distance between the two neurons – that is, they are translation-invariant, the same at any position – the convolution in Eq. S1 is turned into a multiplication by Fourier transformation. For any function $f(x)$, we let $\tilde{f}(k)$ be its Fourier transform at what we will call spatial frequency k (on a grid of N units, k is an integer corresponding to spatial frequency k cycles per N units). We normalize the Fourier transform so that the Fourier transform of $f * g(x)$ is $\tilde{f}(k)\tilde{g}(k)$.[1] Then after Fourier transform, Eq. S1 becomes

$$\tau_E \mathbf{T} \frac{d}{dt}\tilde{\mathbf{r}}(k) = -\tilde{\mathbf{r}}(k) + \tilde{\mathbf{W}}(k)\tilde{\mathbf{r}}(k) + c\tilde{\mathbf{h}}(k) \tag{S2}$$

where $\tilde{\mathbf{r}}(k) = \begin{pmatrix} \tilde{r}_{\mathrm{E}}(k) \\ \tilde{r}_{\mathrm{I}}(k) \end{pmatrix}$, $\tilde{\mathbf{h}}(k) = \tilde{h}(k) \begin{pmatrix} \alpha \\ 1 \end{pmatrix}$, and $\tilde{\mathbf{W}} = \begin{pmatrix} \tilde{W}_{\mathrm{EE}}(k) & -\tilde{W}_{\mathrm{EI}}(k) \\ \tilde{W}_{\mathrm{IE}}(k) & -\tilde{W}_{\mathrm{II}}(k) \end{pmatrix}$. Note that the E and I activity patterns at a given spatial frequency influence one another's time evolution, but evolve independently of the activity patterns at every other spatial frequency. This follows from the linearity of the network and the translation-invariance of the weight functions.

From Eq. S2, the network fixed point, where $\frac{d}{dt}\tilde{\mathbf{r}} = 0$, satisfies $\tilde{\mathbf{r}} = (\mathbf{1} - \tilde{\mathbf{W}}(k))^{-1} c\tilde{\mathbf{h}}(k)$,

[1] See footnote 3.

where $\mathbf{1}$ is the 2-dimensional identity matrix. We can rewrite this as

$$\tilde{r}_{\mathrm{E}}(k) = \left(\frac{\left(1 + \tilde{W}_{\mathrm{II}}(k)\right)\alpha - \tilde{W}_{\mathrm{EI}}(k)}{\mathrm{Det}\left(\mathbf{1} - \tilde{\mathbf{W}}(k)\right)} \right) \tilde{h}(k) \equiv \mathcal{L}_{\mathrm{E}}(k)\tilde{h}(k) \tag{S3}$$

$$\tilde{r}_{\mathrm{I}}(k) = \left(\frac{1 - \tilde{W}_{\mathrm{EE}}(k) + \alpha\tilde{W}_{\mathrm{IE}}(k)}{\mathrm{Det}\left(\mathbf{1} - \tilde{\mathbf{W}}(k)\right)} \right) \tilde{h}(k) \equiv \mathcal{L}_{\mathrm{I}}(k)\tilde{h}(k) \tag{S4}$$

Here, $\mathrm{Det}\left(\mathbf{1} - \tilde{\mathbf{W}}(k)\right) = \tilde{W}_{\mathrm{EI}}(k)\tilde{W}_{\mathrm{IE}}(k) - (\tilde{W}_{\mathrm{II}}(k) + 1)(\tilde{W}_{\mathrm{EE}}(k) - 1)$ is the determinant of $(\mathbf{1} - \tilde{\mathbf{W}}(k))$. Stability of the network dynamics requires that $\mathrm{Det}\left(\mathbf{1} - \tilde{\mathbf{W}}(k)\right) > 0$ for all k.[2]

Equations S3-S4 show how selective amplification of spatially periodic patterns of activity arise in response to non-periodic input. The terms multiplying $\tilde{h}(k)$, which we have given the names $\mathcal{L}_{\mathrm{E}}(k)$ and $\mathcal{L}_{\mathrm{I}}(k)$, act as linear filters on the input to produce the steady-state responses. If the input is not spatially periodic, *i.e.* has no peaks at $k \neq 0$ (non-DC peaks), spatial periodicity can nonetheless arise in the firing rates if the filters have non-DC peaks within the bandwidth of $\tilde{h}(k)$, inducing nearby non-DC peaks in $r_{\mathrm{E}}(k)$ or $r_{\mathrm{I}}(k)$. By solving for these filter maxima we can find the conditions under which the network will demonstrate spatial periodicity for non-periodic input.

To find the filter maxima, we will solve for the roots of the first derivative of the network filters with respect to k. The denominator of these derivatives is $\mathrm{Det}(\mathbf{1} - \mathbf{W}(k))^2$. Since network stability requires that $\mathrm{Det}(\mathbf{1} - \mathbf{W}(k)) > 0$ for all k, this denominator remains nonzero. Thus, we can simply determine when the numerator of the derivative becomes zero.

S2.1.1 Inhibitory resonant frequency

Defining $\partial_k f(k) \equiv \frac{df(k)}{dk}$, the numerator of $\partial_k \mathcal{L}_{\mathrm{I}}(k)$ is

$$\begin{aligned} &\left(\tilde{W}_{\mathrm{EI}}(k) - \alpha\left(1 + \tilde{W}_{\mathrm{II}}(k)\right)\right)\left(\partial_k\tilde{W}_{\mathrm{IE}}(k)\left(\tilde{W}_{\mathrm{EE}}(k) - 1\right) - \partial_k\tilde{W}_{\mathrm{EE}}(k)\tilde{W}_{\mathrm{IE}}(k)\right) \\ &+ \left(1 - \tilde{W}_{\mathrm{EE}}(k) + \alpha\tilde{W}_{\mathrm{IE}}(k)\right)\left(-\partial_k\tilde{W}_{\mathrm{EI}}(k)\tilde{W}_{\mathrm{IE}}(k) + \partial_k\tilde{W}_{\mathrm{II}}(k)\left(\tilde{W}_{\mathrm{EE}}(k) - 1\right)\right) \end{aligned} \tag{S5}$$

We work in the limit in which inhibitory connectivity is very localized compared to excitatory connectivity, meaning that $\tilde{W}_{\mathrm{EI}}(k)$ and $\tilde{W}_{\mathrm{II}}(k)$ are very broad in k relative to $\tilde{W}_{\mathrm{IE}}(k)$ and $\tilde{W}_{\mathrm{EE}}(k)$. As a result, the derivatives of the two I projections are very small relative to the derivatives of the two E projections, so that the second line in Eq. S5 is very small relative to the first line. We restrict to the limit of completely localized inhibitory connectivity, as in our simulations, in which $\tilde{W}_{\mathrm{EI}}(k) \equiv \tilde{W}_{\mathrm{EI}}$ and $\tilde{W}_{\mathrm{II}}(k) \equiv \tilde{W}_{\mathrm{II}}$ are constants, independent

[2]The network is stable iff both eigenvalues of $\mathbf{1} - \tilde{\mathbf{W}}(k)$ have negative real part for all k (these eigenvalues across all k are the eigenvalues of $\mathbf{1}_{D_{\mathbf{W}}} - \mathbf{W}$, where $\mathbf{1}_{D_{\mathbf{W}}}$ represents the identity matrix of the same dimensionality as $\mathbf{W}$). The eigenvalues of a 2×2 matrix $\mathbf{M}$ have negative real part iff $\mathrm{Det}\,\mathbf{M} > 0$ and $\mathrm{Tr}\,\mathbf{M} < 0$, where $\mathrm{Tr}\,\mathbf{M}$ is the trace of $\mathbf{M}$, hence a necessary condition for stability is that $\mathrm{Det}\left(\mathbf{1} - \tilde{\mathbf{W}}(k)\right) > 0$ for all k.

of k, and so their derivatives are zero; one could consider corrections for finite width of the inhibitory projections, but we do not pursue that here.

Then, the condition for a zero of the derivative is that the first line of Eq. S5 is zero. Because $W_{\mathrm{EE}}(x)$ and $W_{\mathrm{IE}}(x)$ are even functions of x, both $\tilde{W}_{\mathrm{EE}}(k)$ and $\tilde{W}_{\mathrm{IE}}(k)$ are even functions of k, so both their derivatives are zero at $k = 0$. Thus, one zero is at $k = 0$. Assuming that it is not the case that $\tilde{W}_{\mathrm{EI}} = \alpha\left(1 + \tilde{W}_{\mathrm{II}}\right)$ – a condition that, if true, would mean that $r_{\mathrm{E}}(x) \equiv 0$ for all x by Eq. S3 – the only other zeros occur for k such that

$$\tilde{W}_{\mathrm{EE}}(k) = \frac{\partial_k \tilde{W}_{\mathrm{EE}}(k)\tilde{W}_{\mathrm{IE}}(k)}{\partial_k \tilde{W}_{\mathrm{IE}}(k)} + 1 \tag{S6}$$

The first term on the right side of Eq. S6 will be positive for all k if $\partial_k \tilde{W}_{\mathrm{EE}}(k)$ and $\partial_k \tilde{W}_{\mathrm{IE}}(k)$ always have the same sign and $\tilde{W}_{\mathrm{IE}}(k) > 0$ for all k. This will be true for Gaussian connectivity functions on an infinite continuum, and should be true more generally for even connectivity functions that decay monotonically with distance sufficiently smoothly. So long as this is true, a solution of equation S6, meaning a non-zero peak for the network filter, can only occur for k with $\tilde{W}_{\mathrm{EE}}(k) > 1$, which – along with overall network stability – is the condition for the network to be an ISN. That is, given localized inhibitory projections and sufficiently smoothly decaying excitatory projections, a necessary – but not sufficient – condition for the network to show spatially periodic responses to spatially non-periodic inputs is that the network be an ISN.

We now use our choice of Gaussian excitatory connectivity functions, $\mathbf{W}_{aE}(x) = J_{aE} e^{-\frac{x^2}{2\sigma_{aE}^2}}$, and assume we are operating on an infinite continuum rather than a discrete finite grid – a continuum of units along an infinite, continuous position x and hence an infinite continuum of spatial frequencies k. Note that this means that $\mathbf{W}_{aE}(x)$ has dimensions of 1/length (so that its spatial integral with rates gives a rate); in practice, this means we must replace the J_{aE}'s from our discrete connectivity on a grid of width Δx, with $J_{aE}/\Delta x$ (so that the discrete convolution $\sum_x' \Delta x \frac{J_{aE}}{\Delta x} e^{-\frac{(x-x')^2}{2\sigma_{aE}^2}} r_E(x')$ approaches an integral in the continuum limit). The J_{aE}'s in the formulae below should all be understood numerically to correspond to this $J_{aE}/\Delta x$ and have corresponding dimension 1/length. The I connections W_{aI} apply only to the same grid location, and the continuum equivalent is that the weights are $W_{aI}\delta(x-x')$ (so that continuum and discrete operations give the same result: $\int dx' W_{aI}\delta(x-x')r_I(x') = W_{aI}r_I(x)$). This means that the Fourier transform is simply $\tilde{W}_{aI} = W_{aI}$, which is dimensionless.

The continuum limit allows us to compute the Fourier transform of the Gaussian connectivity[3], which produces analytic results that agree very well with the simulated results

[3]We use the convention $\tilde{f}(k) = \int dx\, e^{ikx} f(x)$, $f(x) = \frac{1}{2\pi}\int dk\, e^{-ikx}\tilde{f}(k)$. With this convention, the Fourier transform of $f * g(x)$ is $\tilde{f}(k)\tilde{g}(k)$ (see text that calls footnote 1) and the Fourier transform of the weights on the continuum is $\tilde{W}_{aE}(k) = J_{aE}\sigma_{aE}\sqrt{2\pi}e^{-\frac{k^2\sigma_{aE}^2}{2}}$. If instead we use $\tilde{f}(k) = \frac{1}{\kappa}\int dx\, e^{ikx} f(x)$, $f(x) = \frac{\kappa}{2\pi}\int dk\, e^{-ikx}\tilde{f}(k)$ for some constant κ (*e.g.*, $\kappa = \sqrt{2\pi}$ is commonly used), then the convolution is multiplied by κ while the Fourier transform of the Gaussian is divided by κ. The result is that all the factors $\tilde{W}_{XY}$ in Eqs. S3-S4 are both divided by κ and multiplied by κ (the latter because they all result from convolutions), so that their values and hence the results of the analysis are unchanged.

on the finite grid (*e.g.*, see Fig. 5B-C of the main text and Supplemental Fig. S2A,B). We thus determine the k that solves Eq. S6, which we call the resonant frequency of inhibition, k_I:

$$k_I = \frac{\sqrt{2\ln\left(J_{EE}\sigma_{EE}\sqrt{2\pi}\left(1-\frac{\sigma_{EE}^2}{\sigma_{IE}^2}\right)\right)}}{\sigma_{EE}} \tag{S7}$$

Spatial periodicity arises iff (if and only if) the solution k_I is real, which in turn occurs iff the argument of the logarithm is greater than 1:

$$J_{EE}\sigma_{EE}\sqrt{2\pi}\left(1-\frac{\sigma_{EE}^2}{\sigma_{IE}^2}\right) > 1 \tag{S8}$$

This in turn implies that $\sigma_{IE} > \sigma_{EE}$ and that $J_{EE}\sigma_{EE}\sqrt{2\pi} > 1$. $J_{EE}\sigma_{EE}\sqrt{2\pi} = \tilde{W}_{\mathrm{EE}}(0)$ is the maximum eigenvalue of the operation of convolving with $W_{\mathrm{EE}}(x)$ (see footnote 3), so that the latter condition means that the excitatory subnetwork by itself is unstable; that is, the network, assuming it is stable, is an ISN.

In sum, for a linear network, given sufficiently localized inhibitory connectivity and excitatory projections that are even and monotonically decay from zero sufficiently smoothly, then spatial periodicity in the inhibitory network in response to non-periodic input can only arise if (1) the network is an ISN and (2) $\sigma_{IE} > \sigma_{EE}$. The periodicity then will arise precisely when the condition in Eq. S8 is satisfied.

In addition, note that, in Eq. S7, the dependence of k_I on the items inside the logarithm is weak, so that the strongest dependence of k_I is that it is proportional to $1/\sigma_{EE}$. That is, longer-range excitatory projections lead to longer inhibitory wavelengths. In addition, we see that k_I increases more weakly with increasing J_{EE} and with increasing σ_{IE}/σ_{EE}, meaning that excitatory projections that are stronger or more widespread to I vs. E lead to shorter inhibitory wavelengths.

S2.1.2 Excitatory resonant frequency

The numerator of $\partial_k \mathcal{L}_{\mathrm{E}}(k)$ is

$$\begin{aligned}&\left(\tilde{W}_{\mathrm{EI}}(k) - \alpha\left(1+\tilde{W}_{\mathrm{II}}(k)\right)\right)\left(\partial_k\tilde{W}_{\mathrm{IE}}(k)\tilde{W}_{\mathrm{EI}}(k) - \partial_k\tilde{W}_{\mathrm{EE}}(k)\left(1+\tilde{W}_{\mathrm{II}}(k)\right)\right)\\ &+\left(1-\tilde{W}_{\mathrm{EE}}(k)+\alpha\tilde{W}_{\mathrm{IE}}(k)\right)\left(\partial_k\tilde{W}_{\mathrm{II}}(k)\tilde{W}_{\mathrm{EI}}(k) - \partial_k\tilde{W}_{\mathrm{EI}}(k)\left(1+\tilde{W}_{\mathrm{II}}(k)\right)\right)\end{aligned} \tag{S9}$$

Again, we take $\tilde{W}_{\mathrm{EI}}(k) \equiv W_{\mathrm{EI}}$ and $\tilde{W}_{\mathrm{II}}(k) \equiv W_{\mathrm{II}}$ so that the second line is zero, and find, assuming that $W_{\mathrm{EI}} \neq \alpha\left(1+W_{\mathrm{II}}\right)$, that the zeros of $\partial_k\mathcal{L}_{\mathrm{E}}(k)$ are either at $k=0$ or where

$$W_{\mathrm{EI}} = \frac{\partial_k\tilde{W}_{\mathrm{EE}}(k)\left(1+W_{\mathrm{II}}\right)}{\partial_k\tilde{W}_{\mathrm{IE}}(k)} \tag{S10}$$

Using the Gaussian connectivity functions and the assumption of an infinite continuum, we find that the non-DC zeros of $\partial_k \mathcal{L}_{\mathrm{E}}(k)$ occur at the excitatory resonant frequency k_E:

$$k_E = \frac{\sqrt{\frac{2}{1-(\sigma_{EE}^2/\sigma_{IE}^2)} \ln\left(\frac{W_{EI} J_{IE} \sigma_{IE}^3}{J_{EE}(1+W_{II})\sigma_{EE}^3}\right)}}{\sigma_{IE}} \tag{S11}$$

For this to be real and nonzero, and thus for excitatory spatial periodicity to exist, we either must have $\sigma_{IE} > \sigma_{EE}$ and the argument of the logarithm > 1, or else $\sigma_{IE} < \sigma_{EE}$ and the argument of the logarithm < 1

Unlike inhibition, the existence of a real k_E does not require the network to operate within the ISN regime. However, we now show that, assuming a stable network, if k_I is real and positive, then k_E is also real and positive, and furthermore $k_I < k_E$. That is, if the inhibitory network shows spatial periodicity, the excitatory network does also, with a shorter wavelength. We use the facts, which follow from k_I being real and positive, that (1) $\sigma_{IE} > \sigma_{EE}$ and (2) Eq. S8 is satisfied.

Since $\sigma_{IE} > \sigma_{EE}$, k_E is real and positive iff the argument of the logarithm is > 1:

$$W_{EI} J_{IE} \sigma_{IE}^3 > J_{EE}\left(1 + W_{II}\right)\sigma_{EE}^3 \tag{S12}$$

As noted above, a necessary condition for network stability is that $\mathrm{Det}\left(\mathbf{1} - \tilde{\mathbf{W}}(k)\right) > 0$ for all k. By solving for the extrema of this determinant (the values of k for which its derivative with respect to k is 0) and imposing the condition that the determinant at these extrema is > 0, we obtain the following requirement for stability:

$$\left(\frac{W_{EI} J_{IE} \sigma_{IE}^3}{J_{EE}\left(1 + W_{II}\right)\sigma_{EE}^3}\right)^{\left(\frac{\sigma_{EE}^2}{\sigma_{IE}^2 - \sigma_{EE}^2}\right)} > J_{EE}\sigma_{EE}\sqrt{2\pi}\left(\frac{\sigma_{IE}^2 - \sigma_{EE}^2}{\sigma_{IE}^2}\right) \tag{S13}$$

From Eq. S8, the right side of Eq. S13 is > 1. Since $\sigma_{IE} > \sigma_{EE}$, the exponent on the left side of Eq. S13 is > 0. Thus, a necessary condition for stability is that $\left(\frac{W_{EI} J_{IE} \sigma_{IE}^3}{J_{EE}(1+W_{II})\sigma_{EE}^3}\right) > 1$, which also means that the extremum is in fact a minimum.[4] This is precisely the condition of Eq. S12 that guarantees that the argument of the logarithm in Eq. S11 for k_E is > 1 and thus that the excitatory population has a real resonant frequency. Furthermore, a bit of algebra shows that the condition $k_I < k_E$ then translates precisely into the condition of Eq. S13 (which also implies that stability is lost precisely when k_I becomes greater than k_E). In sum, if the network is stable and the inhibitory network has a real, positive resonant frequency, then the excitatory network has a higher real, positive resonant frequency.

S2.1.3 Understanding spatially periodic activity in the model from the resonant frequencies

From equations S11 and S7, we see that, with increases in $\frac{\sigma_{EI}}{\sigma_{EE}}$, k_I increases, while k_E may increase or decrease. We test our formulae (derived from the continuum limit) against the

[4] The 2nd derivative at the extremum is positive iff $\left(\frac{W_{EI} J_{IE} \sigma_{IE}^3}{J_{EE}(1+W_{II})\sigma_{EE}^3}\right) > 1$.

result of simulations of our linear model on the grid, varying σ_{IE} while keeping all other parameters constant at the values given previously, and compare the preferred contrast modulation (CM) spatial frequency to the analytically predicted resonant frequencies (Supplemental Fig. S2A,B, and see also Fig. 5B-C of main text). The match is essentially perfect. The analytic solutions reveal that for σ_{IE} sufficiently wide, the network will actually be unstable (red area on the plot). This arises when the E→I connections become too broad for feedback inhibition to stabilize higher frequencies at which E→E connections are unstable, and as already noted occurs precisely where the resonant frequency of inhibition becomes greater than that of excitation.

This analysis also reveals why stimuli with sharp-edged contrast profiles produce multi-peaked length-tuning curves but those with Gaussian contrast profiles do not (Supplemental Figs. S7,S8). In the Fourier domain, a step-function is transformed into a sinc function $\frac{\sin(kl)}{k}$, where l is the width of the step function, and more generally sharp-edged stimulus profiles will have varying degrees of "ringing" in their Fourier transforms. This ringing will induce sign changes in the Fourier representation whose positions depend on stimulus length, resulting in a periodic flip in the phase of the resonant frequency with increasing stimulus size. These phase changes give rise to the periodic rise and fall of activity of the unit at the stimulus center with stimulus length, *i.e.* to periodic length-tuning curves. Gaussian stimuli, on the other hand, are simply transformed into Gaussians curves over frequency with inversely proportional width (narrow stimuli will have broad Fourier representations, and vice-versa). For sufficiently wide Gaussian stimuli, the power spectrum goes essentially to zero at a frequency below that of the peaks in the network response filters (k_E and k_I). Then the network's resonant frequencies receive sufficiently little input that the power in the firing-rate curves follows the power in the stimulus, falling monotonically with frequency. As a consequence, the firing rates show no spatial periodicity. For narrower Gaussian inputs, the stimulus may be wide enough in Fourier space to have non-zero power at the network's preferred frequencies, and in response the network does have spatially-periodic activity – see the yellow curves in the left half of Supplemental Fig. S7A. However, this does not produce periodic length tuning curves because the phase does not change with increasing stimulus length (and also the spatial periodicity largely disappears at relatively small stimulus sizes).

As the length l of a step-function stimulus is increased, there can be stimulus lengths where $\frac{\sin(kl)}{k} = 0$ for one of the peak frequencies (k_E or k_I). This will be observed across the population as a relative weakening in the amplitude of the corresponding spatial oscillation (though not a complete absence of periodicity, as spatial frequencies near the peak are also relatively amplified).

S2.2 Critical frequency, and an experimental test

S2.2.1 The critical frequency

A focus of previous theoretical work on the ISN regime has been on the "paradoxical" decrease in steady-state inhibitory firing rates that results from an increase in the external input to inhibitory units (Ozeki et al. 2009, Tsodyks et al. 1997). With the addition of a

spatial dimension in our current model, this paradoxical response depends on the stimulus spatial frequency. This can be understood from the fixed-point firing-rate solutions in equations S3 and S4. The E and I activities at each frequency k satisfy equations of the same form as the linear two-population models (one E population, one I population) studied in (Ozeki et al. 2009, Tsodyks et al. 1997). Hence the analysis of those papers applies separately to the activity at each frequency. If $\tilde{W}_{\mathrm{EE}}(k) > 1$, then the excitatory subnetwork at frequency k is unstable, so that, assuming the dynamics at frequency k are stabilized by feedback inhibition, the activity at frequency k behaves as an ISN. This includes the paradoxical response to input to inhibitory units: if external input is purely to inhibitory cells, $\tilde{h}_{\mathrm{E}}(k) \equiv 0$ or $\alpha = 0$, the fixed-point equations become

$$\tilde{r}_{\mathrm{E}}(k) = -\frac{1}{\mathrm{Det}\left(\mathbf{1} - \tilde{\mathbf{W}}(k)\right)} \tilde{W}_{\mathrm{EI}}(k)\tilde{h}_{\mathrm{I}}(k) \tag{S14}$$

$$\tilde{r}_{\mathrm{I}}(k) = \frac{1}{\mathrm{Det}\left(\mathbf{1} - \tilde{\mathbf{W}}(k)\right)} \left(1 - \tilde{W}_{\mathrm{EE}}(k)\right) \tilde{h}_{\mathrm{I}}(k) \tag{S15}$$

Because the network is stable, $\det(1 - \mathbf{W}(k)) > 0$. Hence, as expected, $\tilde{r}_{\mathrm{E}}(k)$ is always decreased by an increase in input $\tilde{h}_{\mathrm{I}}(k)$ to the inhibitory units. However, $\tilde{r}_{\mathrm{I}}(k)$ is increased or decreased by such a change in input according to whether $\tilde{W}_{\mathrm{EE}}(k) < 1$ or $\tilde{W}_{\mathrm{EE}}(k) > 1$, respectively. The decrease in $\tilde{r}_{\mathrm{I}}(k)$ in response to increased input to inhibitory units for $\tilde{W}_{\mathrm{EE}}(k) > 1$ is the "paradoxical" ISN response.

Because the strength of connectivity $W_{\mathrm{EE}}(x)$ decreases monotonically and smoothly to zero as a function of distance $|x|$, in the Fourier domain the connection strength $\tilde{W}_{\mathrm{EE}}(k)$ also decreases monotonically as a function of spatial frequency $|k|$. Thus, if the network is an ISN, meaning that at least some values of $\tilde{W}_{\mathrm{EE}}(k)$ are > 1, then with increasing $|k|$ $\tilde{W}_{\mathrm{EE}}(k)$ will fall below 1 at some critical frequency $|k| = k_c$. This means that frequencies below k_c will show the paradoxical ISN behavior, while frequencies above k_c will not. The critical frequency k_c is defined by $J_{EE}\sigma_{EE}\sqrt{2\pi}e^{-\left(k_c\sigma_{EE}/\sqrt{2}\right)^2} = 1$, that is:

$$k_c = \frac{\sqrt{2\ln\left(J_{EE}\sigma_{EE}\sqrt{2\pi}\right)}}{\sigma_{EE}} \tag{S16}$$

k_c scales approximately as $\frac{1}{\sigma_{EE}}$, since the logarithmic dependence is weak. Note that if $J_{EE}\sigma_{EE}\sqrt{2\pi} < 1$, meaning that no frequency has $\tilde{W}_{\mathrm{EE}}(k) > 1$ (the network is always a non-ISN), then k_c is imaginary, meaning that there is no transition from ISN to non-ISN behavior at any real frequency.

We note from examining Eq. S7 that $k_I = \sqrt{k_c^2 + \frac{2}{\sigma_{EE}^2}\ln\left(1 - \frac{\sigma_{EE}^2}{\sigma_{IE}^2}\right)}$. Since the second term in the squareroot is negative, $k_I < k_c$. This shows again that the resonant frequency of the inhibitory elements must fall within the range of frequencies that are inhibition-stabilized.

S2.2.2 Experimental Prediction: Ideal Case.

The existence of this critical frequency yields an interesting experimental prediction, illustrated in Fig. 8 of the main text. Here and in the next section we provide the theory behind this prediction, based on the results just obtained in section S2.2.1.

We imagine we have experimentally isolated an ISN of E and I cells, for example a patch of sufficiently-stimulated layer 2/3 cells in a piece of cortex. There are many practical questions as to when an ISN has been isolated, for example: can a patch of upper layer cells be treated effectively as a closed network except for steady external input arising from other layers and other patches of cortex, *i.e.* can we neglect feedback from these other regions in response to changes in activity in the patch? What are the roles of multiple subtypes of inhibitory neurons, and which inhibitory neurons are the relevant ones for providing feedback inhibition to stabilize the otherwise unstable excitatory subnetwork? We ignore these questions, simply imagining that feedback from outside the patch is negligible, that the recurrence among the E cells in the patch is strong enough to be unstable by itself, and that we are manipulating I neurons in the patch that provide feedback inhibition that prevents this instability.

The prediction is based on selectively stimulating I cells in a manner that is sinusoidally modulated spatially across cortex. We assume this is achieved with light stimulation of channelrhodopsin (ChR) expressed only in the I cells. There must be a baseline level of stimulating light about which the sinusoidal modulation occurs. We assume the network is in the ISN regime in response to spatially unmodulated light stimulation (changes in the baseline light level). The sinusoidal modulation must drift or contrast modulate, with a temporal frequency low enough that the network has time to roughly equilibrate and so be in a near-steady-state at each moment in the cycle. We can then apply the steady-state picture of ISN and non-ISN behavior to each moment in the cycle. E- and I-cell firing rates will periodically modulate at the temporal frequency of the stimulus, and we consider the relative phases of their modulation.

Then the prediction is that, for light stimulus of increasing spatial frequencies, the responses of E and I cells undergo a roughly 180^o transition in their relative phases at the critical spatial frequency k_c (Eq. S16). We illustrate this prediction in our linear model, stimulating only the inhibitory cells in the network with a "photostimulus" with a defined spatial frequency (Supplemental Fig. S2C). Stimuli with spatial frequency below k_c drive activity that operates as an ISN, and so E and I firing rates are modulated in phase with each other and out of phase with the input (Supplemental Fig. S2C, bottom left). This is the spatial analogue of the paradoxical response described by Ozeki et al. (2009). Stimuli with spatial frequency above k_c evoke non-ISN activity, and so E and I move out of phase with each other, while I moves in phase with the input (Supplemental Fig. S2C, bottom right).

As shown in Fig. 8 of the main text, exactly the same effect holds in the more realistic, nonlinear, two-dimensional model with sparse random connectivity, with one significant change. Because of the expansive input-output nonlinearity, the paradoxical response depends not only on the I-cell network being driven at a spatial frequency below the critical frequency, but also on the combination of sensory and baseline input being sufficient to drive the network into the ISN regime.

S2.2.3 Experimental Prediction: More Realistic Case.

Even given the assumption that we have isolated a patch of cells that operates as an ISN, there are other practical problems with the proposed experiment. First, only a fraction of inhibitory neurons will be activated, *i.e.* ChR will be incompletely expressed. We assume, due to the high connection probabilities from I to E neurons in cortex (Fino and Yuste 2011, Packer and Yuste 2011), that this fraction suppresses firing across the entire E network. Thus, the resulting reduction in E→I input will be spread across all the I neurons, both those that were stimulated and those that were not. The reduction in network excitation to a stimulated I neuron may then be less than the input that was directly added to it by the stimulation, so that stimulated I neurons will respond in phase to the stimulus. Unstimulated I neurons will respond in phase with the E cells, at the opposite phase to the stimulus. Unfortunately, these behaviors also characterize the non-paradoxical response expected in a non-ISN, and so no change in this behavior will be seen as k_c is crossed. Second, there are multiple subtypes of inhibitory neuron, and in the case of parvalbumin-containing (PV) and somatostatin-containing (SOM) interneurons in rodents, the two types can show opposite responses to stimuli that suppress E cells (Adesnik et al. 2012) (further discussed in main text). The result may then depend on which class of inhibitory cells is studied, where "class" refers to both subtype and whether or not they express ChR.

These problems can be overcome and the paradoxical response and the jump in phase as k_c is crossed can be robustly studied by applying the prediction to the relative phases of the net inhibitory current and the net excitatory current received by E cells, rather than to the firing of E and I cells. Regardless of the details of varying firing across different classes of I cells, this net current received should follow the predicted ISN (low-frequency, sufficient contrast) and non-ISN (otherwise) phase relationships. To understand why, it is necessary to understand the mechanism of the paradoxical ISN effect (Ozeki et al. 2009).

Suppose that the network is at a steady state of firing rates in response to steady external inputs. The fact that recurrent excitation is strong enough to be unstable by itself means that, if E cells lower their firing rates from the previous steady-state levels, this causes withdrawal of *too much* recurrent E→E input – so much that, absent other changes, the E cell firing rates would fall still further rather than moving back to the fixed point (and similarly, if E cells raised their rates, this would cause recruitment of so much recurrent E→E input that, absent other changes, the E cell firing rates would rise still higher). In a stable network in which the external input has not changed, feedback inhibition dynamically responds to a transient decrease in E-cell firing and restores the network to the fixed point (the lowering of E firing rates causes a lowering of feedback inhibition that exceeds the loss of recurrent excitation, so E cells move back up to their fixed point levels, bringing inhibition along with them). However, when the lowering of E-cell firing is caused by an increase of external input to I cells, so that in the new steady state E-cell firing remains lower than previously, then in this new steady state the E-cells must be receiving less inhibition than previously, to compensate for the excessive loss of recurrent excitation. No matter what the detailed dynamics of the various I-cell populations may be, only such a net decrease of inhibition can stabilize the new lower firing rates given the excessive loss of recurrent excitation (they

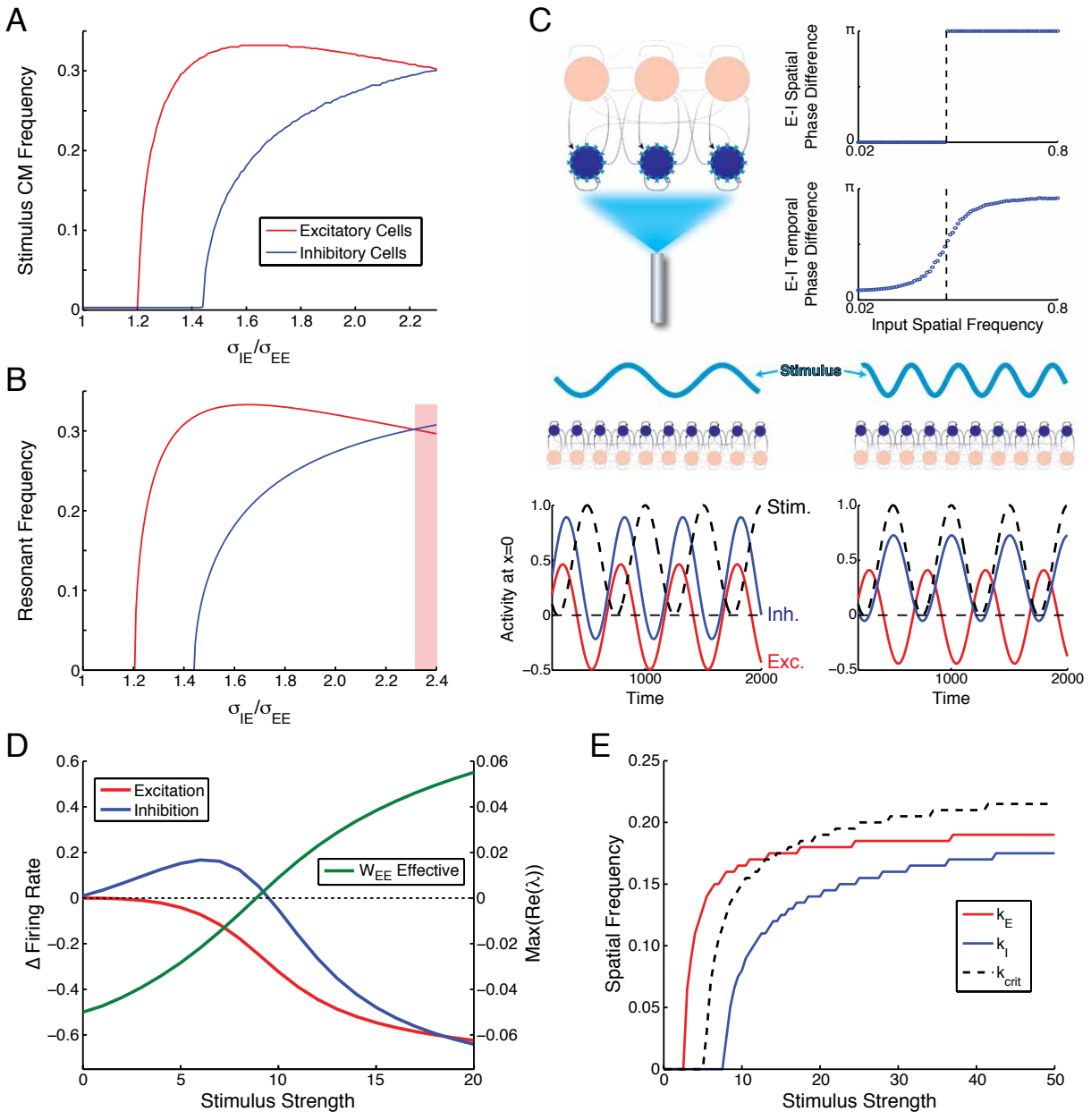

Figure S2:

Resonant frequencies and model linearization (related to Supplement S2.1-S2.3, and main text discussions of Figs. 3,5,8).

A-C: Resonant frequencies in the linear model of Fig. 2. **A,B**: Match of preferred contrast-modulation (CM) spatial frequencies (**A**) to analytically predicted resonant frequencies (**B**, computed from Eqs. S11 and S7), for E (red) and I (blue) units, vs. σ_{IE}/σ_{EE}. We vary σ_{IE} with all other parameters of the linear model fixed. In the red shaded region to the right in **(B)**, where $k_E < k_I$, the network is unstable. **C**: The ISN model predicts a 180° phase shift in the relative responses of E and I units to direct input to I cells at a critical input spatial frequency (as shown for nonlinear 2D model in Fig. 8). Top left: I cells in the network are stimulated with a photostimulus with a defined spatial frequency. The stimulus drifts at 2 Hz. Bottom: The low spatial frequency stimulus on the (continued on next page)

Figure S2:
(Continued) left has spatial frequency 0.2 cycles/degree. It drives E (red) and I (blue) cells at center of grid ($x = 0$) roughly in phase with one another, roughly out of phase with the stimulus they receive (black dashed). The higher spatial frequency stimulus on the right is at 0.5 cycles/degree. Now I cell fires roughly in phase with the stimulus and out of phase with E cell. Top right: summary plots of relative phases of E and I firing rates as a function of photostimulus spatial frequency. The vertical dashed lines are the analytically calculated critical frequency (Eq. S16). Top: phase difference between E and I activities across space at the spatial frequency of the stimulus. Bottom: phase differences in time between illustrated firing rates of E and I units at $x = 0$. **D-E**: Linearization of the nonlinear model of Fig. 3. **D**: Both E and I units are driven by a small (1^o diameter) stimulus of strength c (x-axis) centered at $x = 0$, and linearization is performed around the resulting steady state. Curves show the change in firing rates (left y-axis) of the E (red) and I (blue) units at $x = 0$ induced by giving additional input of strength 1 to stimulated I cells 1; and the maximum real part of the eigenvalues of $\hat{\mathbf{W}}_{\mathrm{EE}}$ (green, right axis). **E**: Resonant frequency increases with increasing stimulus strength. The resonant spatial frequencies of both the excitatory and inhibitory populations are calculated from the Jacobian matrix at the fixed point of response to a uniform stimulus of the given strength.

could also be stabilized if E-cells received a new source of external excitation sufficient to compensate the loss of recurrent excitation, but we have assumed that the only change to external inputs is in the input to I cells).

On the other hand, in the non-ISN regime, a drop in E firing from the old steady-state levels causes too little withdrawal of E→E input to allow the E firing rates to remain so low, so that these firing rates would bounce back up to the old steady-state levels absent other changes. The lower firing rates at the new steady state in the non-ISN regime must therefore be stabilized by an *increase* in the inhibition the E cells receive (or else by withdrawal of external excitatory input, which does not occur).

In sum, for stimuli below k_c (ISN regime), both the inhibition and the excitation received by E cells will decrease when the external input to I cells is increased, while for stimuli above k_c (non-ISN regime), the inhibition they receive will increase while the excitation they receive will decrease. Thus, for low-temporal-frequency stimuli to I cells, the relative phase of the inhibition and the excitation received by E cells should jump by 180^o as the spatial frequency of the stimulus crosses k_c. This conclusion is robust to the details of the I-cell network.

S2.3 Linearization of the Nonlinear Model

With the addition of an expansive nonlinearity, we predicted that our network would transition from non-ISN to ISN regimes with increasing input strength. This is because the effective synaptic strength increases with increasing input strength, until at some point the effective $E \to E$ connections become strong enough to be unstable in the absence of feedback inhibition. The effective synaptic strength – the change in postsynaptic firing rate for a

given change in presynaptic firing rate – increases because it is the product of the biophysical synaptic strength (*e.g.*, the current injected in the postsynaptic cell) and the postsynaptic gain (the change in postsynaptic firing rate for a given current injection). Given the expansive nonlinearity, postsynaptic gain increases with postsynaptic firing rate and thus with input strength.

This input dependence of the dynamic regime can be understood by linearizing the dynamics around the fixed-point firing rates. We let $\mathbf{r}(x) = \mathbf{r}^{\mathrm{FP}}(x) + \delta\mathbf{r}(x)$ where $\mathbf{r}^{\mathrm{FP}}(x) \equiv \begin{pmatrix} r_E^{\mathrm{FP}}(x) \\ r_I^{\mathrm{FP}}(x) \end{pmatrix}$ is the vector of fixed-point firing rates and $\delta\mathbf{r}(x)$ is the deviation of the firing rates from the fixed point. Defining $\mathbf{T}$ and $\mathbf{W}(x)$ as in Section S2.1 and $\mathbf{1}$ as the two-dimensional identity matrix, the linearized dynamics are $\tau_E \frac{d\delta\mathbf{r}(x)}{dt} = \sum_{x'} \hat{\mathbf{W}}(x,x')\delta\mathbf{r}(x')$ where $\hat{\mathbf{W}}(x,x')$, the Jacobian matrix of the dynamical system, is given by $\hat{\mathbf{W}}(x,x') = \mathbf{T}^{-1}\left(\mathbf{\Phi}(x)\mathbf{W}(x-x') - \mathbf{1}\right)$ with $\mathbf{\Phi}(x) = nk^{1/n}\begin{pmatrix} r_E^{\mathrm{FP}}(x)^{\frac{n-1}{n}} & 0 \\ 0 & r_I^{\mathrm{FP}}(x)^{\frac{n-1}{n}} \end{pmatrix}$. The linearized dynamics will accurately describe model behavior so long as $\mathbf{r}$ is sufficiently close to $\mathbf{r}^{\mathrm{FP}}$. As in Section S2.1 for $\mathbf{W}$, we write $\hat{\mathbf{W}} = \begin{pmatrix} \hat{\mathbf{W}}_{\mathrm{EE}} & -\hat{\mathbf{W}}_{\mathrm{EI}} \\ \hat{\mathbf{W}}_{\mathrm{IE}} & -\hat{\mathbf{W}}_{\mathrm{II}} \end{pmatrix}$ to refer to the full matrix of linearized connections, where the submatrix $\hat{\mathbf{W}}_{\mathrm{XY}}$ has elements $\left(\hat{\mathbf{W}}_{\mathrm{XY}}\right)_{\mathrm{ij}} = \hat{\mathbf{W}}_{\mathrm{XY}}(x_i, x_j)$.

We can numerically calculate the eigenvalues and eigenvectors of the effective linear weight matrix, $\hat{\mathbf{W}}$, at a given steady-state and use them to predict the effective dynamic regime of the nonlinear network. For the fixed point to be stable, all eigenvalues of $\hat{\mathbf{W}}$ must have negative real part. We roughly equate[5] the ISN regime with at least one pattern of excitatory activity being unstable in the absence of feedback inhibition, meaning that at least one eigenvalue of $\hat{\mathbf{W}}_{\mathrm{EE}}$ has positive real part; this will occur when the values of $r_E^{\mathrm{FP}}(x)$ become sufficiently large.

As a simple test, we stimulated E and I cells in the 1-D nonlinear model of Fig. 3 with a small, centrally-located stimulus of strength c and considered the linearization about the corresponding fixed point. All eigenvalues of $\hat{\mathbf{W}}$ have negative real part for all stimulus strengths tested (up to $c = 100$). We then perturbed only the stimulated inhibitory cells with a small additional excitatory input, and recorded the responses of the E and I cells at the stimulus center. We observe, as expected, that the stimulus strength at which the largest real part of an eigenvalue of $\hat{\mathbf{W}}_{\mathrm{EE}}$ becomes positive coincides closely with the stimulus strength at which additional drive to inhibitory cells causes a decrease in steady-state inhibitory firing rate (Supplemental Fig. S2D).

We also consider linearization about the steady-state response to a full-field stimulus of

[5]Why this is a rough rather than exact correspondence: The condition that at least one eigenvalue of $\hat{\mathbf{W}}_{\mathrm{EE}}$ has positive real part ensures that there is at least one pattern of E-unit activity that is unstable in the linear regime. By the reasoning of section S2.2.3, this ensures that a pattern of small input to I cells that causes a new steady state in which the only change is a decrease in amplitude of this unstable E-unit pattern must result in the E cells receiving less inhibition in that new steady state. This is the paradoxical signature of the ISN. However this does not ensure that any particular stimulus to I cells, such as the uniform input over a 1^{o} region used in Supplemental Fig. S2D, will yield a paradoxical response.

strength c. We use the linearized weights to calculate the network resonant and critical frequencies.[6] All three frequencies monotonically increase with stimulus strength, and once stimulus strengths reach moderate levels both E and I resonant frequencies are below the critical frequency, meaning that the network shows ISN behavior for stimuli at those frequencies (Supplemental Fig. S2E). The analytically calculated frequencies from the linearization describe most-amplified (resonant) frequencies for small sinusoidal deviations about the uniform stimulus of strength c, but they reasonably approximate the preferred CM frequencies in the actual network (Fig. 5D), which involve responses to stimuli that oscillate sinusoidally between strength 0 and strength c.

[6]Because the stimulus is spatially uniform, steady-state firing rates are spatially uniform except for boundary effects. Therefore, away from the boundaries, the linearized weight submatrices $\hat{\mathbf{W}}_{\mathrm{XY}}$, $X, Y \in E, I$, remain translation-invariant, of Gaussian shape about each position but with size scaled by steady state firing rates according to $\mathbf{\Phi}$ (which does not vary with position). As a result, we expect the eigenvectors of the submatrices to closely approximate the Fourier modes, with real eigenvalues that decrease with frequency. Accordingly, we diagonalize each linearized submatrix with eigenvalues ordered from largest to smallest real parts with imaginary part discarded, and make the ansatz that the weight matrix $\hat{\mathbf{W}}$ in the Fourier basis is well approximated by the matrix of these four diagonal submatrices (with minus signs for the submatrices $\hat{\mathbf{W}}_{\mathrm{XY}}$ for $y = I$). That is, we equate $\hat{W}_{\mathrm{XY}}(k)$ with the k^{th}-largest eigenvalue in the real diagonal submatrix $\hat{\mathbf{W}}_{\mathrm{XY}}$. We then can calculate the equivalent of $\mathcal{L}_{\mathrm{E}}(k)$ and $\mathcal{L}_{\mathrm{I}}(k)$ in this representation (Eqs. S3-S4), with replacements $(1 + \tilde{W}_{\mathrm{II}}(k)) \to \hat{W}_{\mathrm{II}}(k)$, $(1 - \tilde{W}_{\mathrm{EE}}(k)) \to -\hat{W}_{\mathrm{EE}}(k)$, $\tilde{W}_{\mathrm{EI}}(k) \to \hat{W}_{\mathrm{EI}}(k)$, $\tilde{W}_{\mathrm{IE}}(k) \to \hat{W}_{\mathrm{IE}}(k)$, $\mathrm{Det}\,(\mathbf{1} - \tilde{\mathbf{W}}(k)) \to \mathrm{Det}(-\hat{W}(k))$. We find the resonant network frequencies from the peaks of $\mathcal{L}_{\mathrm{E}}(k)$ and $\mathcal{L}_{\mathrm{I}}(k)$ vs. k. The critical frequency is found as the first frequency for which the corresponding eigenvalue of $\hat{\mathbf{W}}_{\mathrm{EE}}$ is < 0.

S3 Supplemental Figures

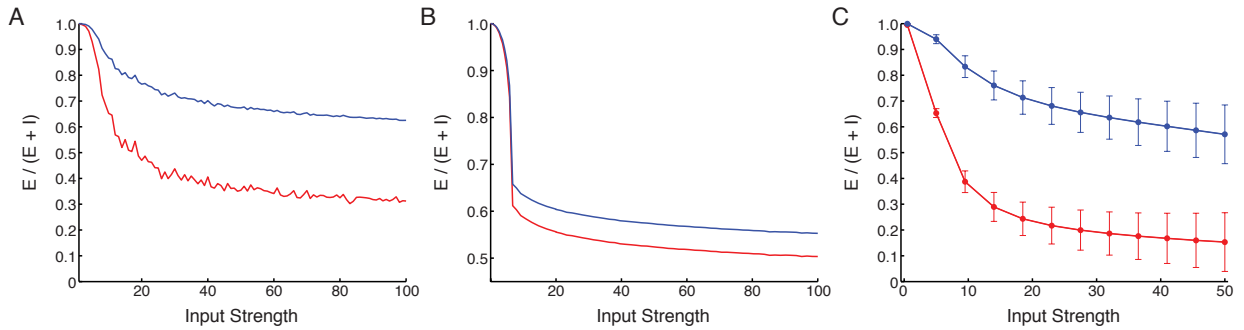

Figure S3:

Increasing dominance of network input by inhibition with increasing input strength, using protocol of Shao et al. (2013) (related to Figs. 1F, 3B, and 6C). In Figs. 1F, 3B, and 6C, we showed that the ratio $E/(E+I)$ of network-driven excitation E to network-driven inhibition I grows with increasing stimulus strength, as in Fig. 3E of Shao et al. (2013). However, in our model figures, the input was given equally to E and I cells. Here we show that the same result holds when we more closely model the protocol of Shao et al. (2013). In Shao et al. (2013), channelrhodopsin (ChRh) was expressed in L2/3 of mouse S1 in around 25% of E cells (ChRh was expressed in $21.1 \pm 0.9\%$ of all neurons, and about 80% of neurons are E cells). Then in cortical slices, intracellular recordings were made from non-ChRh-expressing E cells to assay the strength of excitatory and inhibitory input, E and I, evoked by light stimulation of the ChRh-expressing E cells. To model this, we chose E cells randomly with probability 0.25 to receive input (input identical to that in main-text figures, except set to zero for all I cells and for E cells with probability 0.75), and recorded from the E cells not receiving input (red curves) or from the I cells (blue curves). Results corresponding to Fig. 1F (**A**), Fig. 3B (**B**), or Fig. 6C (**C**) all show qualitatively the same behavior as the original figures: increasing dominance of network input by inhibition with increasing stimulus strength.

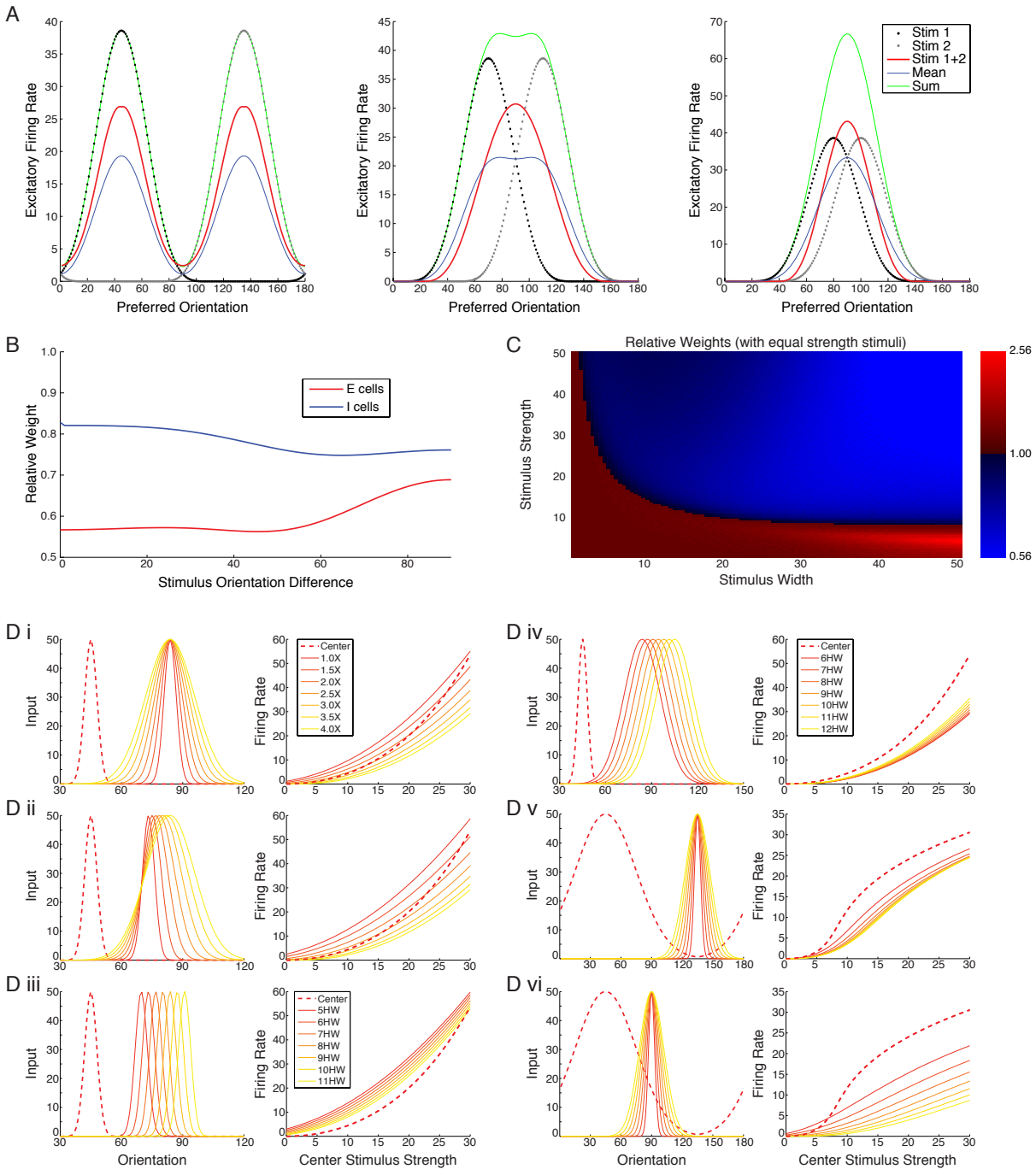

Figure S4:

Normalization in the ring model of Figure 1. A,B: Non-orthogonal grating pairs also show sublinear addition. **A**: E-cell responses to the two stimuli presented individually (dotted) and to the simultaneous presentation of both stimuli (red), as well as the sum (green) and mean (blue) of the individual responses, for orientation differences of 90°, 40°, and 20°. **B**: The sublinear weights w for E and I cells vs. stimulus orientation difference. (Continued on next page.)

Figure S4:

(Continued). w is defined as in Fig. 1I. Strength of each stimulus is $c = 50$ for all panels. **C**: The switch from supra- to sub-linear addition occurs at lower stimulus strengths for wider stimuli, as suggested by the fact that larger stimulus widths switch from being facilitating to suppressive at lower stimulus strengths (**C**, and Figs. 3E, 1J, 6H and Supplemental Fig. S8D). The relative additive weights for excitatory cells in response to two equal-strength, equal-width orthogonal stimuli (orientation difference 90°) are plotted as a function of stimulus width and stimulus strength. For comparison, simulations in **B** and in Fig. 1G used stimulus strength $c = 50$ and stimulus width $\sigma_{FF} = 30°$. **D.** Small but not large surround stimuli, relative to summation field size, can facilitate response to a low-contrast center. **D(i-vi)**. Left panels show stimuli: red dashed curve, center stimulus for $c = 50$, always presented at orientation 45° with strengths varying from $c = 0$ to $c = 50$ by 1; yellow through red solid curves, surround stimuli varying as indicated in legend, $c = 50$ in all cases. Right panels show response vs. center contrast: red dashed curve, response to center stimulus alone; yellow through red solid curves, response to center plus correspondingly colored surround stimulus. **D(i-iv)**. Small center stimulus: center size is summation field size for $c = 50$, which is $\sigma_{FF}^{ctr} = 3$ (Fig. 1J). In **(i-iv)** we will describe separation of center and surround in units of half-widths (HW), meaning the separation between the largest orientation corresponding to half width at half height (HWHH ORI) of the center grating, and the smallest HWHH ORI of the surround grating. **D(i)**. Surround stimulus is varied in size from 3 to 12 in steps of 1.5. Surround gratings have common center position, set so that largest surround is separated by 6 HW. **D(ii)**. Surround stimuli vary in size as in **(i)**, but their positions are varied so that all surround stimuli have separation 6 HW. **D(iii)-(iv)**. Qualitative effects of **(i)-(ii)** are insensitive to position. **D(iii)**. Surround stimulus equal in size to center stimulus, varied in position from 5 to 11 HW in steps of 1 HW. All curves have wide region of facilitation. **D(iv)**. Large surround stimulus (size 12) is varied in position from 6 to 12 HW in steps of 1 HW. All curves show only suppression. **D(v)-(vi)**. Sufficiently small and near surrounds can facilitate even large center stimuli. Here, center size is large ($\sigma_{FF}^{ctr} = 30$, as in all other ring model simulations) and surround is small (varying from 3 to 12 in units of 1.5). Distances are between center positions of the two gratings. **D(v)**. Surrounds orthogonal to center (90° distance). At this distance surrounds are only suppressive. **D(vi)**. Surround are 45° from center. Here, small surrounds can facilitate low-contrast center. Note, the case of center and surround both of size 30 produces only suppression, as illustrated in **A**.

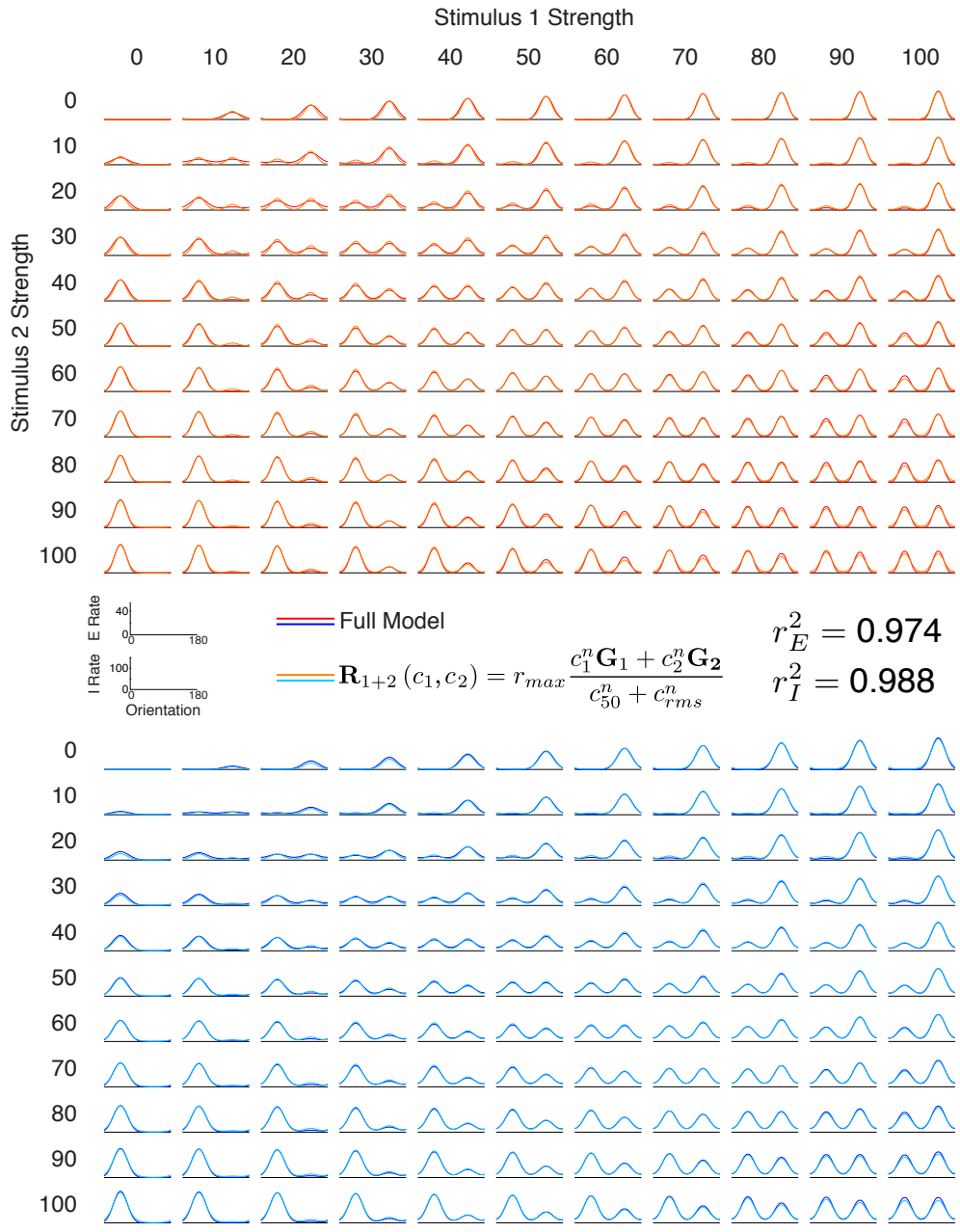

Figure S5:

Ring model results of Fig. 1 are well fit by equations of the normalization model. We presented pairs of orthogonal stimuli (at 45° and 135°). Each stimulus was presented at 21 stimulus magnitudes c, from 0 to 100 in steps of 5. This yields $21 \times 21 = 441$ firing rate curves for both E and I, of which $11 \times 11 = 121$ are illustrated. Each curve shows firing rate (y axis) vs. ring coordinate from $\theta = 0°$ to $\theta = 180°$ (x axis). Separately for E and I, these 441 curves were used to fit equations of the phenomenological normalization model (Busse et al. 2009), shown in figure. Red (E) and blue (I) curves show responses of full model, while orange (E) and cyan (I) curves show fit of normalization model (discrepancies become visible when figure is expanded). (Continued on next page.)

Figure S5: (continued) In the normalization model equation, $\mathbf{R}_{1+2}(c_1, c_2)$ is the vector of responses across the population (E or I) to presentation of stimuli 1 and 2 at strengths c_1 and c_2, respectively, $c_{rms} = \sqrt{c_1^2 + c_2^2}$, and $\mathbf{G}_1$ and $\mathbf{G}_2$ are vectors of responses across the population given by identical circular Gaussians, with amplitude A and width parameter p, centered at 45° and 135°, respectively. This model has five free parameters: r_{max}, c_{50}, n, A, and p. These were fit to give the least squared error across the 441 curves. r_E^2 and r_I^2 are the R^2 values (% of variance explained) for the fits for E and I curves, respectively. The best-fit parameters are: E units, $n = 1.2278$, $c_{50} = 24.4622$, $r_{\max} = 47.7657$, $A = 1.6441$, $p = 3.3977$; I units, $n = 1.4213$, $c_{50} = 80.2834$, $r_{\max} = 149.9930$, $A = 2.9298$, $p = 2.3514$. Note that this model cannot fit the supralinear summation we see for stimulus strengths below 10 (Fig. 1I), because $\mathbf{G}_1$ does not contribute appreciable activation to the region activated by $\mathbf{G}_2$ and vice versa. Because 19 of 20 nonzero strengths used here were 10 or above, this did not greatly affect fit quality. Circular Gaussians have the form $G(\theta) = Ae^{p*cos(2(\theta-\theta_0))}/(2\pi\mathcal{I}_0(p))$, where θ_0 is the respective stimulus orientation and $\mathcal{I}_0$ is the modified Bessel function of the first kind ("besseli" in Matlab) of order 0.

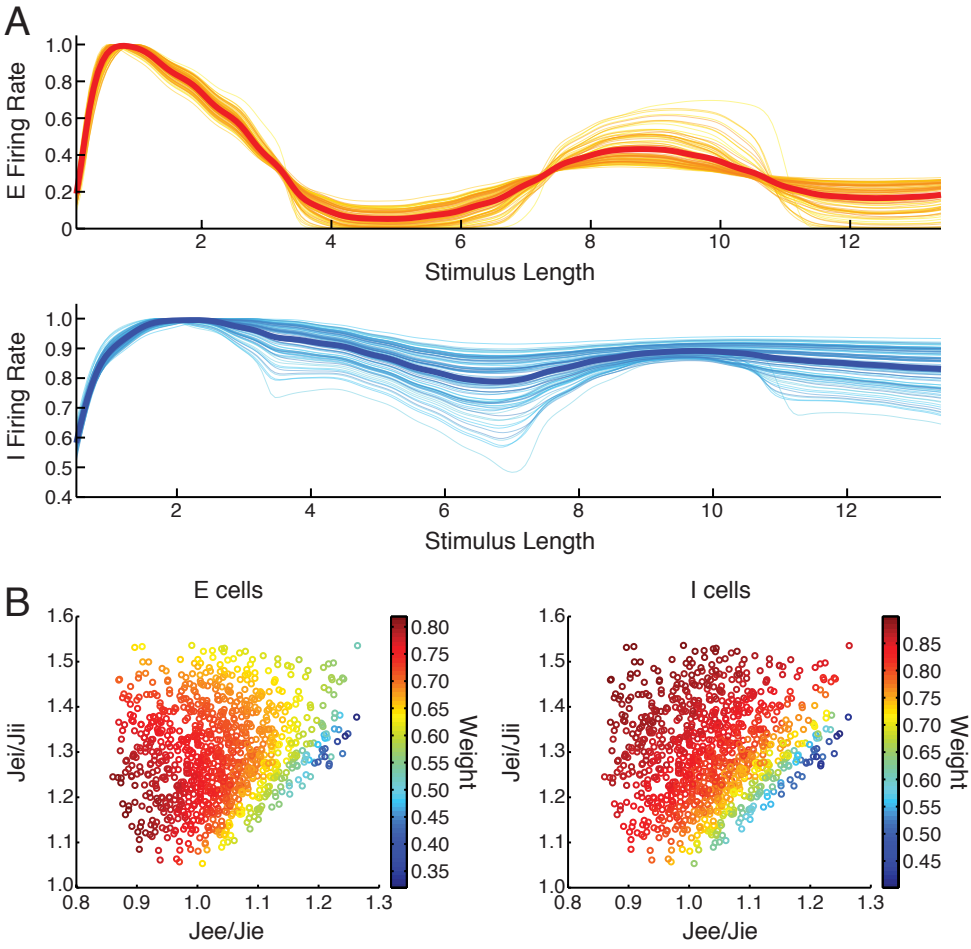

Figure S6:

Robustness of results for ring model (Figure 1) and Nonlinear 1-D model (Figure 3). For Fig. 3 (**A**) and Fig. 1 (**B**), we show that a basic feature of the model response stays qualitatively invariant, changing smoothly and continuously, as parameters are changed, indicating that model behavior does not require fine tuning of parameters. **A.** Length-tuning curves for nonlinear 1-D model of Fig. 3 (top: E cell; bottom: I cell) under weight perturbations. 100 simulations were run, identical to Fig. 3C for $c = 31$, except that in each simulation, each of the four weight-strength parameters (J_{EE}, J_{IE}, W_{EI}, W_{II}, defined in Section S1.1.2) were randomly chosen from a uniform distribution covering $\pm 10\%$ about the value used for Fig. 3. The length-tuning curves from Fig. 3C are shown in bold, and those from the 100 randomly-perturbed simulations are shown as thin lines. **B.** Summation weights w for ring model of Fig. 1 (E cells: left; I cells: right) under weight perturbations. As in Fig. 1I, two orthogonal gratings of equal strength (here, $c = 100$) were shown, and the weight w was determined as that giving least-squared-error fit to the equation $R_{12} = w(R_1 + R_2)$ where R_{12} is the vector of responses across the population of E or I cells to the simultaneous presentation of both gratings, while R_1 and R_2 are the vector responses to one or the other grating alone. 1000 simulations were run, in each of which the four weights J_{EE}, J_{IE}, J_{EI}, and J_{II} (Section S1.1.2)) were each drawn from uniform distributions covering $\pm 10\%$ about the value used in Fig. 1. Each dot presents results from one simulation, with color indicating the resulting weight w. Sublinearity of summation grows stronger (w decreases) with increasing bias of excitatory projections toward E cells (increasing J_{EE}/J_{IE}) and, to a lesser extent, with increasing bias of inhibitory projections toward I cells (decreasing J_{EI}/J_{II}).

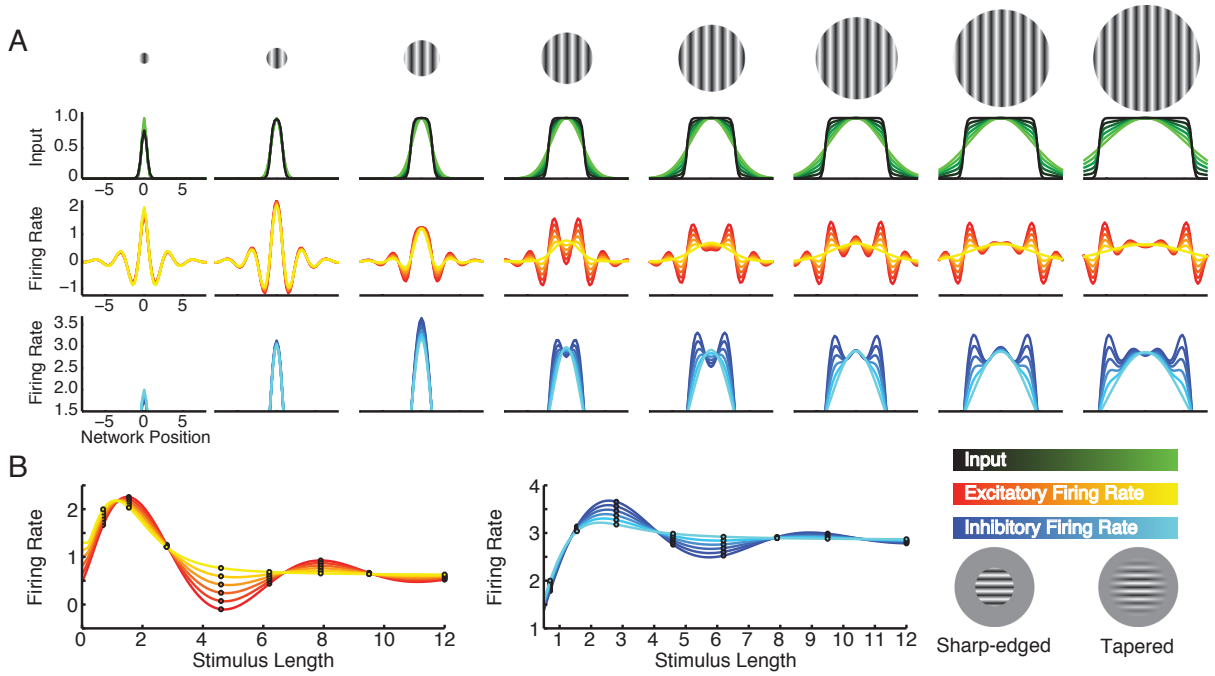

Figure S7:

Effects of varying input shape, from sharp-edged to smoothly tapered, in the linear model of Fig. 2. A. Input (top row) and corresponding E (middle row) and I (bottom row) activity vs. spatial position (x-axes). This repeats Fig. 2B, but now with input shape (top) interpolating, as line colors move from black to light green ("Input" in legend, bottom right), from sharp-edged (black lines, as used in Fig. 2) to Gaussian (lightest green lines) (see Section S1.1.1 for equations for input shapes). Corresponding E (middle) and I (bottom) firing rates are shown by lines varying (see legend) from red to yellow (E) or blue to cyan (I) as inputs vary from sharp-edged to Gaussian. For larger stimuli, more smoothly-tapering stimuli do not yield spatially periodic activity, for reasons described in Section S2.1.3. **B** E (left) and I (right) length tuning curves for cell at middle of grid. This repeats Fig. 2C with the array of input shapes from **A**. Colors as in **A** and legend. More smoothly-tapering stimuli do not yield periodic length tuning curves.

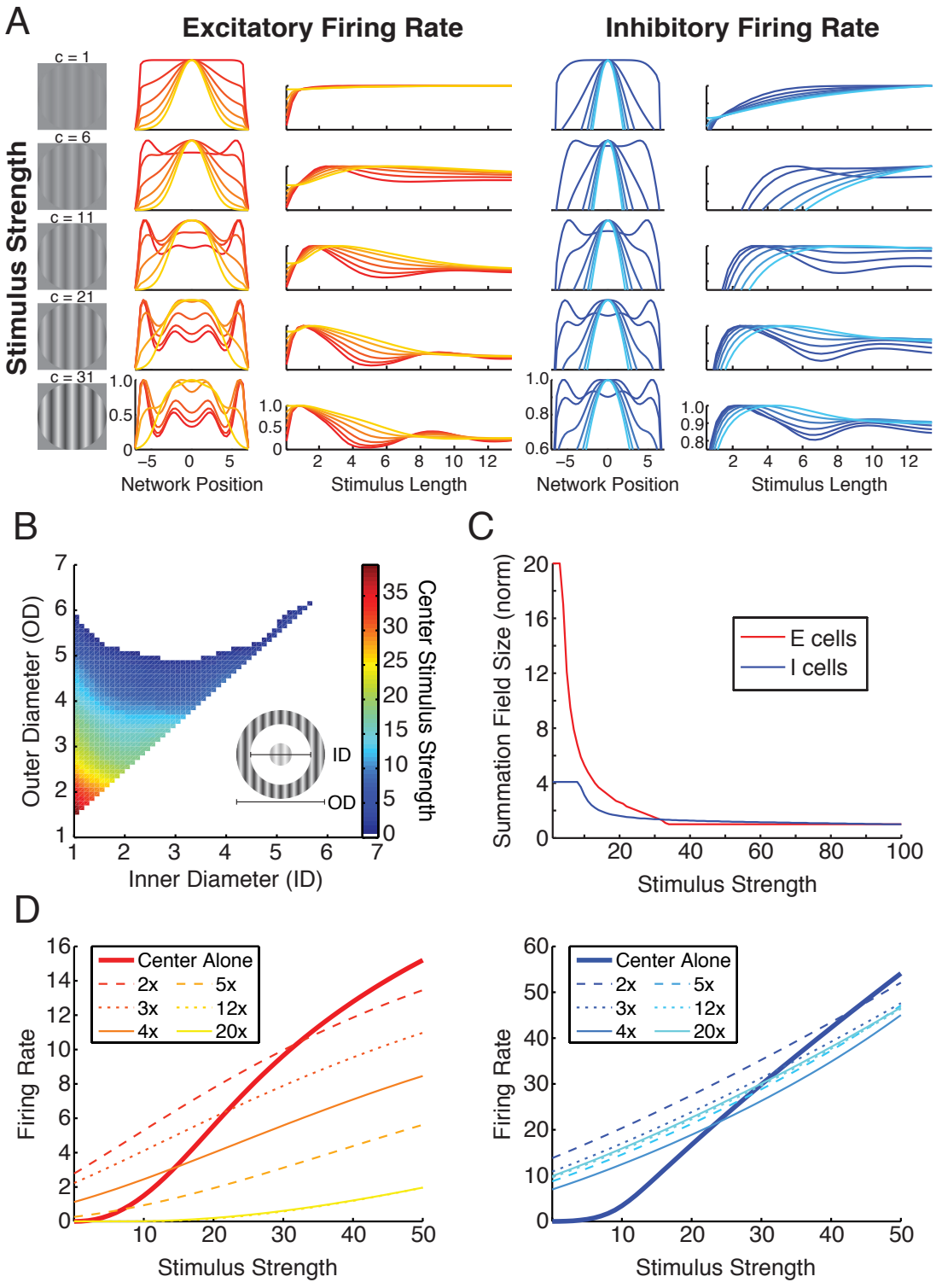

Figure S8:

Nonlinear 1-Dimensional Spatial Model of Figure 3. **A**: Periodicity in spatial activity profiles and length tuning curves depends on input shape. (Continued on next page.)

Figure S8:

(Continued). This panel repeats Fig. 3C, but with the array of input shapes of Fig. S7, ranging from sharp-edged (as used in Fig. 3) to Gaussian. Colors as in Fig. S7, with red to yellow (E) and blue to cyan (I) corresponding to sharp-edged to Gaussian-shaped stimuli. Conventions otherwise as in Fig. 3C. As in the linear model (Fig. S7), periodicity in spatial activity patterns and length tuning curves disappears as stimuli become more smoothly tapering. **B**: Dependence of facilitation on position as well as size of surround. Center stimulus fills $c = 50$ summation field, as in Fig. 3E. Surrounds ($c = 50$) are "annular", which in 1D means segments equally spaced on either side of center stimulus (inset shows inner diameter (ID) and outer diameter (OD) for 2D case; 1D stimulus is a slice through the center of the 2D stimulus). Inner diameter of annular stimulus (distance between inner edges of the two segments), in units of center stimulus diameter, given by x-axis (= 1 in Fig. 3E) and outer diameter by y-axis (=total stimulus size in Fig. 3E). Figure shows heat map of center stimulus strength at which effect of surround switches from facilitation to suppression for E units. White indicates that surround is never facilitating (lowest center strength examined, $c = 0.5$). For larger inner and outer diameters up to 20, there is no facilitation except for inner diameter 1 and outer diameter 14-17.5 for very low center strengths (switch at center c ranging from 2 to 4.5). Note that this panel explains why high-contrast surrounds can facilitate responses to a low-contrast center (**D**; Fig. 3E), whereas in the ring model a high-contrast orthogonal grating only suppressed response to a low-contrast grating (Fig. 1H). These results are seen to be consistent when surround size is expressed in terms of high-contrast summation-field size (hcSFS). Here, facilitation occurs for surrounds smaller than about 5 times the hcSFS. In the ring model, the gratings were about 10× larger than the hcSFS (compare Fig. 1J). Smaller high-contrast orthogonal gratings can instead yield facilitation (Supplemental Fig. S4 C,D). **C-D**: Contrast-dependent changes in summation field size and surround effects are insensitive to stimulus shape. The simulations from Figs. 3D-E are repeated but with Gaussian-shaped rather than sharp-edged stimuli. The results are essentially the same: (**C**) shrinking of summation fields with increasing contrast and (**D**) a switch from surround facilitation to surround suppression with increasing center contrast for smaller, but not larger, surround stimuli for E cells (left) and for all surround stimuli for I cells (right). In **D**, center stimulus is Gaussian-shaped with full-width at half-height (FWHH) 0.55° for E, 1.9° for I units, and stimulus strength as shown on x-axis; surround stimuli are sharp-edged stimuli with sizes, positions, and strengths ($c = 50$) exactly as in Fig. 3E.

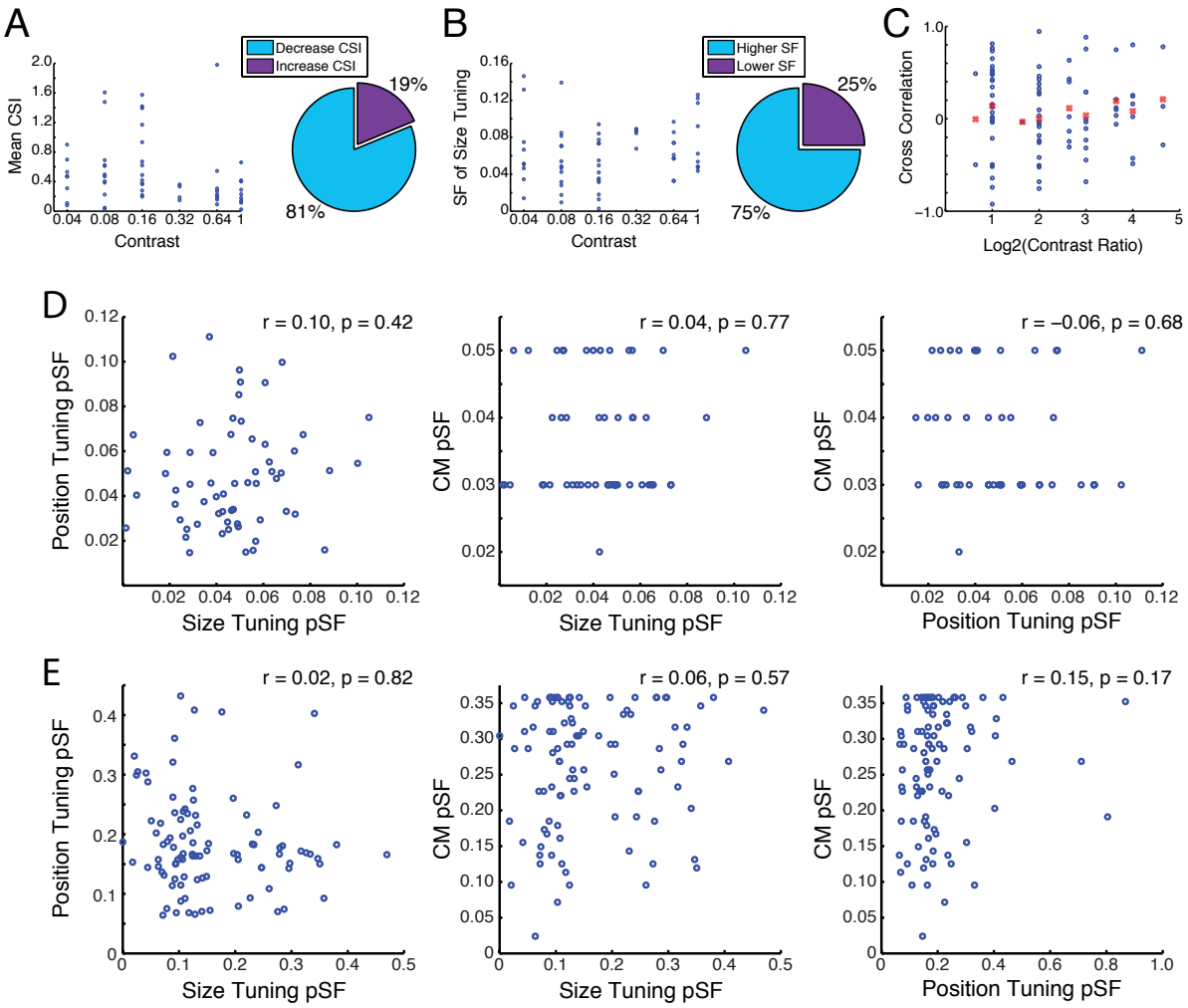

Figure S9:

Experimental Results (related to Figs. 4 and 5). A-C: Size-tuning at multiple levels of stimulus contrast. We were only able to study this in a small number of cells (16): 4 studied at 2 contrasts, 2 at 3 contrasts, 6 at 4 contrasts, and 4 at 5 contrasts. **A.** Our results are consistent with those of Wang et al. (2009). They studied "counter-suppression" (CS) – a re-emergence of activity at larger stimulus sizes after surround suppression. They defined a CS index (CSI): CSI $= \frac{R_{cs}-R_{min}}{R_{max}}$, where R_{max} is the firing rate at the summation field peak (the first peak in the size-tuning curve); R_{min} is the minimum firing rate in the surround suppressed region (the first dip); and R_{cs} is the maximum rate for still larger stimuli. They found that CSI was largest at low contrasts, which seems counter to our prediction that periodicity of length tuning curves is stronger at higher contrasts. We suggest that CSI decreases with contrast because at low contrast, size tuning curves can be fundamentally summating/facilitating – responses increase with size, but with some wiggles and dips along the way. Such continued facilitation after the first dip will produce the largest R_{cs} and hence the largest CSI. This interpretation is supported by findings of Wang et al. (2009) that responses at maximal stimulus size were larger, relative to R_{min}, and suppression indices lower at low contrast than at high contrast. (Continued on next page.)

Figure S9:

(Continued). To calculate CSI in our own data, we removed subjectivity by using all extrema in each size-tuning curve, calculating CSI for each consecutive peak-trough-peak triplet and taking the average of these as the curve's CSI. Dots represent CSI in the 16 cells for each combination of cell and contrast. Consistent with our interpretation, in our data, which by multiple other measures accords with our model's predictions, we also observe a decrease in CSI with increasing contrast, with 13/16 cells (81%) showing a higher CSI at the lowest contrast studied than at the highest contrast studied ($p < 0.022$, two-sided binomial test of null hypothesis that CSI equally likely to be highest at lowest or highest contrast). **B.** From our fit to the SSM model, we see an increase in dominant spatial frequency with increasing contrast, as the model predicts. 12/16 neurons (75%) showed a higher size-tuning spatial frequency at the highest contrast studied than at the lowest contrast studied. This trend did not reach statistical significance in a two-sided test ($p < 0.077$, two-sided binomial test of null hypothesis that frequency equally likely to be highest at lowest or highest contrast) but was significant at the 0.05 level in a one-sided binomial test ($p < 0.0385$). **C.** To determine whether spatially periodic responses might arise from static properties of the functional architecture, such as the periodicity of orientation columns, rather than arising dynamically as a contrast-dependent spatial resonance, we measured the cross-correlations of all pairs of size-tuning curves measured for a given cell at two different contrasts (after discarding the first 40% of the curve, which in general for all cells simply captures spatial summation). We plot this against the base-2 log of the ratio of the stimulus contrasts. The mean of each distribution is indicated by a red X. For all contrast ratios (except for ratio 3.125, log ratio 1.644, for which there was only 1 data point), the median was not significantly different from 0 (two-sided one-sample Wilcoxon signed rank test). (The means also were not significantly different from zero as judged by a two-sided t-test, with all p-values ≥ 0.13, but because the data may not be normally distributed these statistics are not reliable, hence we used the non-parametric Wilcoxon test). Thus, peak and trough locations for a given cell vary with contrast in a manner inconsistent with a static origin of the periodicity. For increasing contrast ratios, statistics for the Wicoxon test are: $N = (2, 28, 21, 7, 11, 6, 7, 3)$ curves; $p = (1.00, 0.11, 0.99, 0.47, 0.97, 0.094, 0.69, 0.75)$; signed rank $= (1, 273, 116, 19, 32, 19, 17, 4)$. **D,E**: Lack of correlation between the three measures of network resonant frequency (best fit frequencies to size-tuning and position-tuning curves and contrast modulation pSF) in experiments (**D**) and in model (**E**). Experiments: all cells for which we had both forms of data; model: 100 randomly selected E units; in both cases, restricted to cells or units for which SSM gave a better fit than DOG by nested F-test for length and/or position tuning if used in given panel. The calculated correlation coefficient and its p-value are indicated on each plot. In both experiments and model, there is no significant correlation between any pair of the three spatial frequencies, presumably reflecting different subnetworks of cells being recruited by each stimulus paradigm. For three panels, left to right: Experiments, $n = 62$, 50, 45; $DF = 60$, 48, 43; $t = 0.817$, 0.292, -0.417; Model, $n = 86$, 96, 88; $DF = 86$, 96, 88; $t = 0.227$, 0.575, 1.376.

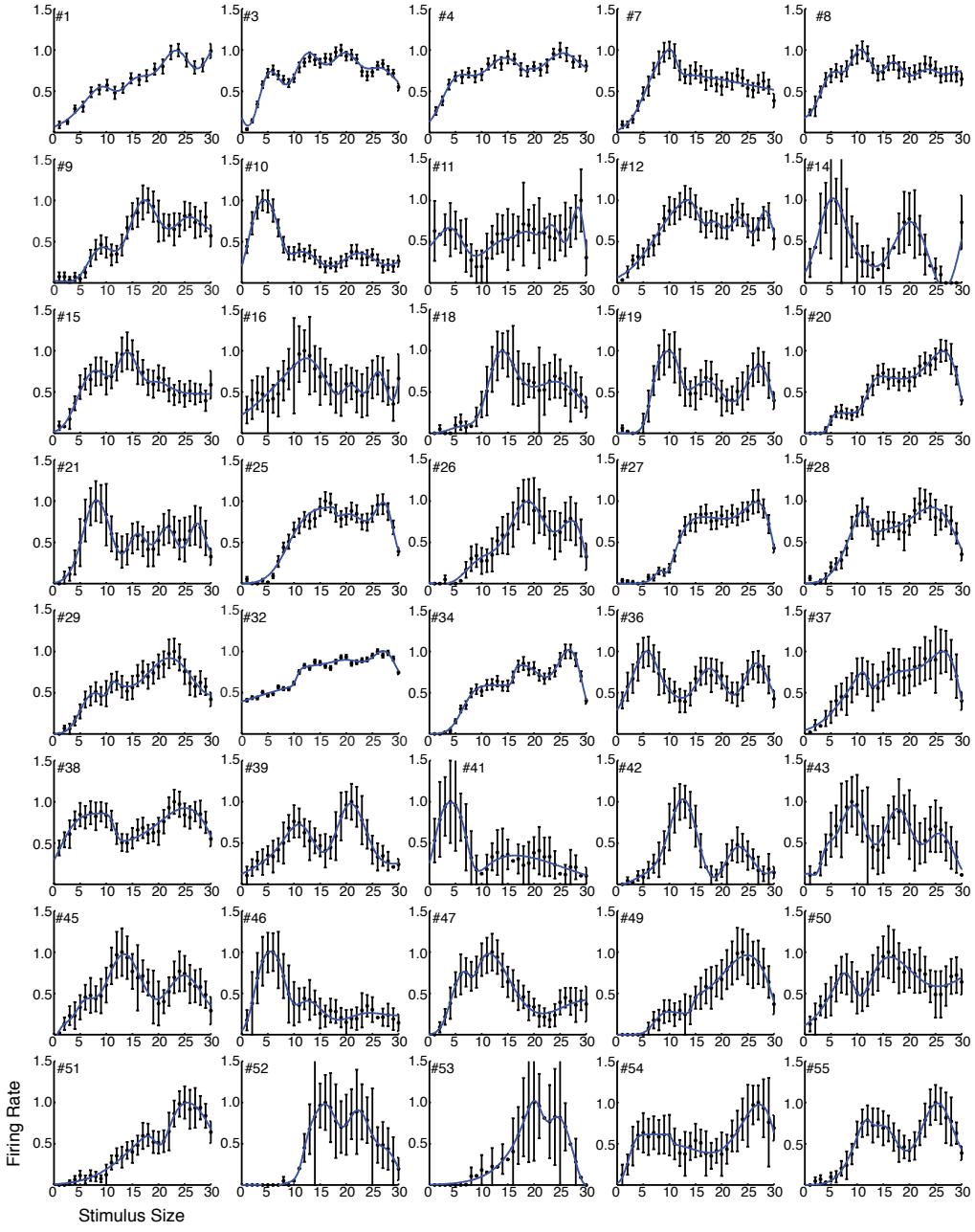

Figure S10:

All experimentally measured size-tuning curves (related to Fig. 4). Cell identification (ID) numbers are indicated. Data points: tuning curve and standard deviation as computed by maximum likelihood estimation (Section S1.4.2). Blue curves: best fit of SSM model curve. Statistics for goodness of fit of SSM vs. DOG model are in Supplemental Tables S1 (for 8-parameter DOG fit) and S2 (for 7-parameter DOG fit). Cells illustrated in Fig. 4A are #42 (left) and #36. (Continued on next page.)

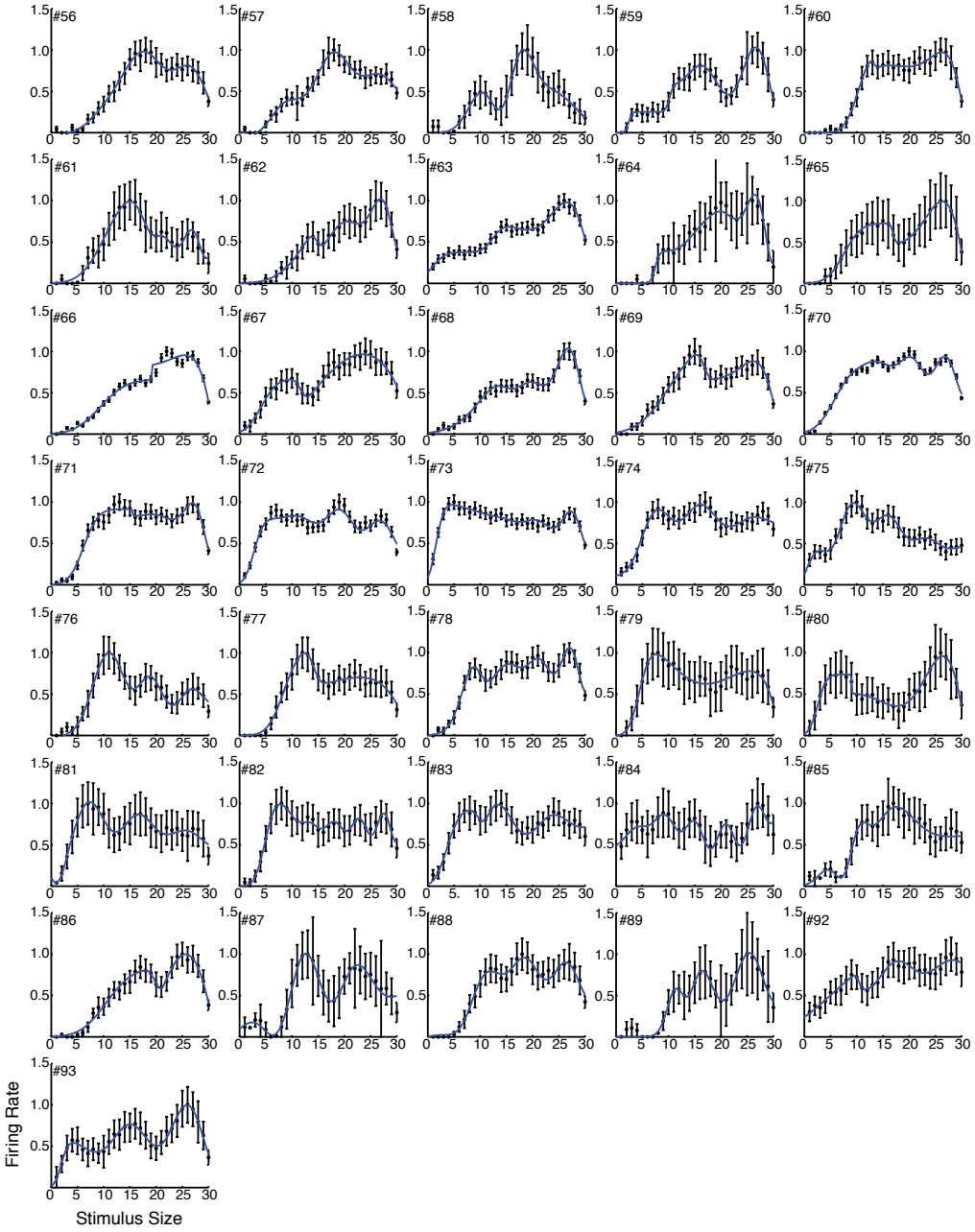

Figure S10:
All experimentally measured size-tuning curves (related to Fig. 4); (continued).

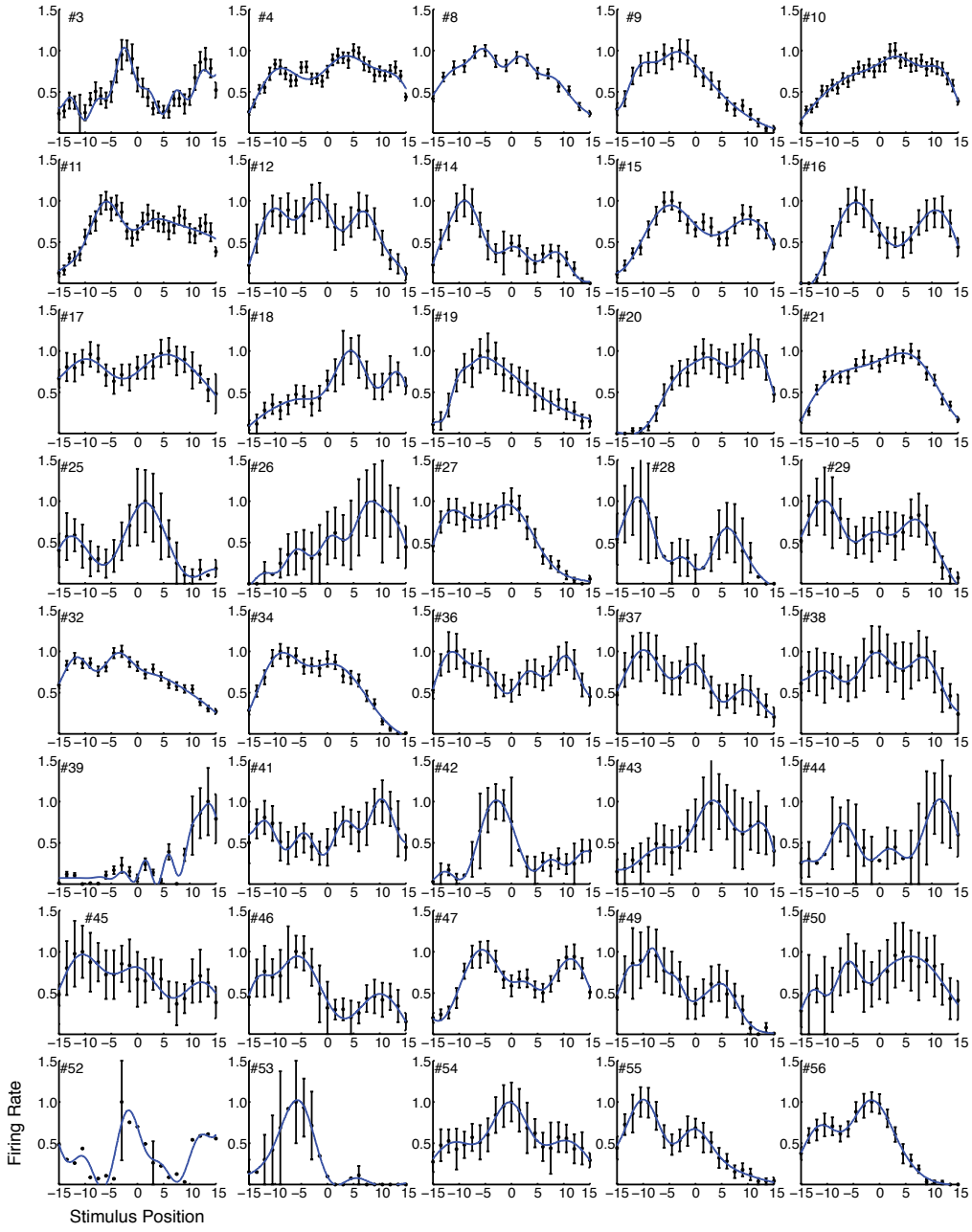

Figure S11:

All experimentally measured position-tuning curves (related to Fig. 4). Cell ID numbers are indicated. Data points: tuning curve and standard deviation as computed by maximum likelihood estimation (Section S1.4.2). Blue curves: best fit of SSM model curve. Statistics for goodness of fit of SSM vs. DOG model are in Supplemental Table S3. Cells illustrated in Fig. 4D are #16 (left) and #79. (Continued on next page.)

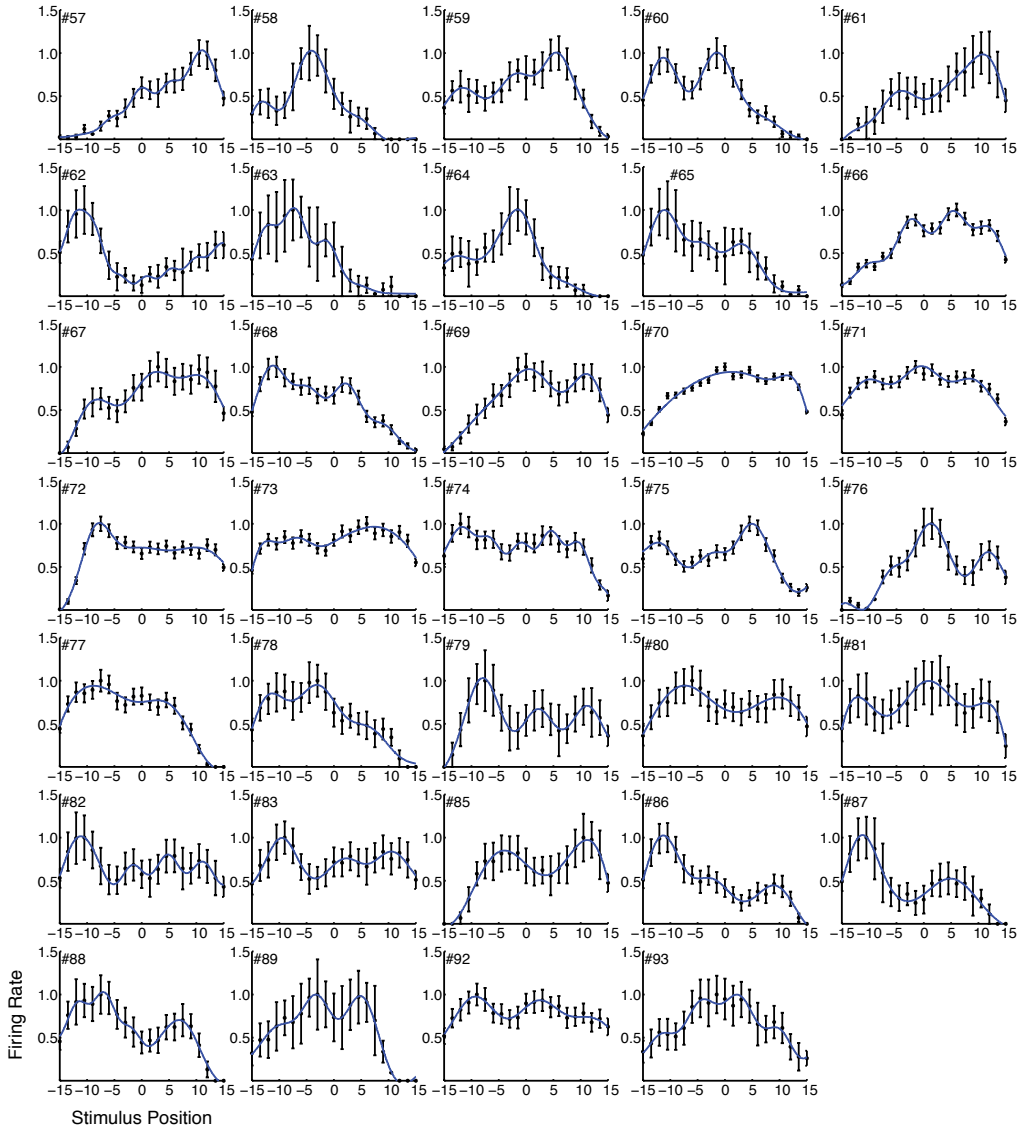

Figure S11:
All experimentally measured position-tuning curves (related to Fig. 4); (continued).

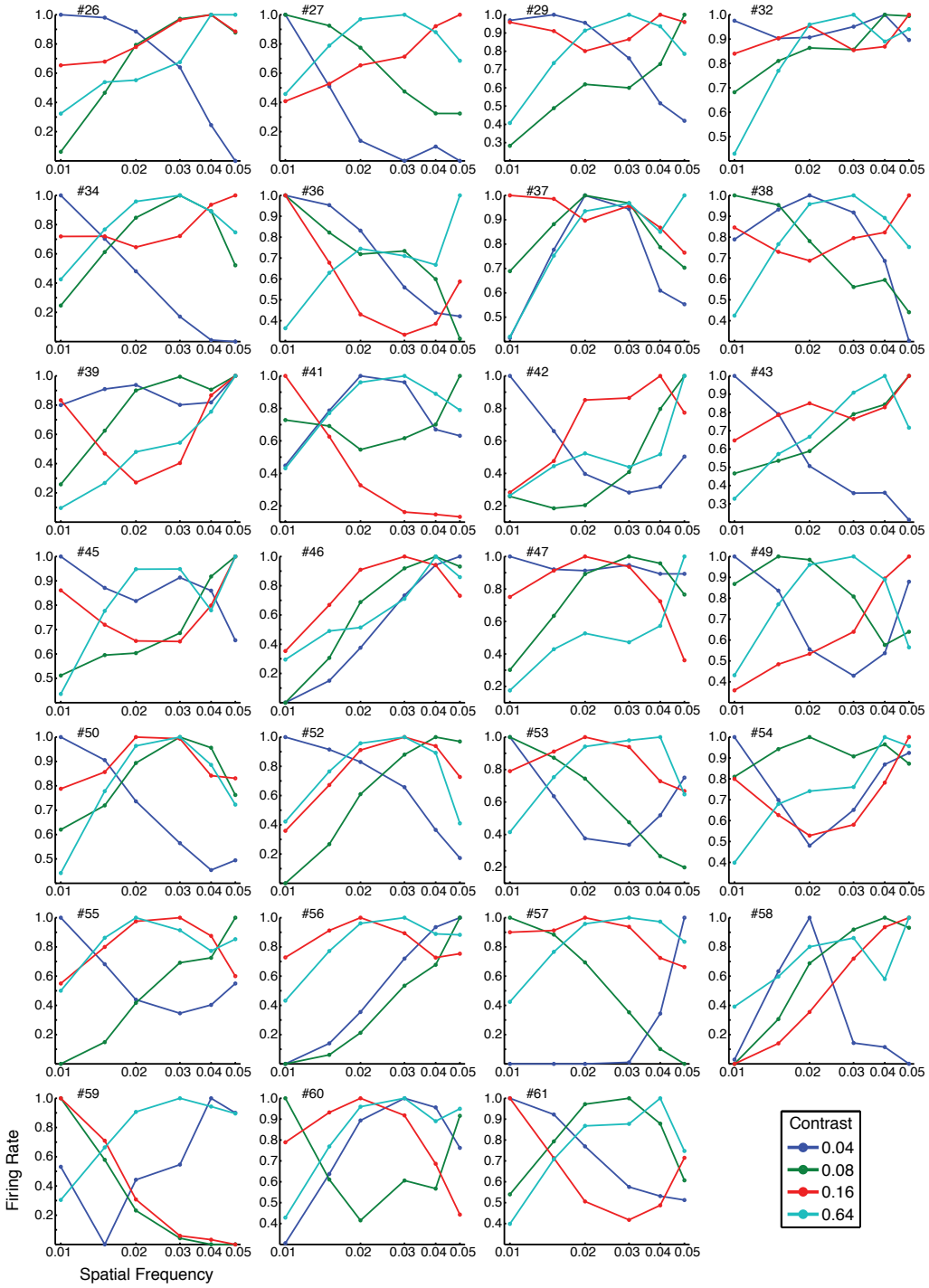

Figure S12:

All experimentally measured contrast-modulation curves (related to Fig. 5). Cell ID numbers are indicated. Data points: tuning curve for each contrast as indicated in legend, computed by maximum likelihood estimation (Section S1.4.2). Error bars omitted for visibility given multiple curves. Cells illustrated in Fig. 5E (left to right) are #89, #79, and #66. (Continued on next page.)

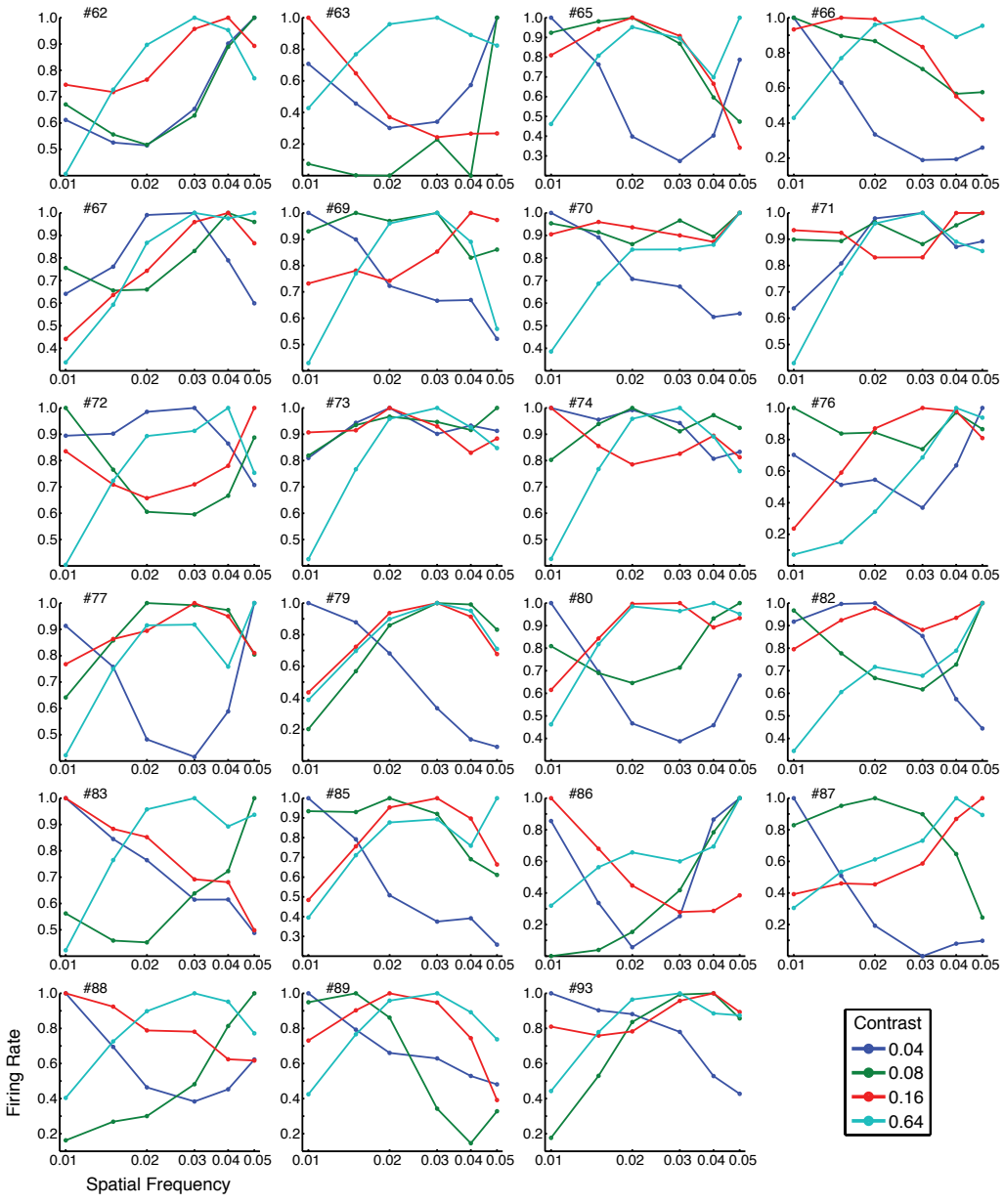

Figure S12:

All experimentally measured contrast-modulation tuning curves (related to Fig. 5); (continued).

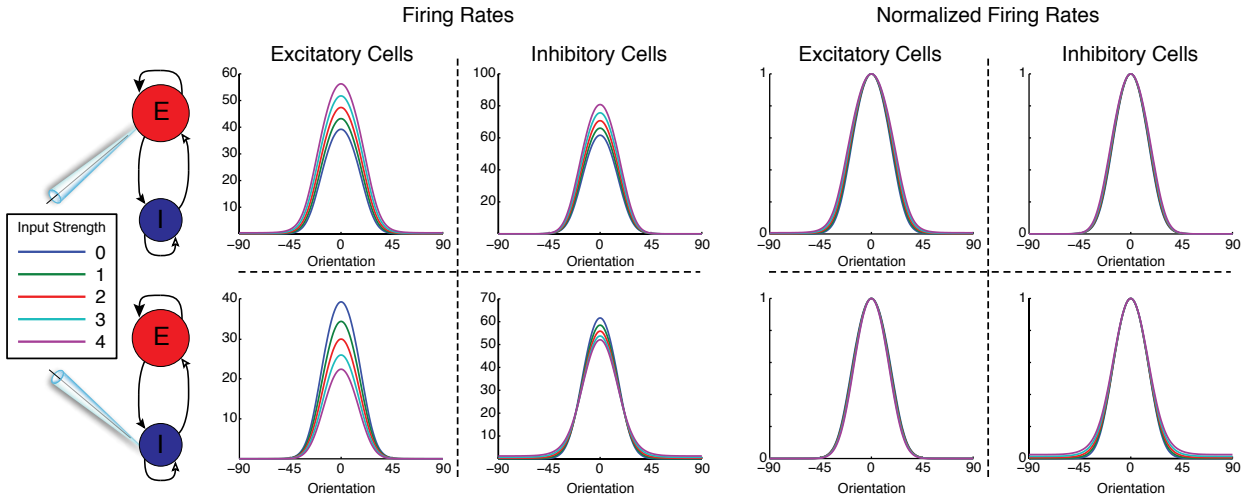

Figure S13:

In a nonlinear two-neuron model, shifting the balance of input towards E or I can cause a multiplicative change in the gain (related to Discussion). The rate model of balanced amplification studied in Murphy and Miller (2009) was a linear model, so responses to different stimuli necessarily added linearly. Thus, a modulatory input added a fixed amount to the responses to any other input. Here we show that balanced amplification in the present model with a power-law input/output nonlinearity can yield multiplicative gain modulation. "Tuning-curves" for both the E and I cell in this simple model were generated by varying the strength of a stimulus of equal magnitude delivered to both cells. At the same time, a constant modulatory input (relative input strength shown in key at left) was added to either the E cell (top row) or I cell (bottom row). Left two plots: adding an input to the E cell boosted the gain of both E and I, whereas adding an input to the I cell reduced the gain. Right two plots: curves replotted normalized so that maximal firing rate in each curve equals 1; the modulatory input induces a nearly multiplicative change in gain. Parameters: $n = 2.2$, $k = 0.01$, $W_{\mathrm{EE}} = 1.0$, $W_{\mathrm{IE}} = 1.25$, $W_{\mathrm{EI}} = 0.75$, $W_{\mathrm{II}} = 0.75$, $g_E = g_I = 1$. Baseline input at orientation θ: $50e^{-\frac{\theta^2}{2\sigma^2}}$, $\sigma = 20^{\mathrm{o}}$. Modulatory input: to I cells, from 0 to 10 in steps of 2.5; to E cells, from 0 to 5 in steps of 1.25. Although we did not tune parameters to get this effect, we have found in further parameter exploration that the degree to which effects are multiplicative vs. additive can vary with parameters.

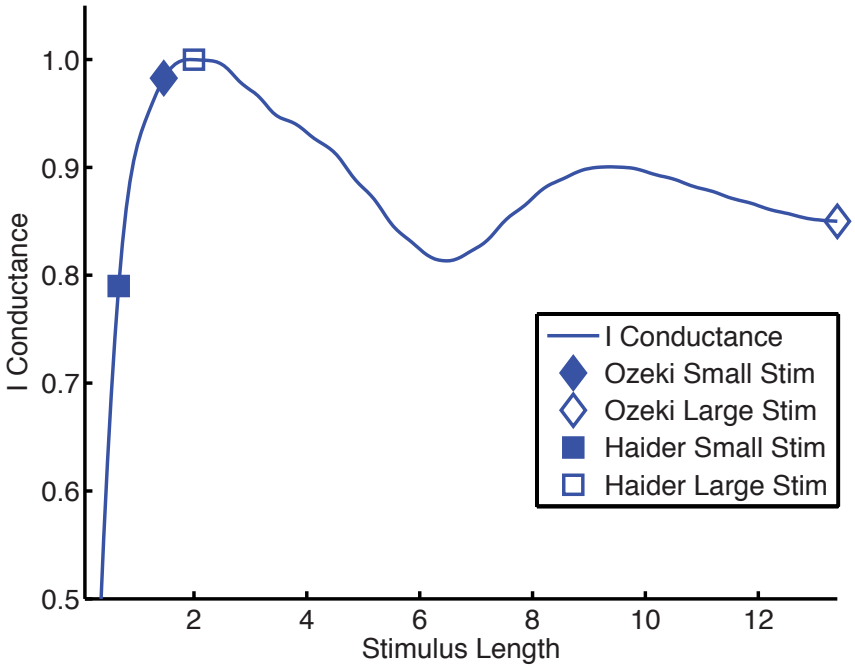

]

Figure S14:

How the model could simultaneously account for results of Ozeki et al. (2009) and Haider et al. (2010) (related to Discussion). We consider the model of Fig. 3. The figure shows the net I input received by an E cell ("I conductance") at the stimulus center as a function of stimulus length, for $c = 40$. Symbols mark possible sizes of small or center stimuli (filled symbols) and large or center+surround stimuli (open symbols) in experiment of Ozeki et al. (2009) (diamonds) or of Haider et al. (2010) (squares). This shows how Haider et al. (2010) could have seen an increase in inhibition received with increasing stimulus size, while Ozeki et al. (2009), using larger stimuli, saw a decrease in inhibition received. The indicated stimulus sizes are determined as follows. In Ozeki et al. (2009), the small stimulus size, meant to cover the CRF, was determined as the size of a shrinking annular stimulus, centered on the CRF center, that first evoked spikes, typically around 2° diameter; the large stimulus size was 20° diameter, typically about 10× larger. The annulus used to measure the CRF had a large outer diameter, and the inner diameter was shrunk until spikes were evoked. In our model for the parameters we use, an annulus with a large outer diameter never facilitates E-cell responses, and hence would not evoke spikes, down to an inner diameter of the E-cell summation-field size (Supplemental Fig. S8B), which is about 0.5° (Fig. 3C). Thus, if we used a CRF size as determined by a large annulus, it would be equal to the summation-field size. We instead here defined the CRF size to be the inner diameter of an annulus of 1° width – outer diameter 2° larger than inner diameter – that first evoked a response. This is quite simply a "hack", but we don't know how general across parameters is the model behavior that annuli with large outer diameter do not facilitate, and it at least illustrates how the model might produce behaviors like those seen experimentally. The key point is that the CRF should be larger than the E-cell summation field size, so that it more closely corresponds to the I-cell summation field size (which in the model for the parameters we use is larger than the E-cell summation field size, Figs. 3C, 7C) and thus to the peak of inhibition received. (Continued on next page.)

Figure S14:
(Continued). Indeed, in monkeys it has been reported that receptive fields determined by the annular procedure are on average 47% larger than the summation field size (Cavanaugh et al. 2002). While 47% is much less than the nearly 4-fold difference between summation field size and annular receptive field size used here, it may also be that for other parameters the average I-cell summation field size would be closer to 50% larger than the E-cell summation field size. We took the large stimulus for Ozeki et al. (2009) simply to be a large stimulus where suppression, though oscillating, had reached a plateau in overall level, here 13°. In Haider et al. (2010), the small stimulus was defined as the circular fit to the half-maximal iso-response contour of the RF as mapped by sparse noise stimuli, while the large stimulus was three times larger. In the model, the size of the small stimulus, so defined, is somewhat dependent on the size of the stimuli used for sparse mapping of the receptive field. We used a 0.5°-width stimulus, moved over 500 positions in steps of 0.0667°. A wider or narrower mapping stimulus would produce slightly larger or smaller sizes, respectively, for the small stimulus. We took the large stimulus for Haider et al. (2010) to be 3× the size of the small stimulus.

S4 Supplemental Tables: Legends

Supplemental Tables are provided in separate Excel files. Here we provide the legends for those tables.

Table S1:

Statistics for length-tuning analyses of Fig. 4B-C. Columns show: cell ID number (as in Supplemental Figs. S10-S12); SSE_DOG and SSE_SSM, the sum-squared error (SSE) for DOG model and for SSM model respectively; the value of the statistic F, and the corresponding p-value, for the nested F-test; and CV Percent Change, the % change in median sum-squared error from DOG to SSM models. For F-test, degrees of freedom (DF) are $(\Delta p, B)$ where Δp is the difference in the number of parameters in the two models, and $B = n - (1 + p)$ where n is the number of data points in the tuning curves being compared and p is the number of parameters in the more complex model. For Fig. 4B these numbers are: $n = 30$, $p = 10$, $\Delta p = 2$, $DF = (2, 19)$.

Table S2:

Statistics for length-tuning analyses of Supplemental Fig. S1F-G. Same as Supplemental Table S1, but for comparison of fits of SSM model to fits of 7-parameter DOG model ($a_7 = 0$) rather than 8-parameter DOG model as in Supplemental Table S1. All conventions as in Supplemental Table S1. For F-tests of Supplemental Fig. S1F: $n = 30$, $p = 10$, $\Delta p = 3$, $DF = (3, 19)$.

Table S3:

Statistics for position-tuning analyses of Fig. 4E-F. Same as Supplemental Table S1, but for position-tuning analyses of Fig. 4E-F. All conventions as in Supplemental Table S1. For F-tests for Fig. 4E: $n = 21$, $p = 10$, $\Delta p = 3$, $DF = (3, 10)$.

Table S4:

Statistics for length-tuning analyses of model units, Fig. 6C, left. Same as Supplemental Table S1, but for comparison of fits to length-tuning curves of SSM vs. DOG model for 100 randomly selected model E units, Fig. 6C. All conventions as in Supplemental Table S1, except that to save space we did not discuss cross-validation tests for model cells, so those statistics are not included here. For F-tests for Fig. 6C, left: $n = 61$, $p = 10$, $\Delta p = 2$, $DF = (2, 50)$.

Table S5:

Statistics for position-tuning analyses of model units, Fig. 6C, right. Same as Supplemental Table S1, but for comparison of fits to position-tuning curves of SSM vs. DOG model for 100 randomly selected model E units, Fig. 6C, right. All conventions as in Supplemental Table S1, except that to save space we did not discuss cross-validation tests for model units, so those statistics are not included here. For F-tests for Fig. 6C, right: $n = 30$, $p = 10$, $\Delta p = 3$, $DF = (3, 19)$.

References

Adesnik, H., Bruns, W., Taniguchi, H., Huang, Z. J., and Scanziani, M. (2012). A neural circuit for spatial summation in visual cortex. *Nature*, 490:226–231.

Ahmadian, Y., Rubin, D. B., and Miller, K. D. (2013). Analysis of the stabilized supralinear network. *Neural Computation*, 25:1994–2037.

Albus, K. (1975). A quantitative study of the projection area of the central and the paracentral visual field in area 17 of the cat. I. The precision of the topography. *Exp. Brain Res.*, 24:159–179.

Busse, L., Wade, A. R., and Carandini, M. (2009). Representation of concurrent stimuli by population activity in visual cortex. *Neuron*, 64:931–942.

Cavanaugh, J. R., Bair, W., and Movshon, J. A. (2002). Nature and interaction of signals from the receptive field center and surround in macaque V1 neurons. *J. Neurophysiol.*, 88:2530–2546.

Edgell, S. E. and Noon, S. M. (1984). Effect of violation of normality on the t test of the correlation coefficient. *Psych. Bull.*, 95:576–583.

Fino, E. and Yuste, R. (2011). Dense inhibitory connectivity in neocortex. *Neuron*, 69:1188–1203.

Haider, B., Krause, M. R., Duque, A., Yu, Y., Touryan, J., Mazer, J. A., and McCormick, D. A. (2010). Synaptic and network mechanisms of sparse and reliable visual cortical activity during nonclassical receptive field stimulation. *Neuron*, 65:107–121.

Hansel, D. and van Vreeswijk, C. (2002). How noise contributes to contrast invariance of orientation tuning in cat visual cortex. *J. Neurosci.*, 22:5118–5128.

Jones, J. P. and Palmer, L. A. (1987). An evaluation of the two-dimensional Gabor filter model of simple receptive fields in cat striate cortex. *J. Neurophysiol.*, 58:1233–1258.

Kaschube, M., Schnabel, M., Löwel, S., Coppola, D. M., White, L. E., and Wolf, F. (2010). Universality in the evolution of orientation columns in the visual cortex. *Science*, 330:1113–1116.

Kleiner, M., Brainard, D., and Pelli, D. (2007). What's new in psychtoolbox-3? *Perception*, 36:ECVP Abstract Supplement.

Miller, K. D. and Troyer, T. W. (2002). Neural noise can explain expansive, power-law nonlinearities in neural response functions. *J. Neurophysiol.*, 87:653–659.

Murphy, B. K. and Miller, K. D. (2009). Balanced amplification: A new mechanism of selective amplification of neural activity patterns. *Neuron*, 61:635–648.

Ozeki, H., Finn, I. M., Schaffer, E. S., Miller, K. D., and Ferster, D. (2009). Inhibitory stabilization of the cortical network underlies visual surround suppression. *Neuron*, 62:578–592.

Packer, A. M. and Yuste, R. (2011). Dense, unspecific connectivity of neocortical parvalbumin-positive interneurons: a canonical microcircuit for inhibition? *J. Neurosci.*, 31:13260–13271.

Sadagopan, S. and Ferster, D. (2012). Feedforward origins of response variability underlying contrast invariant orientation tuning in cat visual cortex. *Neuron*, 74:911–923.

Shao, Y. R., Isett, B. R., Miyashita, T., Chung, J., Pourzia, O., Gasperini, R. J., and Feldman, D. E. (2013). Plasticity of recurrent l2/3 inhibition and gamma oscillations by whisker experience. *Neuron*, 80:210–222.

Tsodyks, M. V., Skaggs, W. E., and Sejnowski, T. J.and McNaughton, B. L. (1997). Paradoxical effects of external modulation of inhibitory interneurons. *J. Neurosci.*, 17:4382–4388.

Turrigiano, G. (2011). Too many cooks? Intrinsic and synaptic homeostatic mechanisms in cortical circuit refinement. *Annu. Rev. Neurosci.*, 34:89–103.

Vogels, T. P., Sprekeler, H., Zenke, F., Clopath, C., and Gerstner, W. (2011). Inhibitory plasticity balances excitation and inhibition in sensory pathways and memory networks. *Science*, 334:1569–1573.

Wang, C., Bardy, C., Huang, J. Y., FitzGibbon, T., and Dreher, B. (2009). Contrast dependence of center and surround integration in primary visual cortex of the cat. *J Vis.*, 9:1–15.